

# The *R*-Process Alliance: A Nearly Complete *R*-Process Abundance Template Derived from Ultraviolet Spectroscopy of the *R*-Process-Enhanced Metal-Poor Star HD 222925\*

IAN U. ROEDERER,<sup>1,2</sup> JAMES E. LAWLER,<sup>3</sup> ELIZABETH A. DEN HARTOG,<sup>3</sup> VINICIUS M. PLACCO,<sup>4</sup> REBECCA SURMAN,<sup>5,2</sup>  
TIMOTHY C. BEERS,<sup>5,2</sup> RANA EZZEDDINE,<sup>6,2</sup> ANNA FREBEL,<sup>7,2</sup> TERESE T. HANSEN,<sup>8</sup> KOHEI HATTORI,<sup>9,10</sup>  
ERIKA M. HOLMBECK,<sup>11,2</sup> AND CHARLI M. SAKARI<sup>12</sup>

<sup>1</sup>*Department of Astronomy, University of Michigan, 1085 S. University Ave., Ann Arbor, MI 48109, USA*

<sup>2</sup>*Joint Institute for Nuclear Astrophysics – Center for the Evolution of the Elements (JINA-CEE), USA*

<sup>3</sup>*Department of Physics, University of Wisconsin-Madison, Madison, WI 53706, USA*

<sup>4</sup>*NSF's NOIRLab, Tucson, AZ 85719, USA*

<sup>5</sup>*Department of Physics, University of Notre Dame, Notre Dame, IN 46556, USA*

<sup>6</sup>*Department of Astronomy, University of Florida, Bryant Space Science Center, Gainesville, FL 32611, USA*

<sup>7</sup>*Department of Physics and Kavli Institute for Astrophysics and Space Research, Massachusetts Institute of Technology, Cambridge, MA 02139, USA*

<sup>8</sup>*Department of Astronomy, Stockholm University, Stockholm, Sweden*

<sup>9</sup>*National Astronomical Observatory of Japan, Mitaka, Tokyo 181-0015, Japan*

<sup>10</sup>*Institute of Statistical Mathematics, Tachikawa, Tokyo 190-0014, Japan*

<sup>11</sup>*Carnegie Observatories, Pasadena, CA 91101, USA*

<sup>12</sup>*Department of Physics and Astronomy, San Francisco State University, San Francisco, CA 94132, USA*

(Accepted for publication in the Astrophysical Journal Supplement Series)

## ABSTRACT

We present a nearly complete rapid neutron-capture process (*r*-process) chemical inventory of the metal-poor ( $[\text{Fe}/\text{H}] = -1.46 \pm 0.10$ ) *r*-process-enhanced ( $[\text{Eu}/\text{Fe}] = +1.32 \pm 0.08$ ) halo star HD 222925. This abundance set is the most complete for any object beyond the solar system, with a total of 63 metals detected and seven with upper limits. It comprises 42 elements from  $31 \leq Z \leq 90$ , including elements rarely detected in *r*-process-enhanced stars, such as Ga, Ge, As, Se, Cd, In, Sn, Sb, Te, W, Re, Os, Ir, Pt, and Au. We derive these abundances from an analysis of 404 absorption lines in ultraviolet spectra collected using the Space Telescope Imaging Spectrograph on the Hubble Space Telescope and previously analyzed optical spectra. A series of appendices discusses the atomic data and quality of fits for these lines. The *r*-process elements from Ba to Pb, including all elements at the third *r*-process peak, exhibit remarkable agreement with the Solar *r*-process residuals, with a standard deviation of the differences of only 0.08 dex (17%). In contrast, deviations among the lighter elements from Ga to Te span nearly 1.4 dex, and they show distinct trends from Ga to Se, Nb through Cd, and In through Te. The *r*-process contribution to Ga, Ge, and As is small, and Se is the lightest element whose production is dominated by the *r*-process. The lanthanide fraction,  $\log X_{\text{La}} = -1.39 \pm 0.09$ , is typical for *r*-process-enhanced stars and higher than that of the kilonova from the GW170817 neutron-star merger event. We advocate adopting this pattern as an alternative to the Solar *r*-process-element residuals when confronting future theoretical models of heavy-element nucleosynthesis with observations.

**Keywords:** Nucleosynthesis (1131); *R*-process (1324); Stellar abundances (1577); Ultraviolet astronomy (1736); Spectral line identification (2073)

## 1. INTRODUCTION

The rapid neutron-capture process, or *r*-process, is one of the main ways that stars and their remnants produce the heaviest elements (atomic number,  $Z$ ,  $> 30$ ). Recent theoretical and observational advances generally agree that rare, prolific events are responsible for much

Email: iur@umich.edu

\* Based on observations made with the NASA/ESA Hubble Space Telescope, obtained at the Space Telescope Science Institute (STScI), which is operated by the Association of Universities for Research in Astronomy, Inc. (AURA) under NASA contract NAS 5-26555. These observations are primarily associated with program GO-15657. Data from programs GO-7348, GO-8197, GO-9804, GO-12554, GO-14161, and GO-14765 are also used. This paper also includes data gathered with the 6.5 meter Magellan Telescopes located at Las Campanas Observatory, Chile.

of the  $r$ -process material found in the Sun and other stars in and around the Milky Way (e.g., [Hotokezaka et al. 2015](#); [Ji et al. 2016](#); [Abbott et al. 2017](#); [Siegel et al. 2019](#)). There are many open questions about the  $r$ -process, including one that has persisted for decades: *which elements were produced by the  $r$ -process, and in what amounts?*

The neutron-star merger GW170817 remains the only  $r$ -process nucleosynthesis event to have been observed in the act, but the detailed abundance pattern of that event remains unknown. The kilonova that followed the merger was linked to  $r$ -process nucleosynthesis by comparing the evolving photometric colors with theoretical predictions for radiative transfer rates in representative  $r$ -process ions with high opacities (e.g., [Kasen et al. 2017](#)). Only the  $r$ -process element strontium (Sr,  $Z = 38$ ) has possibly been identified in the ejecta of that merger event ([Watson et al. 2019](#)). The spectral lines of all other  $r$ -process elements—including silver, platinum, and gold—are blurred by the high expansion velocity of the ejecta ( $\approx 0.1$ – $0.2c$ ; e.g., [Chornock et al. 2017](#); [Smartt et al. 2017](#)) and thus cannot be unambiguously identified and translated into abundances.

Instead, the standard approach to identifying which elements were produced by the  $r$ -process and in what amounts derives from models calibrated to Solar isotopic abundances measured from Type-I carbonaceous chondrite meteorites. A model based on stellar evolution and Galactic chemical evolution (e.g., [Arlandini et al. 1999](#)), or an analytic model (e.g., [Cameron 1982](#); [Käppeler et al. 1989](#)), is fit to abundances of isotopes that can only be produced by the slow neutron-capture process ( $s$ -process). The  $s$ -process contribution to all other isotopes is inferred, and all residual abundances are ascribed to the  $r$ -process. This set of “ $r$ -process residuals” is frequently used as the observational ground truth that  $r$ -process models aim to reproduce (e.g., [Wanajo et al. 2001](#); [Kratz et al. 2007](#); [Wu et al. 2016](#)). This approach has been justified by the unexpected observation of a near-perfect match between the Solar  $r$ -process residuals and the heavy-element abundances found in a rare few percent of old, metal-poor stars in the Milky Way (e.g., [Cowan et al. 1995](#); [Snedden et al. 1996](#); [Hill et al. 2002](#); [Roederer et al. 2009](#); [Frebel 2018](#); [Cowan et al. 2021](#)). This similarity gave rise to the so-called “universality” of the  $r$ -process, at least for the heaviest stable and observable  $r$ -process elements ( $56 \leq Z \leq 82$ ).

This single template for the  $r$ -process pattern has guided the vast majority of theoretical explorations of  $r$ -process nucleosynthesis. It relies on the critical assumption that  $r$ -process and  $s$ -process nucleosynthesis are sufficient to explain the origin of all heavy elements in the solar system. Multiple events, processes, and patterns are hidden within the  $r$ -process residuals (e.g., [Goriely 1999](#); [Travaglio et al. 2004](#); [Bisterzo et al. 2017](#); [Côté et al. 2018](#)). Thus, an independent assessment of a

detailed inventory of the elements produced in a single  $r$ -process event is highly desirable.

Ongoing efforts by the  $R$ -Process Alliance (RPA) have identified an ideal metal-poor halo star for this task, HD 222925. Our previous analysis ([Roederer et al. 2018b](#)) of the optical spectrum of HD 222925 confirmed that it is a moderately metal-poor ( $[\text{Fe}/\text{H}] = -1.47$ ) field red horizontal-branch star with a high level of  $r$ -process enhancement ( $[\text{Eu}/\text{Fe}] = +1.33$ ). One event likely dominated the production of  $r$ -process elements found in HD 222925. This assertion, commonly applied to other highly  $r$ -process-enhanced metal-poor stars, was recently rooted on firmer observational ground by a number of such stars, including HD 222925, being placed into groups, based on their orbital kinematics and small metallicity dispersions ([Roederer et al. 2018a](#); [Gudin et al. 2021](#)). The stars in each group are presumed to have formed together, within a low-mass dwarf galaxy or star cluster that was enriched by one prolific  $r$ -process event. Subsequent tidal interactions with the much more massive Milky Way disrupted these systems and deposited their stars into the stellar halo, where they are found today.

We present high-quality ultraviolet (UV) spectroscopy of HD 222925 conducted with the Space Telescope Imaging Spectrograph (STIS) on board the Hubble Space Telescope (HST). Several  $r$ -process-enhanced stars have been previously observed by HST (e.g., [Snedden et al. 1998](#); [Cowan et al. 2005](#); [Barbuy et al. 2011](#); [Roederer et al. 2012a](#)), but none of them share the unique combination of characteristics found in HD 222925: (1) bright enough in the UV ( $V = 9.02$ , [Norris et al. 1985](#);  $\text{GALEX } NUV = 13.41$ , [Martin et al. 2005](#)) for high-resolution spectroscopy with decent signal-to-noise ratios (S/N) at wavelengths as short as 2000 Å; (2) sufficiently metal poor that the UV spectrum is not overwhelmed by strong lines of Fe-group elements; (3) sufficiently  $r$ -process enhanced that lines of rarely detected  $r$ -process elements may be present; and (4) dominated by  $r$ -process material produced in a single event. Our derived  $r$ -process abundance pattern of HD 222925 thus provides a viable alternative to the inferred elemental Solar  $r$ -process residuals.

Section 2 describes the new STIS observations. Section 3 describes our abundance analysis methods, and Section 4 presents our results. We discuss these results in Section 5 and summarize our findings in Section 6. Appendix A provides a detailed discussion of the UV absorption lines and the atomic data used to derive the abundances from them.

## 2. OBSERVATIONS

HD 222925 was observed with STIS ([Kimble et al. 1998](#); [Woodgate et al. 1998](#)) between 2019 October 03 and 2020 March 20. Several visits early in this series suffered from delayed guide-star (re)acquisitions, which was part of a higher than usual failure rate across many

observing programs. STScI staff recognized and corrected the issue by adopting a longer and more reliable guide-star acquisition strategy. Failed observations were repeated, and our program was successfully executed.

Observations were made using the E230H echelle grating, the  $0''.2 \times 0''.09$  slit, and the near-UV Multinode Microchannel Array detector. This setup produces spectra with a resolving power of  $R \equiv \lambda/\Delta\lambda = 114,000$ . Five central wavelength settings were used (i2063, i2313, i2563, i2812, and c3012), resulting in complete wavelength coverage from 1936 to 3145 Å. The observations were made during 47 orbits spread across 17 visits, not counting observations that were repeated because of guide-star acquisition failures. The integration times for the individual setups were 71,250 s (i2063, distributed across 27 individual observations), 23,291 s (i2313, 9 observations), 12,050 s (i2563, 5 observations), 10,106 s (i2812, 4 observations), and 3,948 s (c3012, 2 observations), for a total observing time on target of 120,645 s, or 33.5 hr.

The spectra were processed automatically by the CALSTIS software package and downloaded from the Mikulski Archive for Space Telescopes (MAST). We first shift all observations to a common rest velocity. We then coadd and normalize the spectrum using tools in the IRAF “onedspec” package, taking care to match the continuum level where the edges of adjacent orders and settings overlap. The S/N ratios per pixel in the final, coadded spectrum are approximately 10/1 at 2000 Å, 20/1 at 2100 Å, 30/1 at 2200 Å, and 30/1 to 40/1 between 2200 and 2900 Å, before decreasing to 20/1 at 3000 Å and 15/1 at 3100 Å. The region of the spectrum with  $\lambda < 2000$  Å has such a low S/N that we do not use it for our analysis.

We also revisit the optical spectrum of HD 222925 presented in Roederer et al. (2018b). That spectrum was collected using the Magellan Inamori Kyocera Echelle spectrograph (MIKE; Bernstein et al. 2003) mounted on the Landon Clay (Magellan II) Telescope at Las Campanas Observatory, Chile. It has  $R = 68,000$  in the blue ( $3330 \leq \lambda \leq 5000$  Å) and  $R = 61,000$  in the red ( $5000 \leq \lambda \leq 9410$  Å) with S/N ratios of several hundred per pixel.

### 3. ANALYSIS METHODS

#### 3.1. Definitions

We adopt the standard nomenclature for elemental abundances and ratios. The abundance of an element X is defined as the number of X atoms per  $10^{12}$  H atoms,  $\log \varepsilon(X) \equiv \log_{10}(N_X/N_H) + 12.0$ . The abundance ratio of the elements X and Y relative to the Solar ratio is

defined as  $[X/Y] \equiv \log_{10}(N_X/N_Y) - \log_{10}(N_X/N_Y)_\odot$ . We adopt the Solar photospheric abundances of Asplund et al. (2009). By convention, abundances or ratios denoted with the ionization state are understood to be the total elemental abundance, as derived from transitions of that particular ionization state after Saha (1921) ionization corrections have been applied.

#### 3.2. Stellar Parameters

We adopt the same stellar parameters and model atmosphere derived by Roederer et al. (2018b): effective temperature ( $T_{\text{eff}} = 5636 \pm 103$  K, log of the surface gravity ( $\log g = 2.54 \pm 0.17$  [cgs units], microturbulent velocity parameter ( $v_t = 2.20 \pm 0.20$  km s $^{-1}$ , and model metallicity ( $[M/H] = -1.5 \pm 0.1$ ).  $T_{\text{eff}}$  was calculated by averaging the  $T_{\text{eff}}$  values predicted by five different optical and near-infrared colors. The log  $g$  was calculated from fundamental relations, and it included the parallax measurement from the Gaia mission’s second data release (DR2; Lindegren et al. 2018). The parallax measurement from Gaia’s early third data release (EDR3; Gaia Collaboration et al. 2021) is effectively identical to the DR2 value, and log  $g$  would change by  $< 0.01$  dex using the EDR3 value instead of the DR2 value. The  $v_t$  parameter was derived by requiring no dependence between the line strength and the abundance derived from Fe I lines. Finally, the  $[M/H]$  value approximately matched the Fe abundance.

#### 3.3. Spectrum Synthesis

We derive all abundances by using the MOOG (Snedden 1973; Sobeck et al. 2011) “synthesis” driver to compare synthetic spectra to the observed spectrum. MOOG assumes that local thermodynamic equilibrium (LTE) holds in the line-forming layers of the atmosphere. Line lists for these syntheses are generated using a version of the LINEMAKE code (Placco et al. 2021) that includes updates to the atomic data for UV transitions. LINEMAKE starts with the Kurucz (2011) line compendia and supplements or replaces individual lines with atomic data—transition probabilities, hyperfine splitting, etc.—recommended by the Wisconsin Atomic Transition Probability group, the National Institute of Standards and Technology (NIST) Atomic Spectra Database (ASD), refinements to Fe I line lists by Peterson & Kurucz (2015) and Peterson et al. (2017), or our own assessments of literature data. The fitting uncertainties reported in Table 1 are usually dominated by continuum placement or blending features, so these are larger than would be expected based on the well-resolved line profiles.

**Table 1.** Line Atomic Data, References, and Derived Abundances

Species	$\lambda$	$E_{\text{low}}$	$\log(gf)$	Reference	$\log \varepsilon(X)$	Uncertainty
	(Å)	(eV)				(dex)
Be II	3130.422	0.00	-0.18	1	$< -0.90$	...
Be II	3131.067	0.00	-0.48	1	$< -0.80$	...
B I	2088.889	0.00	-1.02	1	$< 1.10$	...
B I	2089.570	0.00	-0.72	1	$< 0.90$	...
B I	2496.796	0.00	-0.80	1	$< 0.40$	...
C I	2964.846	0.00	-7.20	1	6.70	0.34
Al I	2118.332	0.00	-1.56	1	4.32	0.19
Al I	2129.678	0.00	-1.38	1	4.28	0.23
Al I	2199.180	0.00	-2.60	2	4.27	0.19

**Table 1** *continued*

**Table 1** (*continued*)

Species	$\lambda$	$E_{\text{low}}$	$\log(gf)$	Reference	$\log \varepsilon(X)$	Uncertainty
	(Å)	(eV)				(dex)

**References**—1 = NIST (Kramida et al. 2020); 2 = NIST (Kramida et al. 2020) for  $\log(gf)$  value and VALD (Piskunov et al. 1995; Pakhomov et al. 2019) for HFS; 3 = Träbert et al. (1999) for  $\log(gf)$  value and Roederer & Lawler (2021) for HFS; 4 = Biemont et al. (1993); 5 = Theodosiou (1989); 6 = Lawler et al. (2013); 7 = Wood et al. (2013); 8 = Wood et al. (2014a) for  $\log(gf)$  value and HFS; 9 = Sobeck et al. (2007); 10 = Gurell et al. (2010); 11 = Lawler et al. (2017); 12 = Den Hartog et al. (2011) for  $\log(gf)$  value and HFS; 13 = Belmonte et al. (2017); 14 = Den Hartog et al. (2019); 15 = Lawler et al. (2015) for  $\log(gf)$  value and Kurucz (2011) for HFS; 16 = Lawler et al. (2018) for  $\log(gf)$  value and this study for HFS; 17 = Wood et al. (2014b); 18 = Fedchak & Lawler (1999); 19 = NIST (Kramida et al. 2020) for  $\log(gf)$  value and Kurucz (2011) for HFS; 20 = Roederer & Lawler (2012) for  $\log(gf)$  value; 21 = This study; 22 = Li et al. (1999); 23 = Holmgren (1975); 24 = Morton (2000); 25 = Biémont et al. (2011); 26 = Ljung et al. (2006); 27 = Nilsson et al. (2010); 28 = Nilsson & Ivarsson (2008); 29 = Sikström et al. (2001); 30 = Johansson et al. (1994); 31 = Xu et al. (2004); 32 = Curtis et al. (2000); 33 = Oliver & Hibbert (2010); 34 = Hartman et al. (2010); 35 = Roederer et al. (2012b); 36 = Den Hartog et al. (2006); 37 = Lawler et al. (2001); 38 = Wickliffe et al. (2000); 39 = Lawler et al. (2008); 40 = Wickliffe & Lawler (1997); 41 = Biémont et al. (1998) for  $\log(gf)$  value and Roederer & Lawler (2012) for HFS/IS; 42 = Roederer et al. (2010) for  $\log(gf)$  value and Den Hartog et al. (2020) for HFS; 43 = Quinet et al. (1999) for  $\log(gf)$  value and Den Hartog et al. (2020) for HFS; 44 = Lawler et al. (2009) for  $\log(gf)$  value and Den Hartog et al. (2020) for HFS; 45 = Den Hartog et al. (2021a); 46 = Lawler et al. (2007); 47 = Quinet et al. (2009); 48 = Nilsson et al. (2008); 49 = Kling et al. (2000); 50 = Roederer et al., in preparation; 51 = Palmeri et al. (2005); 52 = Quinet et al. (2006); 53 = Kramida et al. (2020) for  $\log(gf)$  value and this study for HFS/IS; 54 = Ivarsson et al. (2004); 55 = Den Hartog et al. (2005) for  $\log(gf)$  value only; 56 = Den Hartog et al. (2005) for  $\log(gf)$  value and this study for HFS/IS; 57 = Den Hartog et al. (2005) for  $\log(gf)$  value and HFS/IS; 58 = Quinet et al. (2008); 59 = Zhang et al. (2018); 60 = Hannaford et al. (1981) for  $\log(gf)$  value and Demidov et al. (2021) for HFS; 61 = Quinet et al. (2007) for  $\log(gf)$  value and Roederer et al. (2020) for HFS/IS;

NOTE—The two Al I transitions at 2204.619 (E.P. = 0.01 eV,  $\log(gf) = -2.29$ , NIST grade C) and 2204.660 Å form a single line in our spectrum. The two Cu I transitions at 2024.323 and 2024.337 Å form a single line in our spectrum; HFS patterns are known for both lines, and the NIST ASD lists B grades for both  $\log(gf)$  values. A complete machine-readable version of Table 1 is available online. A short version is shown here to illustrate its form and content.

There are several strong absorption lines that severely depress the continuum for a few Å on either side of each line. Low-lying levels of Fe I and Fe II are mostly responsible for this effect, but similar behavior is observed among Mg I and Mg II, Si I, Cr II, and Mn II lines. Most of these lines are found between 2320 and 2640 Å, although a few lines are found at shorter wavelengths. The  $^2S-^2P^o$  Mg II resonance doublet depresses the continuum by a few percent or more for about 35 Å on either side of 2800 Å. The  $\log(gf)$  values and damp-

ing constants are known for these transitions, as are the abundances of these elements. Analysis of other lines in these regions proceeds with caution, and only after rescaling the observed spectrum locally to match the predicted wings of the strong lines.

#### 3.4. Iron (Fe, $Z = 26$ ) and the UV Continuum

We verify that MOOG is modeling the UV continuum reliably by comparing the abundances derived from optical and UV lines of Fe. We synthesize 50 Å regions of the spectrum, match our syntheses to the observed



spectrum, and search for reasonably unblended Fe lines. Strong lines whose damping wings depress the continuum are not considered for this analysis.

We derive abundances from Fe I lines when the line is reasonably unblended and has a  $\log(gf)$  value listed in [Belmonte et al. \(2017\)](#) or the NIST ASD with a grade of C or better (uncertainty < 25%, or 0.12 dex). We derive abundances from Fe II lines when the line is similarly unblended and has a  $\log(gf)$  value listed in [Den Hartog et al. \(2019\)](#) or the NIST ASD with a grade of C or better. A total of 70 Fe I and 42 Fe II lines meet these criteria; they are listed in Table 1. The uncertainties listed in Table 1 are statistical and reflect the goodness of the line fit and the  $\log(gf)$  uncertainty. The weighted mean abundance derived from these UV Fe I lines is  $[\text{Fe}/\text{H}] = -1.61 \pm 0.02$  ( $\sigma = 0.18$  dex), which matches the value derived by [Roederer et al. \(2018b\)](#) from 124 optical lines,  $-1.58 \pm 0.01$  ( $\sigma = 0.08$  dex). Likewise, the weighted mean abundance derived from these UV Fe II lines is  $[\text{Fe}/\text{H}] = -1.46 \pm 0.03$  ( $\sigma = 0.11$  dex), which also matches the value derived by [Roederer et al.](#) from 10 optical lines,  $-1.41 \pm 0.03$  ( $\sigma = 0.08$  dex).<sup>1</sup>

We draw three important conclusions from this test. First, the optical and UV abundance scales are in excellent agreement, which suggests that the continuum is being consistently modeled within MOOG. Secondly, our data reduction and continuum normalization procedures have yielded a UV spectrum that is approximately “correct,” except possibly in regions near strong lines, as noted in Section 3.3. Finally, the difference between the Fe abundance derived from Fe I and Fe II lines is small but significant, about  $+0.15 \pm 0.04$  dex. A small non-LTE (NLTE) overionization correction is applied to the abundance derived from Fe I lines. [Roederer et al. \(2018b\)](#) used the INSPECT database ([Bergemann et al. 2012; Lind et al. 2012](#)) to estimate a correction of +0.12 dex, which agrees well.

### 3.5. Other $Z \leq 30$ Elements

We verify that other elements yield consistent abundance results when derived from optical and UV lines. We also detect lines of some species that are not detected in the optical spectrum of HD 222925. Each species is discussed in detail in Appendix A. The abundances derived from each line are presented in Table 1, along with the wavelength ( $\lambda$ ), energy of the lower level of the transition ( $E_{\text{low}}$ ),  $\log(gf)$  value, and reference for the  $\log(gf)$  value and any hyperfine splitting (HFS) or isotope shifts (IS) included in the synthesis. The weighted mean abun-

dances derived from UV lines are presented in Table 2. The final set of recommended elemental abundances in HD 222925 is presented in Table 3.

**Table 2.** Mean Abundances in HD 222925 Derived from the STIS/E230H UV Spectrum

Species	$\log \varepsilon_{\odot}(\text{X})^a$	$\log \varepsilon(\text{X})$	$[\text{X}/\text{Fe}]^b$	Unc. (dex)	$N_{\text{lines}}$
Be II	1.38	< -0.90	< -0.82	...	2
B I	2.70	< 0.40	< -0.84	...	3
C I	8.43	6.70	-0.27	0.30	1
Al I	6.45	4.23	-0.76	0.07	8
Al II	6.45	4.77	-0.22	0.13	1
Si I	7.51	6.02	-0.03	0.14	5
Si II <sup>c</sup>	7.51	6.48	+0.43	0.18	4
P I	5.41	4.13	+0.18	0.15	3
S I <sup>c</sup>	7.12	5.98	+0.32	0.19	3
Ca II	6.34	5.24	+0.36	0.16	2
Ti I	4.95	3.65	+0.16	0.10	5
Ti II	4.95	3.77	+0.28	0.06	21
V II	3.93	2.72	+0.25	0.14	9
Cr I	5.64	3.88	-0.30	0.07	15
Cr II	5.64	4.16	-0.02	0.06	20
Mn II	5.43	3.84	-0.13	0.12	2
Fe I	7.50	5.89	-1.61	0.18	70
Fe II	7.50	6.04	-1.46	0.11	42
Co I	4.99	3.39	-0.14	0.08	11
Co II	4.99	3.48	-0.05	0.13	7
Ni I	6.22	4.59	-0.17	0.07	17
Ni II	6.22	4.74	-0.02	0.10	6
Cu I	4.19	1.93	-0.80	0.12	3
Cu II	4.19	2.09	-0.64	0.10	6
Zn I	4.56	3.15	+0.05	0.11	2
Ga II	3.04	1.26	-0.32	0.27	1
Ge I	3.65	1.46	-0.73	0.11	5
As I	2.30	1.01	+0.17	0.23	1
Se I	3.34	2.62	+0.74	0.22	1
Y II	2.21	1.06	+0.31	0.12	4
Zr II	2.58	1.76	+0.64	0.07	22
Nb II	1.46	0.73	+0.73	0.11	9

**Table 2** continued

<sup>1</sup> [Roederer et al. \(2018b\)](#) used the NIST ASD  $\log(gf)$  scale for Fe II lines. Subsequent laboratory analysis by [Den Hartog et al. \(2019\)](#) showed better agreement with the [Meléndez & Barbuy \(2009\)](#) scale. The value reported in the text here,  $[\text{Fe}/\text{H}] = -1.41$ , has been corrected by +0.06 dex to the  $\log(gf)$  scale of [Meléndez & Barbuy](#) and [Den Hartog et al.](#), which is the scale adopted for the UV Fe II lines.

**Table 2** (*continued*)

Species	$\log \varepsilon_{\odot}(\text{X})^a$	$\log \varepsilon(\text{X})$	$[\text{X}/\text{Fe}]^b$	Unc.	$N_{\text{lines}}$
				(dex)	
Mo II	1.88	1.36	+0.94	0.09	12
Ru II	1.75	1.26	+0.97	0.19	2
Cd I	1.71	0.34	+0.09	0.17	1
In II	0.80	0.51	+1.17	0.21	1
Sn II	2.04	1.39	+0.81	0.20	1
Sb I	1.01	0.37	+0.82	0.17	1
Te I	2.18	1.63	+0.91	0.14	2
Gd II	1.07	0.80	+1.19	0.10	6
Tb II	0.30	0.31	+1.47	0.19	1
Dy II	1.10	1.01	+1.37	0.17	1
Er II	0.92	0.67	+1.21	0.12	3
Tm II	0.10	0.06	+1.42	0.13	3
Yb II	0.84	0.63	+1.25	0.19	1
Lu II	0.10	-0.10	+1.26	0.11	7
Hf II	0.85	0.31	+0.92	0.10	15
Ta II	-0.12	< -0.30	< +1.28	...	1
W II	0.85	0.02	+0.63	0.11	6
Re II	0.26	0.16	+1.36	0.15	2
Os I	1.40	1.19	+1.25	0.14	4
Os II	1.40	1.10	+1.16	0.12	5
Ir I	1.38	1.26	+1.34	0.12	4
Ir II	1.38	1.58	+1.66	0.23	2
Pt I	1.62	1.45	+1.29	0.10	8
Pt II	1.62	1.48	+1.32	0.26	1
Au I	0.92	0.53	+1.07	0.22	1
Pb II	2.04	1.14	+0.56	0.14	1
Bi I	0.65	<0.80	< +1.61	...	1

<sup>a</sup>Asplund et al. (2009)<sup>b</sup>[Fe/H] is given for Fe I and Fe II. For all other species, the [X/Fe] ratios are referenced to the Fe abundance derived from Fe II lines; i.e., [Fe/H] = -1.46.<sup>c</sup>Newly derived from the MIKE optical spectrum.**Table 3.** Recommended Metal Abundances in HD 222925

Z	El.	$\log \varepsilon(\text{X})$	[X/H]	Unc. <sup>a</sup>	[X/Fe]	Unc. <sup>b</sup>
				(dex)		(dex)
3	Li	<0.80	...	...	...	...
4	Be	< -0.90	-2.28	...	< -0.82	...
5	B	<0.40	-2.30	...	< -0.84	...
6	C	7.11	-1.32	0.15	+0.14	0.17
7	N	6.45	-1.38	0.20	+0.08	0.21
8	O	7.65	-1.04	0.13	+0.42	0.07
11	Na	4.49	-1.75	0.07	-0.29	0.07
12	Mg	6.43	-1.17	0.08	+0.29	0.05
13	Al	4.78	-1.67	0.13	-0.21	0.13
14	Si	6.47	-1.04	0.11	+0.42	0.11
15	P	4.13	-1.28	0.18	+0.18	0.15
16	S	5.98	-1.14	0.19	+0.32	0.19
19	K	3.68	-1.35	0.10	+0.11	0.04
20	Ca	5.14	-1.20	0.08	+0.26	0.05
21	Sc	1.82	-1.33	0.13	+0.13	0.08
22	Ti	3.82	-1.13	0.10	+0.33	0.05
23	V	2.67	-1.26	0.15	+0.20	0.08
24	Cr	4.16	-1.48	0.11	-0.02	0.05
25	Mn	3.80	-1.63	0.19	-0.17	0.16
26	Fe	6.04	-1.46	0.10	+0.00	0.10
27	Co	3.48	-1.51	0.20	-0.05	0.11
28	Ni	4.74	-1.48	0.12	-0.02	0.09
29	Cu	2.09	-2.10	0.10	-0.64	0.10
30	Zn	3.15	-1.41	0.11	+0.05	0.05
31	Ga	1.26	-1.78	0.27	-0.32	0.27
32	Ge	1.46	-2.19	0.13	-0.73	0.11
33	As	1.01	-1.29	0.23	+0.17	0.23
34	Se	2.62	-0.72	0.22	+0.74	0.22
37	Rb	<2.10	< -0.42	...	< +1.04	...
38	Sr	1.98	-0.89	0.13	+0.57	0.13
39	Y	1.04	-1.17	0.10	+0.29	0.07
40	Zr	1.74	-0.84	0.11	+0.62	0.08
41	Nb	0.71	-0.75	0.14	+0.71	0.11
42	Mo	1.36	-0.52	0.10	+0.94	0.07
44	Ru	1.32	-0.43	0.11	+1.03	0.11
45	Rh	0.64	-0.27	0.16	+1.19	0.12

**Table 3** *continued*

**Table 3** (*continued*)

$Z$	El.	$\log \varepsilon(X)$	[X/H]	Unc. <sup>a</sup>	[X/Fe]	Unc. <sup>b</sup>
				(dex)		(dex)
46	Pd	1.05	−0.52	0.15	+0.94	0.08
47	Ag	0.44	−0.50	0.18	+0.96	0.13
48	Cd	0.34	−1.37	0.25	+0.09	0.17
49	In	0.51	−0.29	0.21	+1.17	0.21
50	Sn	1.39	−0.65	0.20	+0.81	0.20
51	Sb	0.37	−0.64	0.17	+0.82	0.17
52	Te	1.63	−0.55	0.17	+0.91	0.14
56	Ba	1.26	−0.92	0.09	+0.54	0.06
57	La	0.51	−0.59	0.09	+0.87	0.07
58	Ce	0.85	−0.73	0.08	+0.73	0.07
59	Pr	0.22	−0.50	0.10	+0.96	0.08
60	Nd	0.88	−0.54	0.09	+0.92	0.08
62	Sm	0.62	−0.34	0.09	+1.12	0.08
63	Eu	0.38	−0.14	0.09	+1.32	0.08
64	Gd	0.82	−0.25	0.09	+1.21	0.08
65	Tb	0.18	−0.12	0.11	+1.34	0.09
66	Dy	1.01	−0.09	0.11	+1.37	0.08
67	Ho	0.12	−0.36	0.15	+1.10	0.12
68	Er	0.73	−0.19	0.10	+1.27	0.08
69	Tm	−0.09	−0.19	0.10	+1.27	0.08
70	Yb	0.55	−0.29	0.19	+1.17	0.19
71	Lu	−0.04	−0.14	0.10	+1.32	0.09
72	Hf	0.32	−0.53	0.12	+0.93	0.10
73	Ta	< −0.30	< −0.18	...	< +1.28	...
74	W	0.02	−0.83	0.11	+0.63	0.11
75	Re	0.16	−0.10	0.15	+1.36	0.15
76	Os	1.17	−0.23	0.14	+1.23	0.09
77	Ir	1.28	−0.10	0.17	+1.36	0.10
78	Pt	1.45	−0.17	0.14	+1.29	0.10
79	Au	0.53	−0.39	0.23	+1.07	0.22
82	Pb	1.14	−0.90	0.16	+0.56	0.14
83	Bi	<0.80	< +0.15	...	< +1.61	...
90	Th	−0.06	−0.08	0.12	+1.38	0.11
92	U	< −0.50	< +0.04	...	< +1.50	...

**Table 3** *continued***Table 3** (*continued*)

$Z$	El.	$\log \varepsilon(X)$	[X/H]	Unc. <sup>a</sup>	[X/Fe]	Unc. <sup>b</sup>
				(dex)		(dex)

NOTE—Readers interested in the details of why these recommendations are made are encouraged to consult the relevant sections in Appendix A. The C abundance is corrected for stellar evolution effects, as described in [Placco et al. \(2014\)](#). The O abundance is adopted from [Navarrete et al. \(2015\)](#). A complete machine-readable version of Table 3 is available online.

<sup>a</sup>Uncertainty on  $\log \varepsilon(X)$  and [X/H] abundances.

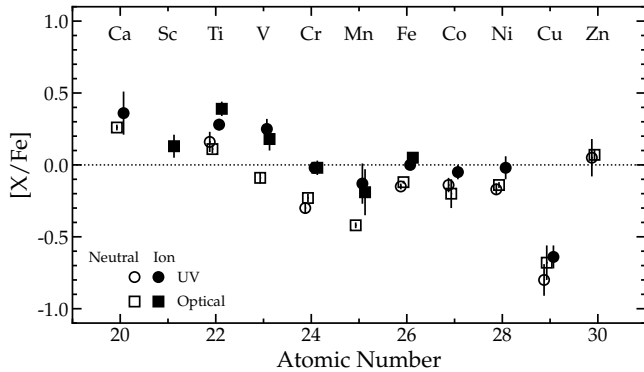
<sup>b</sup>Uncertainty on [X/Fe] abundance ratios. This value also approximates the uncertainty in the abundance ratios of other elements relative to each other; e.g., [Ba/Eu].

Figure 1 illustrates the abundance ratios for Ca and elements in the Fe group, and it shows that the abundances derived from the UV spectrum of HD 222925 are fully compatible with those derived from the optical spectrum. In most cases, the abundances derived from lines of the neutral species are lower by  $\approx 0.1$ – $0.3$  dex than the abundances derived from lines of the corresponding ions. NLTE abundance calculations for metal-poor stars suggest this difference is primarily due to overionization (e.g., Ca: [Mashonkina et al. 2017](#); Ti: [Sitnova et al. 2020](#); Cr: [Bergemann & Cescutti 2010](#); Mn: [Bergemann & Gehren 2008](#); Fe: [Bergemann et al. 2012](#); Co: [Bergemann et al. 2010](#); Cu: [Korotin et al. 2018](#)). Few NLTE predictions have been made for the UV transitions examined here or the Fe-group elements in metal-poor, red horizontal-branch stars. The observed abundance behaviors are consistent with the magnitude and direction of the trends presented in the literature. The ionized fraction always dominates the neutral fraction for atoms of these elements in the atmosphere of HD 222925, so we regard the ions as more reliable abundance indicators.

Figure 1 also illustrates general properties among the Fe-group element abundances in HD 222925. Sc, Ti, and V are collectively enhanced relative to Fe. The correlated abundances among these three elements continue a trend among metal-poor stars identified by [Snedden et al. \(2016\)](#), [Cowan et al. \(2020\)](#), and [Ou et al. \(2020\)](#). Cr, Mn, Co, Ni, and Zn are found in approximately Solar ratios relative to Fe. Cu is subsolar relative to Fe, by  $\approx 0.6$  dex. All of these ratios are broadly consistent with general chemical-evolution patterns found among Milky Way stars at this metallicity, as summarized by [Roederer et al. \(2018b\)](#). Our results indicate that the elements with  $Z \leq 30$  in HD 222925 are typical for a metal-poor halo star.

### 3.6. Elements with $Z \geq 31$





**Figure 1.** Derived abundances for the elements with  $20 \leq Z \leq 30$  in HD 222925. The legend identifies the meanings of the symbols, and the dotted line represents the Solar ratio. The vertical error bars mark  $1\sigma$  statistical uncertainties. The points are slightly offset along the horizontal axis to improve clarity.

The UV spectrum of HD 222925 is rich in heavy-element absorption lines. We identify several rarely detected *r*-process elements, including Ga, Ge, As, Se, Cd, In, Sn, Sb, Te, W, Re, Os, Ir, Pt, and Au. We present evidence of their detection in Appendix A. Figures 2–4 illustrate the synthesis of representative lines of these and other species.

Table 3 presents our recommended abundances for each element. These values are considered on a case-by-case basis, including our best attempts to account for elements detected in multiple ionization states, poorly studied NLTE effects, missing or poor atomic data, problematic lines, small numbers of lines detected, and other issues. We encourage readers who are interested in the details of how we arrive at these recommended abundances to consult the relevant sections in Appendix A.

### 3.7. Uncertainties

All abundance uncertainties are computed following the method presented in Roederer et al. (2018b). We draw  $10^3$  samples from a normal distribution centered on the adopted value of each model atmosphere parameter, and interpolate a new model atmosphere for each of those draws. We approximate the equivalent width of each line through a reverse curve-of-growth analysis, based on the abundance derived from the spectrum synthesis. We draw  $10^3$  new equivalent widths for each line, assuming a normal distribution of uncertainties related to the S/N and the goodness of the synthetic spectrum fit. The  $\log(gf)$  of each line is also resampled  $10^3$  times from a normal distribution of uncertainties, based on NIST grades or uncertainties quoted in the original literature. New abundances are computed for each resample. The 16th and 84th percentiles of the resulting distributions are roughly symmetric, and the uncertain-

ties quoted in Tables 2 and 3 represent  $1\sigma$  uncertainties in the abundance ratios.

## 4. RESULTS

### 4.1. Elements Detected in HD 222925

A total of 63 elements are detected in HD 222925, plus H, which is detectable through the Balmer series lines, and He, which was detected previously by Navarrete et al. (2015). This tally includes 42 elements with  $31 \leq Z \leq 92$  produced by the *r*-process. We also report upper limits on the abundances of 7 elements, including 4 produced by the *r*-process. The rich UV and optical spectra of HD 222925 enable a nearly complete characterization of the *r*-process abundance pattern in a star whose atmosphere retains the heavy-element abundance pattern of its natal cloud.

These numbers represent a substantial improvement upon previous efforts. Among *r*-process-enhanced stars, for example, Hill et al. (2002), Plez et al. (2004), and Siqueira Mello et al. (2013) derived abundances for 37 *r*-process elements in CS 31082–001 (54 elements in total, plus H), Sneden et al. (2003) derived abundances for 31 *r*-process elements in CS 22892–052 (52 elements in total, plus H), and Roederer et al. (2012a, 2014c,d) derived abundances for 35 *r*-process elements in HD 108317 (52 elements in total, plus H). Among chemically peculiar stars with strong metal-line spectra, abundances have been derived for 51 elements (plus H) in the rapidly oscillating peculiar A (roAp) star HD 101065, also known as Przybylski’s star (Cowley et al. 2000), and abundances have been derived for 54 elements (plus H) in the bright metallic-line (Am) star Sirius (Landstreet 2011; Cowley et al. 2016). To the best of our knowledge, HD 222925 presents both the most complete set of *r*-process elements and the most complete set of abundances overall for any object beyond the solar system.

High-resolution UV spectroscopy is essential to this advance. Figures 5 and 6 illustrate this role in two complementary ways. Figure 5 illustrates the wavelengths of the lines that are detected and used to derive the abundances in the UV and optical spectra of HD 222925. It emphasizes the *number of lines* available in the UV spectrum. Figure 6 shows a periodic table that emphasizes the *number of elements* detectable in the UV region of the spectrum. Many of these elements are detected for the first time in a highly *r*-process-enhanced star. Abundances of some elements (e.g., Nb, Lu, Hf, Os, and Ir) are determined more reliably, because the UV spectral range presents a substantial increase in the number of lines available. Other elements (e.g., Al, Co, Ni, Cu, Mo, Ru, and Pb) benefit because the UV spectral range permits the detection of the dominant ionization state. The optical and near-infrared spectral ranges cannot replicate the rich diversity of lines found in the UV spectra of stars such as HD 222925.

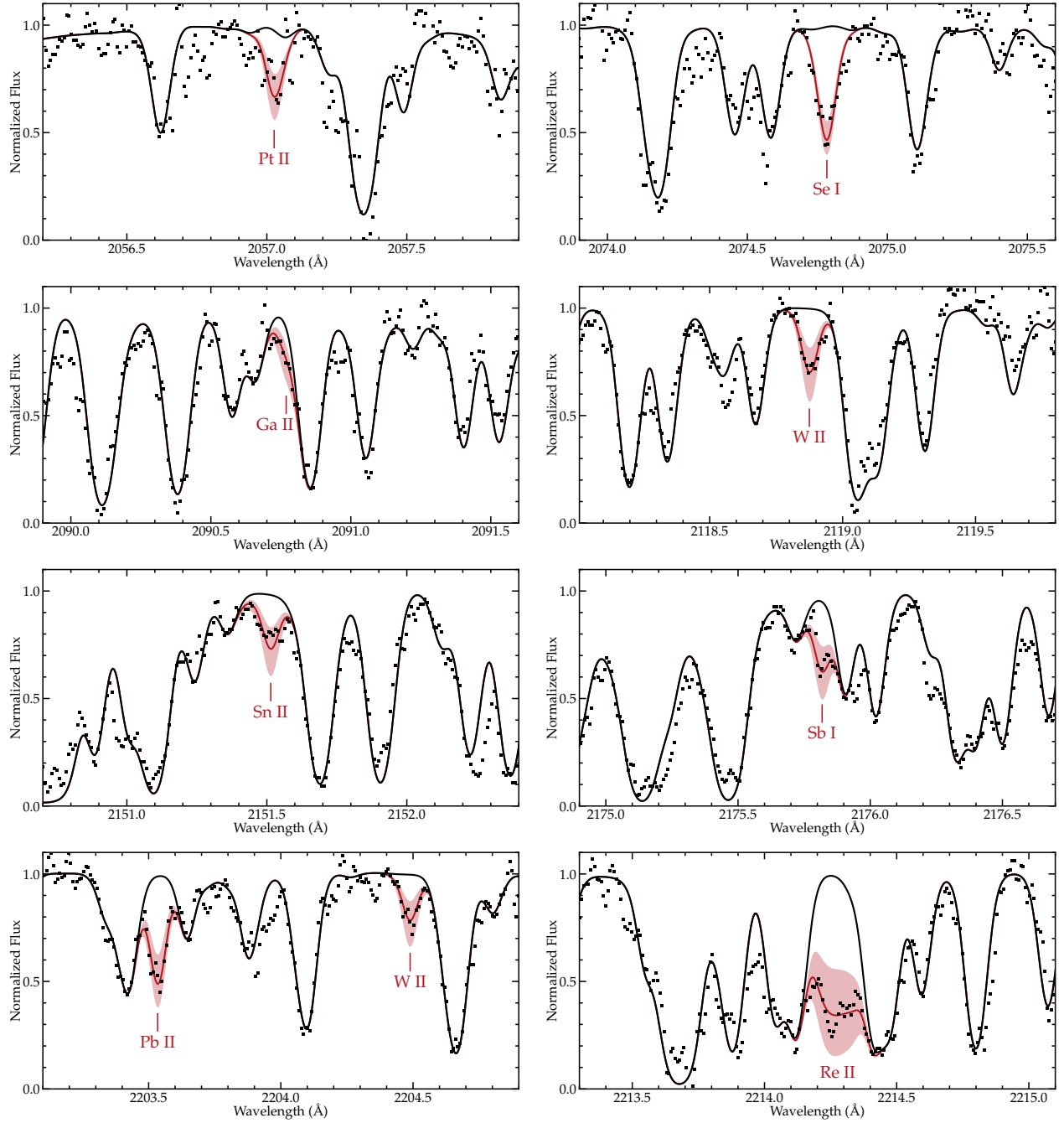


**Figure 2.** STIS E230H spectra of HD 222925 compared with model spectra around lines of interest, which are marked and labeled. The thick red line indicates the best-fit abundance for the line(s) of interest. The light red bands indicate variations in this abundance by  $\pm 0.3$  dex ( $\approx 1.5$ – $2.0$  times the typical uncertainties), to facilitate visibility. The thick black line indicates a model that excludes the element of interest.

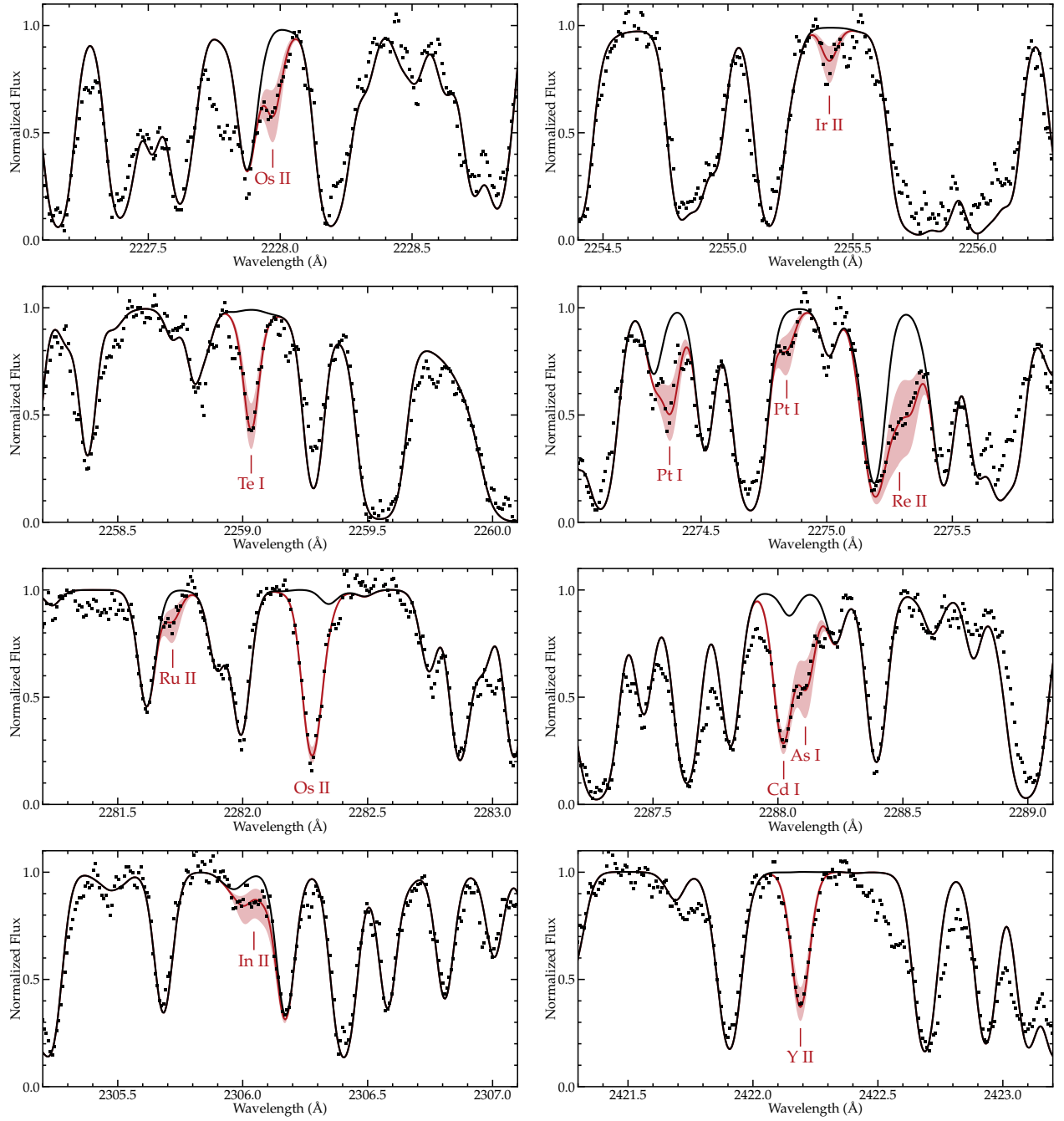


**Figure 3.** STIS E230H spectra of HD 222925 compared with model spectra around lines of interest. The symbols are the same as in Figure 2.

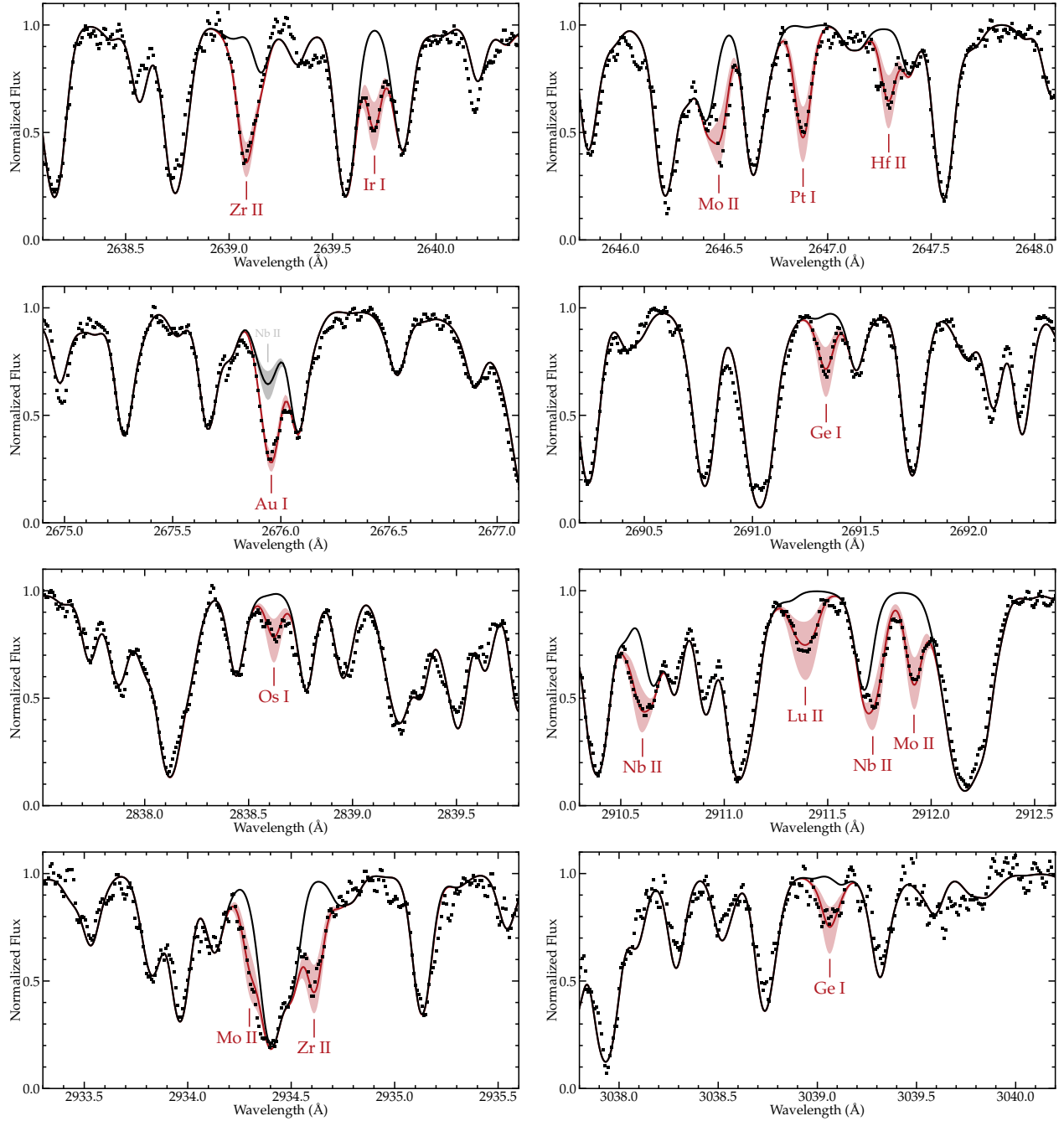


**Figure 4.** STIS E230H spectra of HD 222925 compared with model spectra around lines of interest. The symbols are the same as in Figure 2. The gray band in the second panel on the left marks a change in the blending Nb II line by its uncertainty,  $\pm 0.20$  dex.

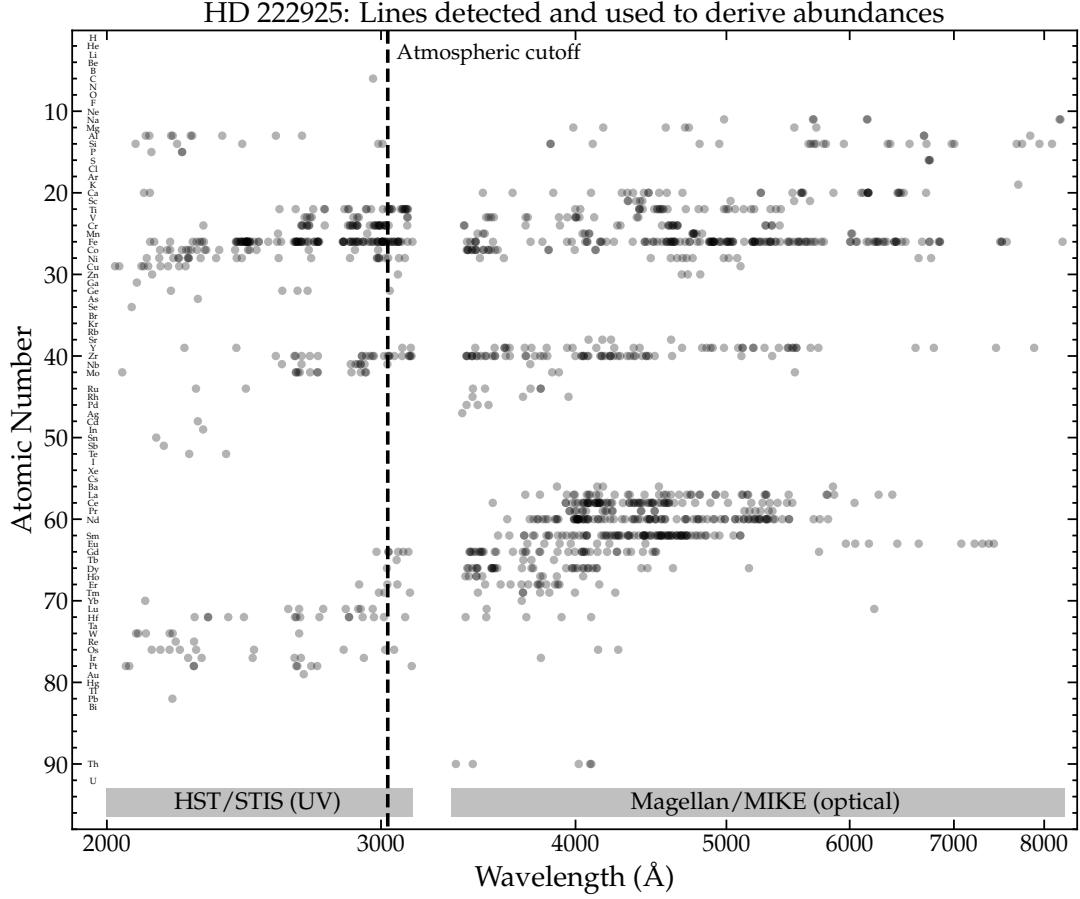


**Figure 5.** Illustration of the wavelengths of the lines that are detected and used to derive the abundances in HD 222925. Each dot represents a line. The atmospheric cutoff is marked and labeled. The gap between  $\approx 3145$  Å and  $\approx 3330$  Å reflects the gap between our STIS and MIKE spectra of HD 222925.

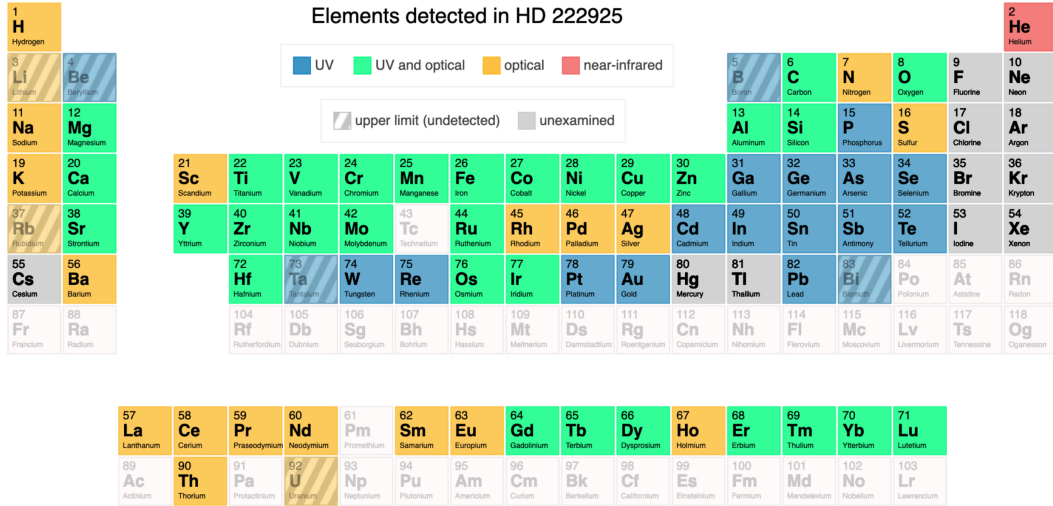


**Figure 6.** Periodic table showing the elements examined in HD 222925. Elements with no long-lived isotopes are indicated using light gray font. He was previously detected in near-infrared spectra by [Navarrete et al. \(2015\)](#).

#### 4.2. Elements Unexamined in HD 222925

Among all stable elements between H and U, only 11 remain unexamined in HD 222925: fluorine (F,  $Z = 9$ ), neon (Ne,  $Z = 10$ ), chlorine (Cl,  $Z = 17$ ), argon (Ar,  $Z = 18$ ), bromine (Br,  $Z = 35$ ), krypton (Kr,  $Z = 36$ ), iodine (I,  $Z = 53$ ), xenon (Xe,  $Z = 54$ ), cesium (Cs,  $Z = 55$ ), mercury (Hg,  $Z = 80$ ), and thallium (Tl,  $Z = 81$ ). These elements are labeled as “unexamined” in Figure 6. Their neutral and ionized species present no transitions in optical or UV spectra with a realistic chance of detection. Elements with no long-lived isotopes also remain unexamined in HD 222925: technetium (Tc,  $Z = 43$ ), promethium (Pm,  $Z = 61$ ), polonium through actinium (Po–Ac,  $Z = 84$ –89), protactinium (Pa,  $Z = 91$ ), and all transuranic elements ( $Z \geq 93$ ).

We predict that two more elements, I and Hg, may be detectable in HD 222925. The I I line at 2061.633 Å is blended with a strong Cr II line, but I I lines at 1830.380 and 1844.453 Å may be strong enough to permit detections. The Hg II resonance line at 1942.273 Å is in a region of our UV spectrum where the S/N is too low to permit a reliable detection, and the Hg I resonance line at 2536.521 Å is too blended to detect or derive an upper limit. Future UV observations with a more sensitive telescope should enable detection of the I I  $\lambda\lambda$ 1830 and 1844 and the Hg II  $\lambda$ 1942 lines in HD 222925.

#### 4.3. The $R$ -process Abundance Pattern

Figure 7 illustrates the heavy-element abundance pattern of HD 222925. The red line marks the Solar  $r$ -process residuals,<sup>2</sup> scaled downward by 0.11 dex to match the Eu abundance in HD 222925. The Solar  $r$ -process residuals and the observed pattern are in near-perfect agreement for the elements with  $Z \geq 56$ . The mean difference is  $-0.05 \pm 0.02$  dex ( $\sigma = 0.08$  dex, or 17%). Ho is the most discrepant,  $0.23 \pm 0.12$  dex below the scaled Solar  $r$ -process residual pattern. This difference is  $< 2\sigma$  significant. As discussed in Appendix A.31, we find no reason to discount our Ho abundance derivation.

The elements with  $Z \leq 52$  behave differently. The deviations from the  $r$ -process residuals for the lighter elements span nearly 1.4 dex from As ( $-1.15$  dex) to Nb ( $+0.24$  dex), regardless of the overall normalization. The deviations do not appear to be random, and three general trends emerge.

First, the lightest elements in this region, Ga, Ge, and As ( $31 \leq Z \leq 33$ ), are deficient by more than 0.8 dex relative to the scaled Solar  $r$ -process pattern. The abundance of Se ( $Z = 34$ ), an element at the first  $r$ -process peak, agrees with the scaled Solar residual pattern.

Secondly, there is an overall decrease in the HD 222925 pattern relative to the  $r$ -process residuals for Nb through Cd ( $41 \leq Z \leq 48$ ). The even- $Z$  element Cd is also unusual in that its abundance is comparable to or less than its odd- $Z$  neighbors, Ag and In ( $Z = 47$  and 49). As discussed in Appendix A.26, we find no reason to discount our Cd abundance derivation.

Finally, In, Sn, and Sb ( $49 \leq Z \leq 51$ ), detected here for the first time in an  $r$ -process-enhanced star, lie either on the pattern (In, Sn) or slightly below it (Sb) when normalizing to Eu. Te ( $Z = 52$ ), an element at the second  $r$ -process peak, is deficient by 0.40 dex.

### 5. DISCUSSION

We begin by introducing several general environmental and chemical properties of HD 222925 that inform our discussion of its heavy-element abundance pattern.

1. HD 222925 is on an eccentric orbit with pericenter near  $1.0 \pm 0.1$  kpc, apocenter near  $16.6 \pm 0.6$  kpc, and maximum distance above the Galactic plane of  $5.3 \pm 0.1$  kpc (Roederer et al. 2018a). Its azimuthal angular momentum is small and retrograde,  $J_\phi = -L_z = -380 \pm 40$  kpc km s $^{-1}$ , suggesting that HD 222925 was accreted by the Milky Way, perhaps from a satellite or star cluster associated with the Gaia Sausage/Enceladus galaxy (Belokurov et al. 2018; Helmi et al. 2018) that was accreted at least  $\approx 10$  Gyr ago (Feillet et al. 2021; Montalbán et al. 2021).
2. HD 222925 does not show evidence of radial velocity variations over more than 7 yr of observations (Appendix B), indicating it is not likely to be in a binary or multiple-star system.
3. All light ( $Z \leq 30$ ) elements in HD 222925 exhibit abundance ratios typical for halo stars with  $[\text{Fe}/\text{H}] \approx -1.5$ , indicating that the production of these elements was dominated by normal Type II supernovae. Neither C nor N are enhanced in HD 222925 ( $[\text{C}/\text{Fe}] = +0.14 \pm 0.17$ ,  $[\text{N}/\text{Fe}] = +0.08 \pm 0.21$ ). The  $\alpha$  elements O, Mg, Si, S, Ca, and Ti are enhanced relative to Fe,  $[\alpha/\text{Fe}] = +0.32 \pm 0.03$ . As discussed in Appendix A.1, only the He abundance is potentially anomalous in HD 222925.
4. The metallicity of HD 222925,  $[\text{Fe}/\text{H}] = -1.46 \pm 0.10$ , is higher than most known  $r$ -process-enhanced stars, which suggests that multiple supernovae have contributed to the lighter elements in HD 222925. We follow Roederer et al. (2018b) in assuming that a single  $r$ -process event dominated the heavy-element enrichment of the gas from which HD 222925 formed. As discussed there, any  $s$ -process contributions from asymptotic giant branch (AGB) stars are minimal compared to the  $r$ -process material.

#### 5.1. The First $R$ -process Peak

<sup>2</sup> The Solar abundances listed in Table 1 of Sneden et al. (2008) should include  $\text{N}[\text{s}] = 0.055$  and  $\text{N}[\text{r}] = 0.172$  for  $^{99}\text{Ru}$  and  $\text{N}[\text{r}] = 0.373$  for  $^{136}\text{Xe}$  (J. Cowan 2022, private communication).



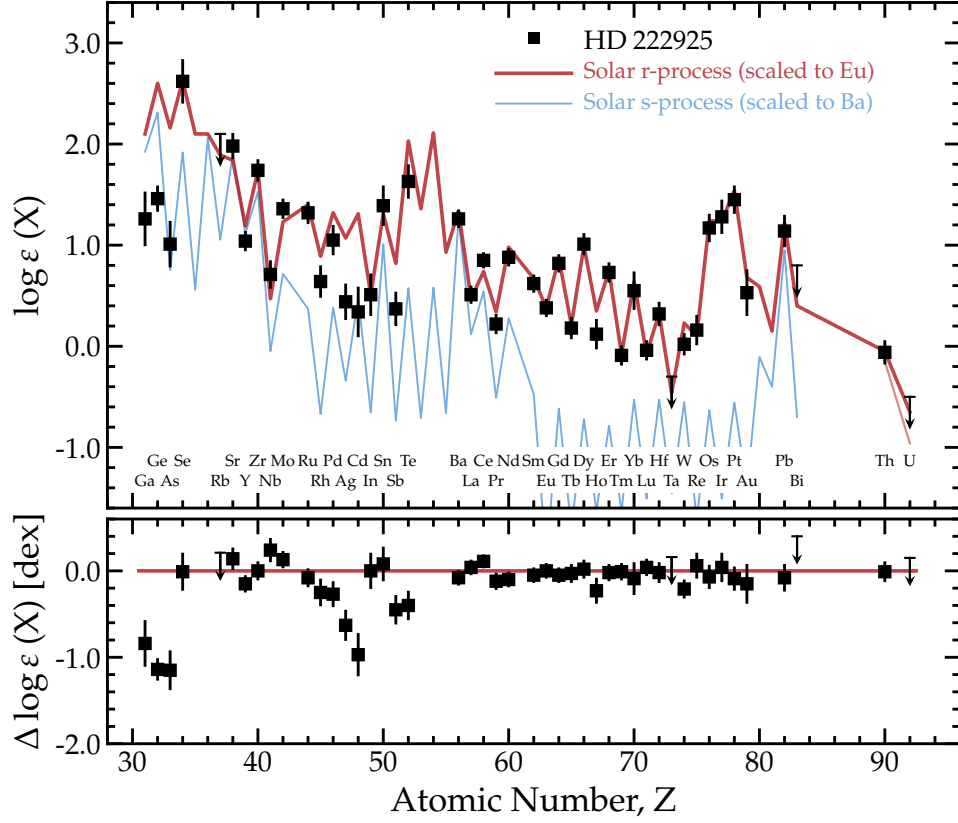


**Figure 7.** Top: the  $r$ -process abundance pattern in HD 222925. The Solar  $s$ -process pattern (the thin blue line, scaled to match the Ba abundance) and the  $r$ -process residuals (the thick red line, scaled to match the Eu abundance) are shown for comparison (Snedden et al. 2008, except Y, which is adopted from Bisterzo et al. 2014). The detected elements are marked by the filled black squares, and the upper limits derived from non-detections are marked by the arrows. The light red line at Th and U accounts for 13 Gyr of radioactive decay; i.e., 8.5 Gyr of additional decay relative to the Solar abundances. Bottom: the difference between the HD 222925 abundances and the Solar  $r$ -process residuals when scaled to Eu.

The first  $r$ -process peak is expected to occur around mass number  $A \sim 80$ , Se to Kr, comprising the stable  $\beta$ -decay products of radioactive nuclei at the  $N = 50$  closed neutron shell along the  $r$ -process path. The elements just below the first  $r$ -process peak, Ga, Ge, and As, are deficient by more than 1 dex relative to Se:  $\log \varepsilon(\text{Se}/\text{Ga}) = +1.36 \pm 0.35$ ,  $\log \varepsilon(\text{Se}/\text{Ge}) = +1.16 \pm 0.25$ , and  $\log \varepsilon(\text{Se}/\text{As}) = +1.61 \pm 0.32$ . We investigate in this section the  $r$ -process contributions to each of these elements.

Figure 8 illustrates the Fe group and first few trans-Fe-group elements from four  $r$ -process-enhanced stars, along with the Solar abundances. These are the only four  $r$ -process-enhanced stars in which Se has been detected. In massive stars, Fe-group elements are produced during explosive  $^{28}\text{Si}$  burning, which produces the familiar shape of the Fe peak. The even- $Z$  elements fall off in abundance away from Fe, as indicated by the dashed lines. At the light end, Ca sits above the line, indicating that another process,  $\alpha$ -capture, dominates its production. Se exhibits a similar upturn relative to the

downward trend of even- $Z$  abundances heavier than Fe. We follow Roederer et al. (2014d) in proposing that this excess of Se is due to  $r$ -process nucleosynthesis. The four stars shown in Figure 8 have a range of  $[\text{Eu}/\text{Fe}]$  ratios, and thus  $r$ -process enhancement levels, ranging from  $-0.02$  to  $+1.32$  dex. There is a clear sequence in the Se abundances in that the highest  $[\text{Se}/\text{Fe}]$  ratio is found in HD 222925, the star with the highest  $[\text{Eu}/\text{Fe}]$  ratio, and the lowest  $[\text{Se}/\text{Fe}]$  ratio is found in HD 128279, the star with the lowest  $[\text{Eu}/\text{Fe}]$  ratio.

We conclude that the  $r$ -process dominates production in the mass range that includes Se,  $76 \leq A \leq 80$ . Some of the Ga, Ge, and As in HD 222925 could also have originated in the  $r$ -process, and some may have been produced by (neutron-rich)  $\alpha$ -rich freezeout from nuclear statistical equilibrium in the supernovae that produced the Fe-group elements (Woosley & Hoffman 1992). This result is compatible with the finding by Cowan et al. (2005) that Ge abundances in metal-poor stars correlate more closely with Fe than Eu.

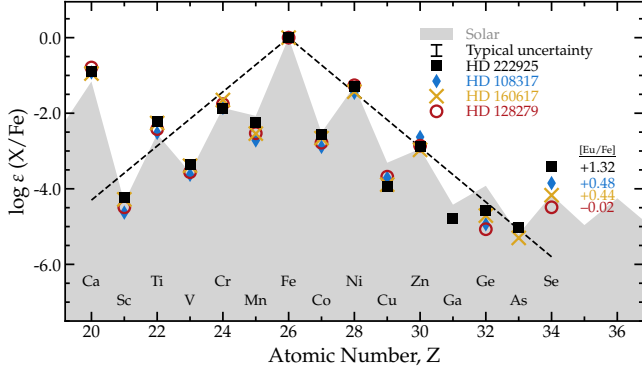


**Figure 8.** Abundances near the Fe peak in the solar system and four metal-poor stars. The abundance patterns are normalized to  $\log \varepsilon(\text{Fe}) = 0.0$ .  $[\text{Eu}/\text{Fe}]$  ratios are indicated for the four metal-poor stars next to their Se abundances. The data are taken from Roederer et al. (2012a, 2014d) for HD 108317 and HD 128279 and Roederer & Lawler (2012) for HD 160617. The dashed lines approximately follow the decline in the abundances of the even- $Z$  elements on either side of the Fe peak. The Se abundances in the metal-poor stars, especially HD 222925, are far in excess of this extrapolation.

This result has implications for the origin of Ga, Ge, As, and Se in the solar system. We present a toy model that assumes that all  $r$ -process material in the solar system originated in events identical to the one that enriched HD 222925. Figure 9 illustrates the total Solar elemental abundance distribution (Lodders et al. 2009) from Ga to Te. We adopt the  $s$ -process abundances from Bisterzo et al. (2011, 2014), who calculated the  $s$ -process fraction of each element from AGB stellar models and Galactic chemical-evolution models. Our model substitutes the HD 222925  $r$ -process pattern in place of the traditional  $r$ -process residuals. HD 222925 is not physically related to the solar system, so the relative scaling of the  $s$ -process and  $r$ -process patterns is not known a priori. We scale the  $r$ -process pattern upward to the maximum extent permitted, without overpredicting any Solar abundance beyond its uncertainty: for a shift of +0.40 dex, In is overproduced by  $0.21 \pm 0.21$  dex. Note that this shift is unrelated to the  $-0.11$  dex shift applied in Section 4.3 to match the Solar  $r$ -process abundance of Eu to the HD 222925 Eu abundance. Our toy model sets an *upper limit* on the allowable  $r$ -process contribution to the Solar abundances of lighter  $r$ -process elements from Ga to Te.

The purple band in panel (a) of Figure 9 represents the sum of the scaled  $r$ -process abundance pattern from HD 222925 and the  $s$ -process abundance pattern from the Bisterzo et al. (2014) Galactic chemical evolution model, hereafter the “ $r+s$ ” pattern. It includes uncertainties from the  $s$ -process model, observational uncertainties in the  $r$ -process abundance pattern, and uncer-

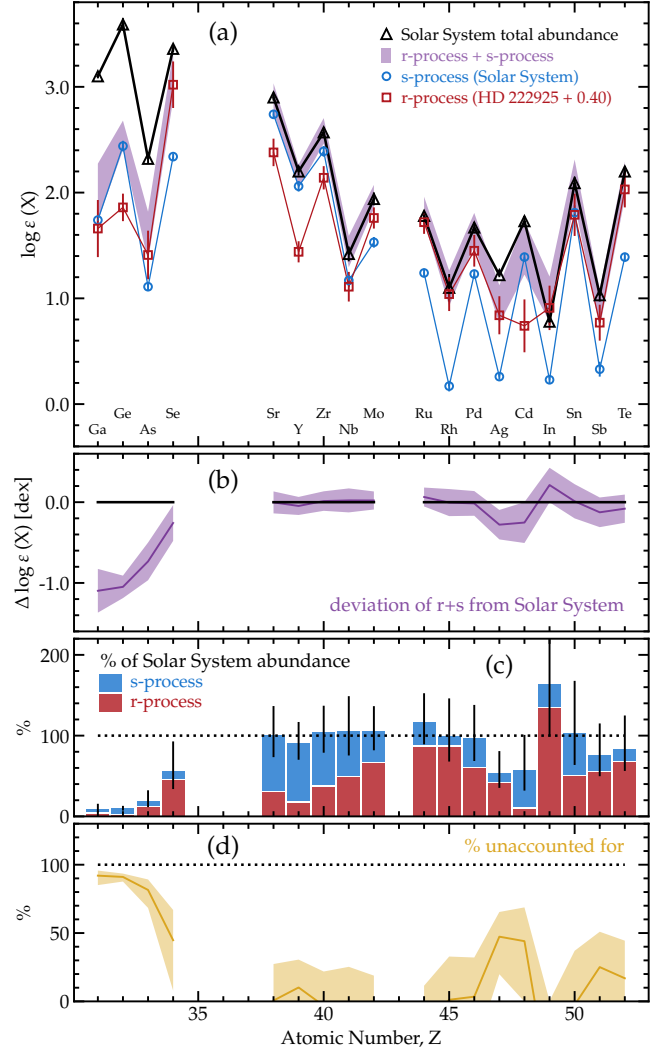


**Figure 9.** Panel (a): abundances of elements from Ga to Te in the solar system (Lodders et al. 2009; black triangles), excluding elements that are not detected in HD 222925. The AGB  $s$ -process contribution to the Solar abundances (Bisterzo et al. 2011 for Ga through Se, Bisterzo et al. 2014 for all others) is shown with blue circles; the  $r$ -process abundances derived from HD 222925, scaled by +0.40 dex, are shown as red squares; and the sum of the  $r$ -process and  $s$ -process abundances, with  $\pm 1\sigma$  uncertainties, are shown as the purple band. Panel (b): the difference between the summed  $r$ -process and  $s$ -process abundances (the purple line and band) and the total Solar abundances (the black line). Panel (c): percentage contributions by the  $r$ -process (red) and  $s$ -process (blue) to the total Solar abundances. The dotted line marks 100%. Panel (d): percentage contributions (yellow band) that are unaccounted for by either the  $r$ -process or  $s$ -process. The dotted line marks 100%.

tainties in the Solar abundances. Panel (b) of Figure 9 illustrates that this  $r+s$  pattern provides an acceptable fit to most of the Solar abundances. Panel (c) of Figure 9 shows the percentages of the Solar abundances contributed by each of the  $r$ -process and  $s$ -process. We emphasize that the  $r$ -process percentages in panel (c) represent upper limits on the contribution to the solar system from  $r$ -process events, such as the one that enriched the gas from which HD 222925 formed.

Panel (d) of Figure 9 illustrates the elements for which the  $r$ -process and AGB  $s$ -process contributions are insufficient to account for the Solar abundances. The maximum  $r$ -process contributions to Ga, Ge, and As are  $4^{+4}_{-2}\%$ ,  $1.6^{+0.6}_{-0.4}\%$ , and  $13^{+9}_{-5}\%$ , respectively. This finding is consistent with previous work (e.g., Fröhlich et al. 2006; Pignatari et al. 2010; Wanajo et al. 2011; Roederer 2012; Niu et al. 2014; Kobayashi et al. 2020), which showed that the origins of the Solar Ga, Ge, and As are dominated by other nucleosynthesis processes. The  $r$ -process accounts for roughly half of the Se abundance,  $48^{+31}_{-20}\%$ , indicating that substantial  $r$ -process contributions start at Se.

### 5.2. The Second $R$ -process Peak

The second  $r$ -process peak is expected to occur around mass number  $A \sim 130$ , Te to Xe, comprising the stable  $\beta$ -decay products of radioactive nuclei at the  $N = 82$  closed neutron shell along the  $r$ -process path. The Te abundance lies 0.40 dex lower than the Solar  $r$ -process residuals when the Solar pattern is scaled to match Eu. The Sn abundance in HD 222925 is nearly as high as the Te abundance,  $\log \varepsilon(\text{Te}/\text{Sn}) = +0.24 \pm 0.24$ , whereas the Solar  $r$ -process residuals anticipate a value of  $+0.36$  or  $+0.72$  (Bisterzo et al. 2014 and Sneden et al. 2008, respectively). Conversely, the  $\log \varepsilon(\text{Sn}/\text{Cd})$  ratio in HD 222925 is high,  $+1.05 \pm 0.26$ , whereas the Solar  $r$ -process residuals anticipate a value of  $+0.31$  or  $+0.00$ . We caution that the Sn abundance is derived from a single line, and our identification of this line is less secure than others (Section A.28).

These discrepancies could signal the need for further improvements in nuclear structure models, and nuclear masses in particular, for nuclei just below the  $A \sim 130$  peak (see Kratz et al. 2014). For example, the Sn and Sb behavior is consistent with a recent measurement by Li et al. (2021) that improved the uncertainty on the mass of the neutron-rich isotope  $^{123}\text{Pd}$ . That measurement implies a slight decrease in the  $r$ -process abundance of the  $A = 123$  isobar, which is linked to one of only two stable Sb isotopes. It also corresponds to a slight enhancement in the  $A = 122$  isobar, and we propose that the impact of this enhancement on the Sn abundance may be minimal, because  $^{122}\text{Sn}$  comprises only one of six stable Sn isotopes accessible to the  $r$ -process.

Another possible interpretation of these discrepancies could be that the second  $r$ -process peak is shifted to lower mass numbers by  $\approx 2$ –4 mass units compared to

the Solar pattern. Simulations of  $r$ -process nucleosynthesis suggest that the shape and placement of the second peak depends sensitively on the astrophysical conditions. The electron fraction and entropy of the outflow determine the position of the  $r$ -process path on the nuclear chart, and the initial placement of the peak is set by the neutron-richness of the  $N = 82$  closed shell nuclei populated along the path (Meyer & Brown 1997). How quickly the temperature and density drop as a function of time determines how rapidly the  $r$ -process freezes out of the  $(n, \gamma)$ – $(\gamma, n)$  equilibrium, with the final placement and width of the peak set by late-time neutron capture (Surman & Engel 2001; Surman et al. 2009; Arcones & Martínez-Pinedo 2011). The neutron-richness of the conditions also determines whether fissioning nuclei are reached; if so, the second peak is shaped in part by the deposition of fission products (Eichler et al. 2015; Vassh et al. 2019; Lemaître et al. 2021; Sprouse et al. 2021). Therefore, the discrepancy noted here is intriguing, and calls for new comparisons between models and observations for elements around the second  $r$ -process peak.

### 5.3. The Lanthanides

The lanthanide elements span  $57 \leq Z \leq 71$ , La to Lu, which are also known as rare-earth elements. The lanthanide fraction,  $X_{\text{La}}$ , is the mass ratio between the lanthanides and all  $r$ -process elements. We calculate  $X_{\text{La}} = 0.041 \pm 0.008$ , or  $\log X_{\text{La}} = -1.39 \pm 0.09$ , for HD 222925. This value matches the means of the distributions calculated by Ji et al. (2019) for other highly  $r$ -process-enhanced stars,  $\log X_{\text{La}} = -1.55 \pm 0.3$ , using the same Solar  $r$ -process distribution from Sneden et al. (2008), or  $\log X_{\text{La}} = -1.44 \pm 0.3$ , using one from Arnould et al. (2007) that yields slightly reduced contributions to Ga and Ge.

This calculation requires the abundances of elements that are undetected or unexamined in HD 222925. We estimate their abundances by extrapolating from neighboring elements using the Solar  $r$ -process residuals. We rely less on these extrapolations than previous work did. Our estimate of the lanthanide fraction in a metal-poor star is the first wherein a majority of the mass of  $r$ -process elements have been detected directly. The elements detected in HD 222925 comprise  $\approx 70\%$  of the mass of the  $r$ -process elements. Without UV spectra we would have only been able to detect elements that comprise  $\approx 25\%$  of the mass of  $r$ -process elements. The availability of high-quality UV spectra thus greatly reduces the systematic uncertainties in the calculation of  $X_{\text{La}}$ .

The lanthanide elements dominate the opacity in  $r$ -process-rich kilonovae emerging from merging pairs of neutron stars (e.g., Kasen et al. 2013), so kilonova light curves are sensitive to the lanthanide fraction of material ejected from the mergers. The lanthanide fraction in HD 222925 is higher, by a factor of  $\sim 6$ , than that of the kilonova associated with GW170817,

$\log X_{\text{La}} \approx -2.2 \pm 0.5$  (Ji et al. 2019). This difference maintains the tension identified by Ji et al. between the lanthanide fraction in highly  $r$ -process-enhanced stars and this particular kilonova. This tension could signal the operation of another dominant source of  $r$ -process elements in the early universe, such as magnetorotational hypernovae (e.g., Yong et al. 2021a), if observations of future kilonovae fail to detect events with lanthanide fractions higher than that found in the GW170817 event.

#### 5.4. The Third $R$ -process Peak, Lead, and Actinides

The third  $r$ -process peak is expected to occur around mass number  $A \sim 195$ , Os to Pt, comprising the stable  $\beta$ -decay products of radioactive nuclei at the  $N = 126$  closed neutron shell along the  $r$ -process path. The third-peak element abundances in HD 222925 are in superb agreement with the Solar  $r$ -process residuals. Our detections of W, Re, and Au confirm that the Solar  $r$ -process residuals accurately reflect the rise and fall of the third-peak abundances, as well as the placement of the third peak near  $A \sim 195$ .

Pb is the heaviest stable element detected in HD 222925. Pb is unique among  $r$ -process elements because it mostly ( $> 85\%$ ; Cowan et al. 1999) formed through the decay of radioactive nuclei with  $A > 209$ , including the long-lived isotopes of Th and U. Roederer et al. (2020) used the Th/Pb chronometer to calculate an age of  $8.2 \pm 5.8$  Gyr for the  $r$ -process material in HD 222925. This calculation is relatively insensitive to the details of the  $r$ -process model, because of the close link between Pb and Th production. See Roederer et al. for further discussion of the prospects for using the Th/Pb ratio as an age indicator, provided that the Pb II line can be detected in UV spectra of more  $r$ -process-enhanced stars.

#### 5.5. Future Prospects

More than a quarter century has passed since the discovery of the first highly  $r$ -process-enhanced star, CS 22892-052, by Sneden et al. (1994). HD 222925 remains the only star in this class that is bright enough in the UV for high-quality spectroscopy at wavelengths as short as 2000 Å to be practicable. Identifying additional bright  $r$ -process-enhanced stars is one of the major goals of the RPA. More than 60 highly  $r$ -process-enhanced stars are already known with  $V > 12$ , as shown in Figure 10. A majority of these stars have been identified by the RPA in only the last 5 yr. All of these stars would potentially be observable by the large UV-optical-infrared flagship mission recently recommended by the Astro2020 Decadal Survey (National Academies 2021) for launch in the 2040s. While awaiting that transformative development, we encourage continued investment to maximize the operational lifetimes of STIS and HST.

## 6. CONCLUSIONS

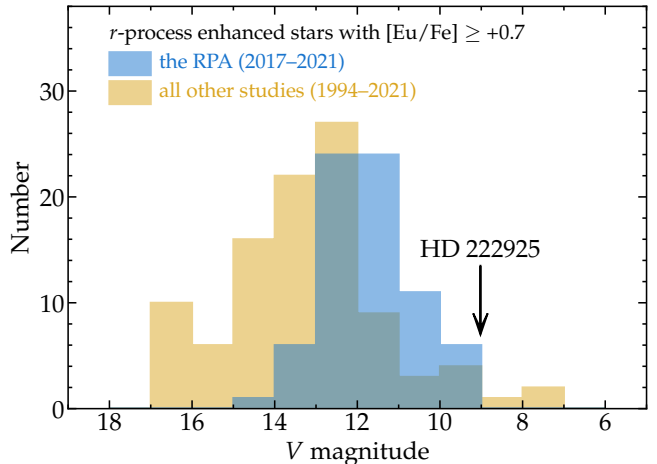


**Figure 10.** Histogram showing the magnitude distribution of highly  $r$ -process-enhanced stars, here defined as those with  $[\text{Eu}/\text{Fe}] \geq +0.7$  (Holmbeck et al. 2020). The three stars brighter than HD 222925 in the  $V$  band, HD 115444 (Westin et al. 2000), HD 120559 (Hansen et al. 2012), and HD 221170 (Ivans et al. 2006), are all fainter than HD 222925 in the GALEX  $NUV$  band. Data for these 181 stars have been compiled from more than 40 literature sources, including Barklem et al. (2005), Ezzeddine et al. (2020), Hansen et al. (2018), Holmbeck et al. (2020), Howes et al. (2016), Ishigaki et al. (2013), Jacobson et al. (2015), Rasmussen et al. (2020), Roederer et al. (2014a), Sakari et al. (2018), and Yong et al. (2021b).

We have collected new high-resolution UV spectra of the bright,  $r$ -process-enhanced, metal-poor star HD 222925. We use a standard LTE abundance analysis to derive abundances from 404 lines in these spectra, and we merge our results with ones derived from 908 lines in an optical spectrum. We summarize our main results and findings as follows.

1. HD 222925 presents the most complete chemical inventory of any object beyond the solar system. We detect 63 metals in HD 222925, including 42 elements produced by the  $r$ -process. These detections include a number of  $r$ -process elements that are rarely detected in stars, including Ga, Ge, As, Se, Cd, In, Sn, Sb, Te, W, Re, Os, Ir, Pt, and Au. We report upper limits on the abundances of seven other elements not detected in our spectra. We critically evaluate these abundances and produce a set of recommended abundances, which is presented in Table 3.
2. The  $r$ -process elements with  $31 \leq Z \leq 52$  do not generally match the Solar  $r$ -process residuals, regardless of how they are scaled (Figure 7).
3. The  $r$ -process contributes a small amount to Ga, Ge, and As ( $31 \leq Z \leq 33$ ). In the solar system, less than  $\approx 4\%$ ,  $\approx 2\%$ , and  $\approx 13\%$ , respectively, of



these elements originated in  $r$ -process nucleosynthesis events like the one that enriched the gas from which HD 222925 formed (Figure 9).

4. Se ( $Z = 34$ ) is the lightest element with a substantial contribution from the  $r$ -process in both HD 222925 and the solar system (Figures 8 and 9).
5. There is a gradual downward trend relative to the Solar  $r$ -process residuals from Nb through Cd ( $41 \leq Z \leq 48$ ; Figure 7).
6. The elements Sb and Te ( $Z = 51$  and  $52$ , respectively) at the second  $r$ -process peak are deficient by  $\approx 0.4$  dex relative to the Solar  $r$ -process residuals when scaled to Eu. The elements just below the second  $r$ -process peak, In and Sn ( $Z = 49$  and  $50$ , respectively), match the Solar  $r$ -process residuals (Figure 7). This behavior could indicate that the second  $r$ -process peak is shifted to lower mass numbers by  $\approx 2$ – $4$  mass units. Improvements in nuclear structure models and new experiments will play an important role in interpreting this behavior.
7. The  $r$ -process elements with  $Z \geq 56$  (Ba and heavier) present a near-perfect abundance match to the Solar  $r$ -process residuals when scaled to match the Eu abundance (Figure 7). This agreement includes all elements surrounding the third  $r$ -process peak from Re to Au ( $75 \leq Z \leq 79$ ) and Pb ( $Z = 82$ ), which is formed mainly through radioactive decay of heavier isotopes.
8. The HD 222925 lanthanide fraction,  $\log X_{\text{La}} = -1.39 \pm 0.09$ , is normal for highly  $r$ -process-enhanced stars (Ji et al. 2019), and it relies far less than previous estimates on extrapolations using the Solar  $r$ -process residuals. This lanthanide fraction is higher, by a factor of  $\sim 6$ , than that inferred from the kilonova observed after the merger of two neutron stars in the GW170817 gravitational-wave event (Section 5.3).

HD 222925 exhibits no remarkable characteristics in its chemical abundance pattern, other than the overall enhancement of  $r$ -process elements. Thus, it may be considered as reflecting the yields of the dominant  $r$ -process source(s) in the early universe. This nearly complete  $r$ -process abundance template provides an alternative to the elemental Solar  $r$ -process residuals for confronting future theoretical models of heavy-element nucleosynthesis with observations; we eagerly anticipate the results of those new comparisons.

## ACKNOWLEDGMENTS

We appreciate the work of P. Royle, S. Deustua, and the staff at the STScI for their attention to the observing challenges encountered in October, 2019, and for their sustained dedication to improving the quality of STIS observations. This project would not have been possible without their persistence. I.U.R. thanks C. Cowan and M. Pignatari for discussions of the Solar abundance pattern, and R. Peterson for sharing results in advance of publication. We thank the referee for helpful comments on our work. We acknowledge generous support provided by NASA through grants GO-15657 and GO-15951 from the Space Telescope Science Institute, which is operated by the Association of Universities for Research in Astronomy, Incorporated, under NASA contract NAS5-26555. We acknowledge support awarded by the U.S. National Science Foundation (NSF): grants PHY 14-30152 (Physics Frontier Center/JINA-CEE), OISE 1927130 (International Research Network for Nuclear Astrophysics/IReNA), AST 1716251 (A.F.), and AST 1815403 (I.U.R.). I.U.R. acknowledges support from the NASA Astrophysics Data Analysis Program, grant 80NSSC21K0627. R.S. acknowledges support from grant DE-FG02-95-ER40934 awarded by the U.S. Department of Energy. The work of V.M.P. is supported by NOIRLab, which is managed by AURA under a co-operative agreement with the NSF. This research has made use of NASA’s Astrophysics Data System Bibliographic Services; the arXiv preprint server operated by Cornell University; the SIMBAD and VizieR databases hosted by the Strasbourg Astronomical Data Center; the ASD hosted by NIST; the MAST at STScI; and Image Reduction and Analysis Facility (IRAF) software packages distributed by the National Optical Astronomy Observatories, which are operated by AURA, under cooperative agreement with the NSF.

*Facility:* HST (STIS), Magellan (MagE, MIKE)

*Software:* IRAF (Tody 1993), LINEMAKE (Placco et al. 2021), matplotlib (Hunter 2007), MOOG (Snedden 1973; Sobeck et al. 2011), numpy (van der Walt et al. 2011), scipy (Jones et al. 2001)

## APPENDIX

## A. DISCUSSION OF INDIVIDUAL LINES AND SPECIES

In this Appendix, we discuss individual lines of interest, with an emphasis on the availability of atomic data relevant to the derivation of stellar abundances. We also discuss the agreement among abundance indicators and upper limits derived from nondetections.

### A.1. Hydrogen ( $H$ , $Z = 1$ ) and Helium ( $He$ , $Z = 2$ )

We detect H directly through the Balmer series transitions in the optical spectrum of HD 222925. The  $H^-$  ion also forms the dominant source of continuous opacity in the optical and UV. Navarrete et al. (2015) detected the near-infrared He I line at 10830 Å in HD 222925. Those authors did not derive the He abundance, but they noted that the equivalent width of this line,  $\approx 230$  mÅ, is about 5–6 times larger than that of other stars in their field-star sample. It is unclear why the He I line is so strong. Navarrete et al. postulated that it could be related to chromospheric activity. HD 222925 exhibits other signs of chromospheric activity, including emission in the cores of the Mg II resonance doublet at 2800 Å, similar to other old, metal-poor, red giants (Dupree et al. 2007). Further study of this He I line would be worthwhile.

### A.2. Lithium ( $Li$ , $Z = 3$ ), Beryllium ( $Be$ , $Z = 4$ ), and Boron ( $B$ , $Z = 5$ )

We detect no lines of the light element Li. We adopt an upper limit on its abundance from Roederer et al. (2018b),  $\log \varepsilon(Li) < 0.80$ , derived from nondetection of the Li I line at 6707.80 Å. This fragile element is diluted and then destroyed when a star, such as HD 222925, evolves into a red giant and horizontal-branch star (e.g., Charbonnel 1995). Our upper limit is compatible with observations of other evolved, metal-poor stars, which show  $\log \varepsilon(Li) \leq 1$  along the upper red giant branch (e.g., Gratton et al. 2000; Lind et al. 2009; Kirby et al. 2016).

We detect no lines of the light elements Be or B, either. Upper limits from several lines are reported in Table 1. Absorption is detected at 2089.56 Å, near the wavelength of a B I line at 2089.570 Å. No absorption that can plausibly be attributed to B I is detected at the wavelengths of other B I lines at 2088.889, 2496.769, or 2497.722 Å, however, so we conclude that B I is undetected in our spectrum of HD 222925. We report upper limits in Table 1.

### A.3. Carbon ( $C$ , $Z = 6$ )

We detect a reasonably unblended line of C I at 2964.846 Å. The NIST ASD lists a  $\log(gf)$  for this line with a D grade. The abundance derived from this line,  $\log \varepsilon(C) = 6.70 \pm 0.34$ , is in good agreement with the C abundance derived from the CH “G” band,  $\log \varepsilon(C) = 6.65 \pm 0.17$ . Given the large uncertainty in the  $\log(gf)$  value of the C I UV line, our recommended C abundance relies on the abundance derived from the CH “G” band. We correct this value by +0.46 dex for stellar evolution effects, as described in Placco et al. (2014). The corrected value is listed in Table 3.

### A.4. Nitrogen ( $N$ , $Z = 7$ )

No atomic or molecular N features are detected in our UV spectrum of HD 222925. Our recommended N abundance is based on that derived from NH molecular bands detected by Roederer et al. (2018b).

### A.5. Oxygen ( $O$ , $Z = 8$ )

A number of OH features are detected redward of  $\approx 2810$  Å in our UV spectrum of HD 222925. Our syntheses yield  $\log \varepsilon(O) \approx +7.9$  or so from these features when using the Kurucz (2011) OH line list. The [O/Fe] ratio, +0.67, is 0.25 dex higher than that found by Navarrete et al. (2015), [O/Fe] =  $+0.42 \pm 0.07$ , based on a careful NLTE differential analysis (relative to the Sun) of the O I triplet near 7770 Å. The UV OH transitions are known to overestimate the O abundance when derived using 1D LTE model atmospheres (e.g., Bessell et al. 2015). In the absence of a 3D hydrodynamical model atmosphere for HD 222925, we recommend the [O/Fe] ratio derived by Navarrete et al.

### A.6. Sodium ( $Na$ , $Z = 11$ ) and Magnesium ( $Mg$ , $Z = 12$ )

We identify no Na I, Mg I, or Mg II lines with reliable  $\log(gf)$  values that are unblended and sufficiently—but not too—strong in our spectrum of HD 222925. Our recommended abundances for Na and Mg are based on the optical lines studied by Roederer et al. (2018b), including NLTE corrections to the Na abundance based on Lind et al. (2011).

### A.7. Aluminum ( $Al$ , $Z = 13$ )

We detect 8 UV Al I lines that are reasonably unblended and have reliable  $\log(gf)$  values. These lines, which arise from the ground level, yield a consistent abundance,  $\log \varepsilon(Al) = 4.23 \pm 0.07$ . This abundance, however, is about 0.6 dex lower than the abundance derived from 3 high-excitation ( $> 3.1$  eV) Al I lines in the optical spectrum,  $\log \varepsilon(Al) = 4.79 \pm 0.22$ . We also detect an unblended Al II line at 2669.155 Å, as discussed in detail in Roederer & Lawler (2021).



This line has a reliable  $\log(gf)$  value (NIST grade A+). The abundance derived from this line,  $\log \varepsilon(\text{Al}) = 4.77 \pm 0.13$ , agrees with that from the high-excitation Al I lines. Our result affirms the calculations of [Mashonkina et al. \(2016\)](#), who found that inelastic collisions with H effectively coupled the highly excited levels of neutral Al with the ground state of the ion, which dominates the ionization balance. [Nordlander & Lind \(2017\)](#) found a similar result and confirmed the abundance behavior for several UV Al I lines in two metal-poor stars. Our recommended Al abundance in HD 222925 averages the abundances from the three high-excitation Al I lines and the one Al II line.

#### A.8. Silicon (*Si*, $Z = 14$ )

The abundances derived from Si I lines in our study and [Roederer et al. \(2018b\)](#) exhibit similar, though not identical, behavior to Al. Si has a much higher first ionization potential (FIP; 8.15 eV) than Al (5.99 eV), so a larger fraction of Si atoms are neutral in the atmosphere of HD 222925. Seventeen of the 18 Si I lines examined by [Roederer et al.](#) originate from highly excited levels ( $> 4.9$  eV). The exception, the Si I line at 4102 Å, originates from a moderately excited level at 1.91 eV. These lines yield  $\log \varepsilon(\text{Si}) = 6.38 \pm 0.07$ . In contrast, the 5 UV lines of Si I originate from levels with  $E_{\text{low}}$  ranging from 0.01 to 0.78 eV. These lines yield  $\log \varepsilon(\text{Si}) = 6.02 \pm 0.14$ , which is notably lower. A similar discrepancy was noticed in the metal-poor, red giant BD +44°493 ([Roederer et al. 2016b](#)).

We present 4 new detections of Si II lines in the MIKE optical spectrum of HD 222925. We also search for Si II lines in our STIS UV spectrum, but these lines are too blended or too weak to yield reliable abundances. The 4 optical Si II lines yield  $\log \varepsilon(\text{Si}) = 6.48 \pm 0.05$ , which is in agreement with the abundance derived from the high-excitation Si I lines.

[Mashonkina et al. \(2016\)](#) found that departures from LTE were minimal in the line-forming layers of a moderately metal-poor dwarf, although that study only considered the moderately or highly excited levels of neutral Si. We suspect that the low-lying levels of neutral Si may be overpopulated in our LTE calculations, so the UV Si I lines may yield low abundances, though not to the same degree as found in Al. New NLTE calculations for these levels would be welcome. Our recommended Si abundance in HD 222925 is based on only the optical Si II and high-excitation Si I lines.

#### A.9. Phosphorus (*P*, $Z = 15$ )

We detect several P I lines in HD 222925. Some of them are saturated, blended, and not useful as abundance indicators, but three P I lines yield reliable abundances. These lines arise from moderately excited levels ( $\approx 1.41$  eV). The derived  $[\text{P}/\text{Fe}]$  ratio ( $+0.18 \pm 0.15$ ) is in good agreement with other stars of similar metallicity ([Roederer et al. 2014b](#)). Our recommended P abundance is based on these UV lines.

#### A.10. Sulphur (*S*, $Z = 16$ )

We detect three lines of the S I multiplet 8 in our optical MIKE spectrum. Each of these three lines is comprised of three fine-structure components. Theoretical  $\log(gf)$  values are reasonably consistent for these fine-structure components: the standard deviations of the total  $\log(gf)$  value of each line from different sources are  $\approx 0.03$  dex ([Wiese et al. 1969](#); [Biemont et al. 1993](#); see [Caffau et al. 2005](#) and [Scott et al. 2015](#)). We conservatively adopt twice this value as the  $\log(gf)$  uncertainty. Table 1 lists the center-of-gravity wavelengths based on the [Kurucz \(2011\)](#) fine-structure components and the combined  $\log(gf)$  values from [Biemont et al.](#) We also apply a small  $-0.05$  dex NLTE abundance correction, following the calculations presented by [Korotin et al. \(2017\)](#). Our recommended S abundance is based on these three S I lines.

#### A.11. Potassium (*K*, $Z = 19$ )

No K I or K II lines are strong enough to detect in our UV spectrum of HD 222925. Our recommended K abundance is based on one optical K I line, including NLTE corrections from [Takeda et al. \(2002\)](#).

#### A.12. Calcium (*Ca*, $Z = 20$ )

We detect 2 lines of Ca II in the UV spectrum of HD 222925. We adopt the  $\log(gf)$  values for these lines from [Theodosiou \(1989\)](#) as recommended by [Den Hartog et al. \(2021b\)](#). That study also reassessed the  $\log(gf)$  values for optical Ca I lines, and we recalculate the Ca abundance derived from the 34 Ca I lines analyzed by [Roederer et al. \(2018b\)](#). The revised  $\log(gf)$  scale only changes the mean  $\log \varepsilon(\text{Ca})$  abundance by  $+0.02$  dex, but the standard deviation decreases substantially, from 0.15 to 0.09 dex. The abundances derived from the Ca I and Ca II lines are in good agreement, as shown in Figure 1. Our recommended Ca abundance is based on the weighted average of all 36 lines.

#### A.13. Other Fe-group Elements

Lines of neutral and ionized atoms are detected in our UV spectrum of HD 222925 for most of the Fe-group elements. These elements have relatively low FIPs, ranging from 6.56 eV (scandium, Sc,  $Z = 21$ ) to 7.90 eV (Fe; [Morton 2003](#)).

These atoms are primarily found in their ionized states in the atmosphere of HD 222925. Zinc (Zn,  $Z = 30$ ) is an exception; its FIP is much higher (9.39 eV), and substantial fractions of both neutral and ionized Zn are present.

We detect no UV lines of Sc I or Sc II with reliable  $\log(gf)$  values and HFS patterns, and our recommended Sc abundance is based on that derived from Sc II lines in the optical spectrum.

We detect and analyze several UV Ti I and Ti II lines. Our recommended titanium (Ti,  $Z = 22$ ) abundance is based on the abundances derived from the optical and UV Ti II lines. The abundances derived from these two ionization stages differ by  $0.28 \pm 0.06$  dex (optical lines) or  $0.12 \pm 0.08$  dex (UV lines), after Saha corrections are applied. These small differences are compatible with previous studies of Ti in other stars, although it is unclear why the difference derived from optical lines is larger than the difference derived from UV lines. NLTE calculations, like those presented in [Sitnova et al. \(2020\)](#), could help to reconcile the Saha discrepancy.

There are no strong and unblended V I lines with reliable  $\log(gf)$  values and HFS patterns in our spectrum, but we detect and analyze several V II lines. Our recommended vanadium (V,  $Z = 23$ ) abundance is based on the abundances derived from the optical and UV V II lines.

We detect and analyze 15 lines of Cr I and 20 lines of Cr II in the UV spectrum. Our recommended chromium (Cr,  $Z = 24$ ) abundance is based on the abundances derived from the optical and UV Cr II lines.

There are no Mn I lines in the UV spectrum that were covered by our preferred laboratory source, [Den Hartog et al. \(2011\)](#). We analyze two UV Mn II lines from [Den Hartog et al.](#), in addition to the three optical Mn II lines analyzed by [Roederer et al. \(2018b\)](#). Our recommended manganese (Mn,  $Z = 25$ ) abundance is based on the abundances derived from these five Mn II lines.

The cases of Fe (Section 3.4) and cobalt (Co,  $Z = 27$ ; Appendix A.14) are sufficiently complex to warrant separate discussions.

We detect and analyze multiple lines of Ni I and Ni II in our UV spectrum of HD 222925. Our recommended nickel (Ni,  $Z = 28$ ) abundance is derived from the UV Ni II lines.

Cu I and Cu II lines are detected in the UV spectrum. No HFS  $A$  constants are available for the Cu II lines, but these lines are reasonably weak and so the abundances derived from them are minimally affected by this shortcoming (see Section 3.1 of [Roederer & Lawler 2012](#)). Following [Korotin et al. \(2018\)](#) and [Roederer & Barklem \(2018\)](#), the recommended copper (Cu,  $Z = 29$ ) abundance is based on the abundances derived from the UV Cu II lines.

The Zn II resonance doublet at 2025 and 2062 Å is detected in our UV spectrum of HD 222925, but these lines are too blended to yield a reliable zinc (Zn,  $Z = 30$ ) abundance. Two Zn I lines are detected in the UV spectrum and useful for analysis. Our recommended Zn abundance is based on the abundances derived from the optical and UV Zn I lines, which have been found to yield consistent results with the Zn II lines when both species are considered ([Roederer & Barklem 2018](#)).

#### A.14. Cobalt (Co, $Z = 27$ )

A total of 11 Co I lines with  $\log(gf)$  values and HFS constants reported by [Lawler et al. \(2015\)](#) are detected and reasonably unblended. The mean abundance derived from these lines,  $\log \epsilon(\text{Co}) = 3.39 \pm 0.05$ , is in good agreement with the Co abundance derived from 21 optical Co I lines,  $\log \epsilon(\text{Co}) = 3.33 \pm 0.10$ . Seven Co II lines with  $\log(gf)$  values reported by [Lawler et al. \(2018\)](#) are detected and reasonably unblended. Table A1 presents the complete line component patterns for these lines, computed using the HFS  $A$  constants from [Ding & Pickering \(2020\)](#), or from [Lawler et al. \(2018\)](#) and [Ding & Pickering](#) averaged together, for levels in common. HFS constants are also presented in the Vienna Atomic Line Database (VALD; [Pakhomov et al. 2019](#)), and [Fu et al. \(2021\)](#) present new measurements that confirm the odd-parity HFS  $A$  constants we use. Table A1 includes two other Co II lines, at 2214.793 and 2314.975 Å, that are detected but too saturated to be useful as abundance indicators. The abundance derived from the seven UV Co II lines,  $\log \epsilon(\text{Co}) = 3.48 \pm 0.05$ , is in fair agreement with the abundance derived from Co I lines.

Previous work ([Cowan et al. 2020](#)) has noted the difficulty of interpreting abundances derived from Co I and II lines. In that study of three metal-poor ( $[\text{Fe}/\text{H}] \approx -3$ ) dwarf stars, the Co I lines yielded a higher abundance ( $\approx +0.4$  dex) than the Co II lines. That behavior is opposite what would be expected if NLTE overionization is responsible for the offset. In contrast, in HD 222925, the seven Co II lines exhibit the expected behavior, yielding a Co abundance higher by +0.11 dex than the Co I lines. NLTE calculations (see [Bergemann et al. 2010](#)) have not been performed for the UV lines examined here, and we encourage new calculations.

We suggest that the seven Co II lines with HFS are the best Co abundance indicators in HD 222925.

#### A.15. Gallium (Ga, $Z = 31$ )

Our spectrum covers the Ga II line at 2090.768 Å, which is illustrated in Figure 2. This line has not previously been examined in cool stars. Excess absorption with  $\approx 20\%$  continuum depth is detected at the correct wavelength in our spectrum of HD 222925.

**Table A1.** Hyperfine Structure Line Component Patterns for Co II Lines

Wavenumber (cm <sup>-1</sup> )	$\lambda_{\text{air}}$ (Å)	$F_{\text{upper}}$	$F_{\text{lower}}$	Component Position (cm <sup>-1</sup> )	Component Position (Å)	Strength
45709.627	2187.0388	5.5	4.5	0.259000	-0.012393	0.300000
45709.627	2187.0388	4.5	4.5	0.079700	-0.003814	0.097222
45709.627	2187.0388	4.5	3.5	0.040100	-0.001919	0.152778

NOTE—Energy levels from the NIST ASD and the index of air (Peck & Reeder 1972) are used to compute the center-of-gravity wavenumbers and air wavelengths,  $\lambda_{\text{air}}$ , and component positions are given relative to those values. Strengths are normalized to sum to 1 for each line. A complete machine-readable version of Table A1 is available online. A short version is shown here to illustrate its form and content.

This line connects the  $3d^{10}4s^2\ ^1S_0$  ground state to the  $4s4p\ ^3P_1^\circ$  excited state. There are three modern calculations of the upper-level radiative lifetime, which can be related to the transition probability through the branching fraction (BF) and level degeneracy. These results, from McElroy & Hibbert (2005), Liu et al. (2006), and Chen & Cheng (2010), agree to within  $\approx 11\%$ , and we average them together to yield  $\log(gf) = -3.25 \pm 0.05$  for this line. We directly adopt the HFS pattern and IS of the two stable Ga isotopes,  $^{69}\text{Ga}$  and  $^{71}\text{Ga}$ , from Karlsson & Litzén (2000). Ga has a low FIP, 6.00 eV, and  $\text{Ga}^+$  is the dominant ionization state in the atmospheres of cool stars. We adopt an  $r$ -process isotope mix from Sneden et al. (2008); this line yields the same abundance if we instead adopt a Solar isotope mix.

How likely is this identification to be correct? There are no other obvious species that might absorb at this wavelength in the Kurucz (2011) lists or NIST ASD. There are also no newly identified Fe I lines at this wavelength in the Peterson & Kurucz (2015) or Peterson et al. (2017) catalogs. Ideally, we would verify the identity of this line using other Ga II lines in the spectrum. Unfortunately, there are no other Ga II lines of comparable or greater strength that would be expected in our spectrum. This spin-forbidden line is the only Ga II line in the NIST ASD with  $\lambda > 1500\text{ Å}$  that is connected to the ground level of  $\text{Ga}^+$ .

As emphasized by Peterson (2021) in a similar context, there are dozens of predicted and potentially detectable unidentified Fe I (and Fe II) lines within several Å, whose energy levels, and thus wavelengths, are poorly known. We test this scenario by checking this region of the spectrum in several other archival STIS spectra. These spectra include the more metal-rich dwarf HD 76932 (Program = GO-9804, PI = Duncan;  $T_{\text{eff}}/\log g/[\text{Fe}/\text{H}]/v_t = 5680\text{ K}/4.11/-0.92/0.90\text{ km s}^{-1}$ , Roederer 2012), the similarly metal-poor dwarf HD 94028 (GO-8197 and GO-14161, Duncan and Peterson;  $6087\text{ K}/4.37/-1.65/1.10\text{ km s}^{-1}$ , Roederer et al. 2018c), the more metal-poor dwarf HD 84937 (GO-14161, Peterson;  $6418\text{ K}/4.16/-2.23/1.50\text{ km s}^{-1}$ , Roederer et al. 2018c), the more metal-poor subgiant HD 160617 (GO-8197, Duncan;  $5950\text{ K}/3.90/-1.77/1.3\text{ km s}^{-1}$ , Roederer & Lawler 2012), the more metal-poor subgiant HD 140283 (GO-7348, Edvardsson;  $5600\text{ K}/3.66/-2.62/1.15\text{ km s}^{-1}$ , Roederer 2012), and the more metal-poor giant HD 196944 (GO-14765, Roederer;  $5170\text{ K}/1.60/-2.41/1.55\text{ km s}^{-1}$ , Placco et al. 2015). Absorption at  $2090.768\text{ Å}$  is clearly detected in HD 76932, and a weak absorption line is tentatively detected in HD 196944.

We check whether a fictitious Fe I or Fe II line could consistently account for the absorption observed at this wavelength. We consider four cases: a low-excitation weak Fe I line ( $E_{\text{low}}/\log(gf) = 1.0\text{ eV}/-3.7$ ), a high-excitation strong Fe I line ( $5.0\text{ eV}/+0.1$ ), a low-excitation weak Fe II line ( $1.0\text{ eV}/-5.4$ ), and a high-excitation strong Fe II line ( $5.0\text{ eV}/-1.6$ ). We set the  $\log(gf)$  values of these fictitious lines to reproduce the absorption observed in HD 222925, and we use those atomic data to generate synthetic spectra for each of the six other stars. The Fe I lines and the high-excitation Fe II line fail to provide a satisfactory fit to all six stars. A low-excitation Fe II line—not unlike the Ga II line itself, when detectable—produces acceptable matches to the observed spectra.

We cautiously conclude that a Ga II line is the most likely explanation for absorption at  $2090.769\text{ Å}$ , but an as yet unidentified low-excitation ion from an Fe-group species cannot be excluded. Under this assumption, we also derive the Ga abundance in HD 76932 and HD 196944, finding  $\log \varepsilon(\text{Ga}) = 1.70 \pm 0.20$  and  $0.30 \pm 0.30$ , respectively, assuming an  $r$ -process isotope mix for HD 76932 and an  $s$ -process isotope mix for HD 196944. If the absorption is not a Ga II line, these values represent upper limits on the Ga abundance. We urge further study of this line in additional stars.

**Table A2.** Hyperfine Structure Line Component Patterns for the As I  $\lambda 2288$  Line

Wavenumber ( $\text{cm}^{-1}$ )	$\lambda_{\text{air}}$ ( $\text{\AA}$ )	$F_{\text{upper}}$	$F_{\text{lower}}$	Component Position ( $\text{cm}^{-1}$ )	Component Position ( $\text{\AA}$ )	Strength
43690.625	2288.1149	3.0	4.0	-0.045975	0.002408	0.375000
43690.625	2288.1149	3.0	3.0	0.050825	-0.002662	0.058333
43690.625	2288.1149	3.0	2.0	0.123425	-0.006464	0.004167

NOTE—The center-of-gravity wavenumber is from [Howard & Andrew \(1985\)](#). The index of air from [Peck & Reeder \(1972\)](#) is used to calculate the center-of-gravity air wavelength,  $\lambda_{\text{air}}$ . The line component positions are given relative to those values. The complete version of Table A2 is available in the online edition of the journal in machine-readable format. A short version is included here to demonstrate its form and content.

#### A.16. Germanium (*Ge*, $Z = 32$ )

We detect 5 Ge I lines in our spectrum, including the lines at 2691.341 and 3039.067  $\text{\AA}$  that have been used in many previous studies. These lines are illustrated in Figure 4. [Li et al. \(1999\)](#) provide experimental  $\log(gf)$  values, which are reliable to  $\approx 10\%$  (0.05 dex), for these lines.

Ge has a moderately high FIP, 7.90 eV, comparable to that of Fe, Co, Ni, and Cu. Most Ge is found as  $\text{Ge}^+$  in the atmosphere of HD 222925. Neutral Ge is a minority species, and it could be susceptible to NLTE overionization. No NLTE studies of Ge in late-type stars have been published. The ions of Fe, Co, Ni, and Cu yield abundances higher by  $\approx 0.15$  dex than the neutral species in HD 222925. We report the LTE abundance of Ge in Tables 1–3, but we caution that this abundance may underestimate the Ge abundance by a small amount. We strongly encourage a study of NLTE Ge line formation in cool stars.

#### A.17. Arsenic (*As*, $Z = 33$ )

We detect only one As I line, at 2288.115  $\text{\AA}$ . It is moderately blended with a Cd I line at 2288.020  $\text{\AA}$  and an Fe I line at 2288.045  $\text{\AA}$ , as illustrated in Figure 3. We adjust the  $\log(gf)$  value of the Fe I line to be  $-4.0$ , using other STIS spectra where absorption from the As I and Cd I lines is minimized. The As I and Cd I lines are sufficiently separated in wavelength that they are both resolved in our spectrum. The FIP of As is high, 9.79 eV, so NLTE overionization is unlikely to impact the LTE As abundance substantially.

There is one stable isotope of As,  $^{75}\text{As}$ . It has a nuclear spin of  $I = 3/2$ , which produces HFS. The lower- and upper-level HFS  $A$  constants are known for this line ([Bouazza et al. 1987](#)). We present the line component pattern for the As I line at 2288  $\text{\AA}$  in Table A2.

We adopt the theoretical transition probability computed by [Holmgren \(1975\)](#),  $\log(gf) = -0.06$ . This value is in good agreement with the  $\log(gf)$  value ( $-0.02$ ) computed using the theoretical upper-level radiative lifetime from [Holmgren](#) and an experimental BF,  $0.79 \pm 0.04$ , measured by [Berzins et al. \(2021\)](#) and published after our analysis had been completed. The  $\log(gf)$  uncertainty is dominated by the upper-level lifetime. The NIST ASD suggests a conservative D grade, and we adopt a  $\log(gf)$  uncertainty of 0.15 dex. Our recommended As abundance is based on this one line.

#### A.18. Selenium (*Se*, $Z = 34$ )

Only one Se I line, at 2074.784  $\text{\AA}$ , is both detected and unblended in our spectrum, as illustrated in Figure 2. We adopt the  $\log(gf)$  value from [Morton \(2000\)](#), with an uncertainty of 0.03 dex. The HFS and IS of this Se I line are expected to be small and negligible for our purposes, as discussed in [Roederer & Lawler \(2012\)](#). An additional Se I line at 2039.842  $\text{\AA}$  is detected, but it is too blended and the continuum placement too uncertain to yield a reliable abundance. The FIP of Se is high, 9.75 eV, so, as in the case of As, NLTE overionization is unlikely to impact the LTE Se abundance. Our recommended abundance is based on this one line.

#### A.19. Strontium (*Sr*, $Z = 38$ )

We check our spectrum for the 10 lines of Sr II that are listed in the NIST ASD. Some are strong enough to be detectable, but they are too blended with other features to be of use. Our recommended Sr abundance in HD 222925 is based on the optical Sr II lines from [Roederer et al. \(2018b\)](#).

A.20. *Yttrium* ( $Y$ ,  $Z = 39$ )

We detect and derive abundances from 4 Y II lines in our spectrum. One of them, at 2422.186 Å, is illustrated in Figure 3. Biémont et al. (2011) presented  $\log(gf)$  values for these lines. The weighted mean of these 4 Y II lines,  $\log \varepsilon(Y) = 1.06$ , is in excellent agreement with the weighted mean abundance derived from the 40 optical Y II lines studied by Roederer et al. (2018b),  $\log \varepsilon(Y) = 1.04$ . The FIP of Y is 6.22 eV, so most Y is found as  $Y^+$  in the atmosphere of HD 222925. NLTE overionization is not expected to be an issue. Our recommended Y abundance is based on the weighted average of these 44 Y II lines.

A.21. *Zirconium* ( $Zr$ ,  $Z = 40$ )

We check the 55 lines of Zr II listed in Ljung et al. (2006), and 22 of these lines yield abundances in our spectrum of HD 222925. Figure 4 illustrates two of these lines. The weighted mean of these 22 Zr II lines,  $\log \varepsilon(Zr) = 1.76$ , is in excellent agreement with the weighted mean abundance derived from the 51 optical Zr II lines studied by Roederer et al. (2018b),  $\log \varepsilon(Zr) = 1.74$ . The FIP of Zr is 6.63 eV, so  $Zr^+$  is the dominant species of Zr in the atmosphere of HD 222925. These Zr II lines likely form in LTE. Our recommended Zr abundance is based on the weighted average of these 73 Zr II lines.

A.22. *Niobium* ( $Nb$ ,  $Z = 41$ )

We check the 112 lines of Nb II listed in Nilsson & Ivarsson (2008) and Nilsson et al. (2010), and 9 of these lines are sufficiently strong and unblended to yield abundances. Figure 4 illustrates two of these lines. Nb has a low FIP, 6.76 eV, so  $Nb^+$  dominates in the atmosphere of HD 222925, and these Nb II lines likely form in LTE. Roederer et al. (2018b) derived an Nb abundance from a single optical Nb II line, and our recommended Nb abundance is based on the weighted average of these 10 Nb II lines.

A.23. *Molybdenum* ( $Mo$ ,  $Z = 42$ )

We check the 49 Mo II lines from the list of lines with experimental  $\log(gf)$  values from Sikström et al. (2001). Of these, 12 lines in our spectrum yield Mo abundances, and Figure 4 illustrates three of them. The weighted mean Mo abundance,  $\log \varepsilon(Mo) = 1.36$ , is in reasonable agreement with the Mo abundance derived by Roederer et al. (2018b) from 3 Mo I lines in the optical spectrum,  $\log \varepsilon(Mo) = 1.30$ . The FIP of Mo is 7.09 eV, so most Mo is found as  $Mo^+$  in the atmosphere of HD 222925. The agreement between these two values suggests that NLTE effects are minimal, as previously found for a few other stars (e.g., Peterson 2011; Roederer et al. 2014d). Our recommended Mo abundance is the weighted average of the abundances derived from 15 Mo I and Mo II lines.

A.24. *Ruthenium* ( $Ru$ ,  $Z = 44$ )

There are 12 Ru II lines from the study of Johansson et al. (1994) that are covered by our spectrum, and 2 of them are sufficiently strong and unblended to yield Ru abundances. One of these lines, at 2281.720 Å, is illustrated in Figure 3. These two lines yield  $\log \varepsilon(Ru) = 1.26$ , which is in fair agreement with the Ru abundance derived by Roederer et al. (2018b) from 5 optical Ru I lines,  $\log \varepsilon(Ru) = 1.34$ . Peterson (2011) found similarly good agreement in two stars. The FIP of Ru is 7.36 eV, and most Ru is  $Ru^+$  in the atmosphere of HD 222925. Any NLTE overionization of Ru appears to be minimal. Our recommended Ru abundance is the weighted average of the abundances derived from 7 Ru I and Ru II lines.

A.25. *Rhodium* ( $Rh$ ,  $Z = 45$ ), *Palladium* ( $Pd$ ,  $Z = 46$ ), and *Silver* ( $Ag$ ,  $Z = 47$ )

We check our UV spectrum for a handful of the potentially strongest lines of Rh II (Quinet et al. 2012; Bäckström et al. 2013), Pd I (Morton 2000), Ag I (Morton 2000), and Ag II (NIST ASD). All are too weak or blended to be useful as abundance indicators. Rh and Ag have low FIPs, 7.46 and 7.58 eV, respectively, while the FIP of Pd is higher, 8.34 eV. Rh and Ag are two of the few  $r$ -process elements whose abundances in HD 222925 are derived from their minority states. The abundances of Rh and Ag could be underestimated in LTE, but no NLTE calculations are available to confirm or refute this assertion. We advise using these abundances with caution until such calculations are available. Our recommended Rh, Pd, and Ag abundances are based on the 3 Rh I lines, 3 Pd I lines, and 1 Ag I line detected in the optical spectrum of HD 222925 by Roederer et al. (2018b).

A.26. *Cadmium* ( $Cd$ ,  $Z = 48$ )

We detect the Cd I line at 2288.020 Å, as shown in Figure 3. It is blended with the As I line at 2288.115 Å, as noted in Appendix A.17, and both lines are sufficiently resolved to yield independent abundance results. The Cd II line at 2144.394 Å, previously used by Roederer & Lawler (2012), is too blended in our spectrum to yield a reliable abundance.



There are 5 naturally occurring isotopes of Cd that are accessible to the  $r$ -process. Roederer et al. (2010) noted that the odd- $A$  Cd isotopes comprise a small fraction of all Cd isotopes, so their HFS can be neglected. The IS are expected to be small. We adopt the  $\log(gf)$  value for this line from Xu et al. (2004), and its uncertainty is  $\approx 0.05$  dex. Recent theoretical calculations of the radiative lifetime of the  $^1P_1$  upper level (Yamaguchi et al. 2019) and the oscillator strength (Shukla et al. 2022) are in agreement with the Xu et al. experimental value. The FIP of Cd is 8.99 eV, so a substantial fraction of neutral Cd is present in the atmosphere of HD 222925. No NLTE investigation of Cd line formation is available at present. Our recommended Cd abundance is based only on the single Cd I line.

The relatively low Cd abundance in HD 222925 (Section 4.3) warrants additional scrutiny. Neglecting to model an unidentified blending feature would cause us to overestimate the Cd abundance, not underestimate it. Similarly, neglecting to model multiple isotopes or HFS of  $^{111}\text{Cd}$  and  $^{113}\text{Cd}$ , which have only a small nuclear spin,  $I = 1/2$ , would also cause us to overestimate the abundance. Neutral Cd has a relatively simple spectrum, and its partition function is very low in the relevant temperature range ( $\approx 1.01$  at  $\log \tau \sim 0$  in this model atmosphere), so it is also unlikely that an incomplete partition function is at fault. The continuum is reasonably well identified in this spectral region (Figure 3), and the abundances derived from other features in this wavelength range appear normal (Figure 1). We find no reason to discount the abundance derived from the Cd I line at 2288.020 Å.

#### A.27. Indium ( $\text{In}$ , $Z = 49$ )

We detect absorption at the wavelength of the In II line at 2306.064 Å, as illustrated in Figure 3. This line has not previously been examined in cool stars. It connects the  $5s^2\ ^1S_0$  ground state to the  $5s5p\ ^3P_1$  excited state.

There are two stable isotopes of In,  $^{113}\text{In}$  and  $^{115}\text{In}$ .  $^{113}\text{In}$  only comprises 4.28% of In atoms in the solar system, and it is blocked by  $^{113}\text{Cd}$  from the  $r$ -process  $\beta$ -decay chains, so we assume that all In is  $^{115}\text{In}$  in HD 222925. These isotopes have a large nuclear spin,  $I = 9/2$ , and wide HFS, which is apparent in Figure 3. The IS ( $< 0.002$  Å; see below) is small compared to the wide-HFS components ( $\approx 0.12$  Å), so the  $^{113}\text{In}$  and  $^{115}\text{In}$  isotopes absorb at virtually the same wavelengths. The derived abundance is thus virtually insensitive to the isotope fraction. HFS  $A$  and  $B$  constants for the upper level of  $^{115}\text{In}$  measured by König et al. (2020) agree with the earlier experimental work by Larkins & Hannaford (1993) and Karlsson & Litzén (2001) and with the theoretical calculations by Jönsson & Andersson (2007). We adopt the König et al. values, which are effectively interchangeable with others for the purposes of stellar abundance analyses.

We adopt the IS from Wang et al. (2007). The sign convention now in use yields a positive IS when a heavier isotope is to the blue, but this convention was not always followed in older literature. The IS depends primarily on the upper and lower configurations of a transition. The mass shifts are small in the middle of the periodic table, and if either configuration includes an  $s$ -electron then the field shift of that configuration will often dominate the total IS. This results in the IS of both signs. In subsequent discussions of elements with more than one isotope, we resolve the sign ambiguity using a statement that the heavier or lighter isotopes are to the blue for transitions of interest. The lighter isotope is to the blue of the heavier isotope for the In II line at 2306 Å that connects to the ground  $5s^2$  configuration. This is clear from Figures 1 and 3 of Wang et al., and follows from first-order perturbation theory. We present the complete line component pattern in Table A3. The center-of-gravity wavenumber and air wavelength listed in Table A3 are given for a solar system isotopic mixture.

The NIST ASD recommends the semiempirical  $\log(gf)$  value from Curtis et al. (2000),  $-2.30$ , which is assigned a grade of B+, (7%, or 0.03 dex). In has a low FIP, 5.79 eV.  $\text{In}^+$  is the dominant ionization state in the atmosphere of HD 222925, so the line likely forms in LTE.

There are two other nearby blends that have a minimal impact on the In II line. A high-excitation ( $E_{\text{low}} = 6.09$  eV) Fe II line is detected at 2305.968 Å, and the NIST ASD grades the quality of its  $\log(gf)$  value as D+ ( $< 40\%$ ). We adjust the strength of this line within this allowed range to fit the observed line profile ( $\log(gf) = -1.06$ ). An Fe I line is detected at 2306.172 Å. The NIST ASD does not recommend a  $\log(gf)$  value for this line, so we adjust its strength to match the observed spectrum ( $\log(gf) = -2.4$ ).

How likely is it that this absorption is due to  $\text{In}^+$ ? Confirmation of this identification using other In II lines could be helpful, but no such lines are available. The only other In II transition with  $\lambda > 1600$  Å and  $E_{\text{low}} < 5$  eV, at 2364.686 Å, is too blended with a strong Fe II line at 2364.828 Å to be of any use in confirming the identification of the  $\lambda 2306$  line. The predicted strengths of two other lines in the Kurucz (2011) list with similar wavelengths, Ni II  $\lambda 2306.027$  Å and Mn II  $\lambda 2306.028$  Å, are each more than 2 dex weaker than what would be required to match the observed line in HD 222925, and their wavelengths are not as well matched to the line center as the In II line is. We conclude that there are no other lines in the NIST ASD or Kurucz (2011) line lists that can plausibly account for this absorption.

We follow the same procedure as described in Appendix A.15 to check whether this absorption could be accounted for by an unidentified line of an Fe-group element. This wavelength is only covered by E230H spectra of HD 84937, HD 94028, and HD 140283, so we supplement our search with the lower-resolution ( $R = 30,000$ ) STIS E230M spectrum



**Table A3.** Hyperfine Structure and Isotope Shift Line Component Pattern for the In II  $\lambda 2306$  Line

Wavenumber ( $\text{cm}^{-1}$ )	$\lambda_{\text{air}}$ ( $\text{\AA}$ )	$F_{\text{upper}}$	$F_{\text{lower}}$	Component Position ( $\text{cm}^{-1}$ )	Component Position ( $\text{\AA}$ )	Strength	Isotope
43350.582	2306.0645	5.5	4.5	1.060596	-0.056419	0.40000	113
43350.582	2306.0645	4.5	4.5	-0.199477	0.010611	0.33333	113
43350.582	2306.0645	3.5	4.5	-1.258196	0.066931	0.26667	113
43350.582	2306.0645	5.5	4.5	1.040281	-0.055338	0.40000	115
43350.582	2306.0645	4.5	4.5	-0.223472	0.011888	0.33333	115
43350.582	2306.0645	3.5	4.5	-1.284827	0.068347	0.26667	115

NOTE—Energy levels from the NIST ASD and the index of air (Peck & Reeder 1972) are used to compute the center-of-gravity wavenumbers and air wavelengths,  $\lambda_{\text{air}}$ , and component positions are given relative to those values. Strengths are normalized to sum to 1 for each isotope. Table A3 is available in the online edition of the journal in machine-readable format.

of HD 196944 (GO-12554, PI: Beers). None of these spectra show absorption at this wavelength. We consider 4 fictitious lines: a low-excitation weak Fe I line ( $E_{\text{low}}/\log(gf) = 1.0 \text{ eV}/-3.6$ ), a high-excitation strong Fe I line ( $5.0 \text{ eV}/+0.2$ ), a low-excitation weak Fe II line ( $1.0 \text{ eV}/-5.3$ ), and a high-excitation strong Fe II line ( $5.0 \text{ eV}/-1.5$ ). We set the  $\log(gf)$  values of these fictitious lines to reproduce the absorption observed in HD 222925, and we generate synthetic spectra for each of the four other stars. All of these fictitious lines overpredict the absorption in these four stars. This result boosts our confidence that the absorption detected at  $2306.064 \text{ \AA}$  is In II. Our recommended In abundance is based on this one In II line.

#### A.28. Tin (Sn, $Z = 50$ )

We identify absorption at the wavelength of an Sn II line at  $2151.514 \text{ \AA}$ . This line, illustrated in Figure 2, has not previously been examined in cool stars. It connects the  $5s^25p^2\ ^2P_{1/2}^o$  ground state to the  $5s5p^2\ ^4P_{1/2}$  excited state. The NIST ASD recommends  $\log(gf) = -2.53$ , with a grade of C+ (18%, 0.09 dex), based on the theoretical calculations of Oliver & Hibbert (2010). There are 10 naturally occurring or stable isotopes of Sn, and 6 of them are accessible to the  $r$ -process. We ignore any HFS or IS in our calculations. The IS are small for this region of the periodic table. The stable odd- $A$  Sn nuclei accessible to the  $r$ -process ( $^{117}\text{Sn}$  and  $^{119}\text{Sn}$ ) that might exhibit HFS comprise only  $\approx 25\%$  of the  $r$ -process abundance of Sn (Sneden et al. 2008), and they have only a small nuclear spin,  $I = 1/2$ . Sn has a relatively low FIP, 7.34 eV, and most Sn is singly ionized in the atmosphere of HD 222925. We derive  $\log \varepsilon(\text{Sn}) = 1.39 \pm 0.15$ .

How likely is it that this absorption is due to Sn II? We perform the same test as described in Appendix A.15, using 4 stars with spectra covering this wavelength: HD 76932, HD 84937, HD 140283, and HD 196944. We again consider 4 cases of fictitious lines: a low-excitation weak Fe I line ( $E_{\text{low}}/\log(gf) = 1.0 \text{ eV}/-3.5$ ), a high-excitation strong Fe I line ( $5.0 \text{ eV}/+0.3$ ), a low-excitation weak Fe II line ( $1.0 \text{ eV}/-5.2$ ), and a high-excitation strong Fe II line ( $5.0 \text{ eV}/-1.4$ ). In addition, there is one other plausible identification for this absorption given in the NIST ASD or Kurucz (2011) lists, an Fe II line at  $2151.508 \text{ \AA}$ . We perform the same test for this known line, which has  $E_{\text{low}} = 7.48 \text{ eV}$ . We derive  $\log(gf) = +0.8$  for this line by assuming that it alone accounts for the absorption at this wavelength and fitting its strength to the observed line profile in HD 222925. Our test excludes all possibilities except the fictitious low-excitation Fe II line.

There are three other Sn II lines that could potentially be strong enough to be detected in our spectrum ( $\lambda\lambda 2150.845$ ,  $2266.016$ , and  $2368.226 \text{ \AA}$ ). Unfortunately, all are too blended with stronger features. Peterson et al. (2020) detected a stronger Sn II line at  $\lambda_{\text{vacuum}} = 1899.898 \text{ \AA}$  in the spectra of several other stars, but that study did not examine the line at  $2151.514 \text{ \AA}$ . One star in the comparison sample, HD 94028, covers both lines. Oliver & Hibbert (2010) also calculated the transition probability for the Sn II line at  $1899 \text{ \AA}$ , and the NIST ASD recommends  $\log(gf) = -0.22$ , with a B+ grade (7% uncertainty, 0.03 dex). We synthesize both lines in HD 94028. The Sn II line at  $1899 \text{ \AA}$  is easily detectable and yields  $\log \varepsilon(\text{Sn}) = 0.9 \pm 0.2$ , which is reasonable (Roederer et al. 2016a). The Sn II line at  $2151 \text{ \AA}$  is much weaker and not detected. The upper limit we infer from this line,  $\log \varepsilon(\text{Sn}) < 1.2$ , is compatible with the abundance derived from the  $\lambda 1899$  line.

**Table A4.** Hyperfine Structure and Isotope Shift Line Component Patterns for Sb I Lines

Wavenumber ( $\text{cm}^{-1}$ )	$\lambda_{\text{air}}$ ( $\text{\AA}$ )	$F_{\text{upper}}$	$F_{\text{lower}}$	Component Position ( $\text{cm}^{-1}$ )	Component Position ( $\text{\AA}$ )	Strength	Isotope
48332.424	2068.3440	5.0	4.0	0.399814	-0.017112	0.30555	121
48332.424	2068.3440	4.0	4.0	0.102274	-0.004377	0.06250	121
48332.424	2068.3440	4.0	3.0	0.062277	-0.002665	0.18750	121

NOTE—Energy levels from the NIST ASD and the index of air (Peck & Reeder 1972) are used to compute the center-of-gravity wavenumbers and air wavelengths,  $\lambda_{\text{air}}$ , and component positions are given relative to those values. Strengths are normalized to sum to 1 for each isotope. The complete version of Table A4 is available in the online edition of the journal in machine-readable format. A short version is included here to demonstrate its form and content.

We also check several lines of the neutral, minority species that are covered by our spectrum. No Sn I lines are detected, and we derive upper limits from three lines that are not blended with other strong features. The most constraining upper limit is derived from the Sn I line at 2199.346  $\text{\AA}$ . This value,  $\log \varepsilon(\text{Sn}) < 1.5$ , is compatible with the abundance derived from the Sn II line at 2151  $\text{\AA}$ .

We conclude that an Sn II line is the most likely explanation for absorption at 2151.514  $\text{\AA}$ , given current data. We caution, however, that an unidentified low-excitation ion from an Fe-group element could mimic the behavior observed in the spectra available to us, so we urge further study of this line in additional stars.

#### A.29. Antimony (Sb, $Z = 51$ )

We detect absorption at the wavelengths of two Sb I lines, at 2068.344 and 2175.818  $\text{\AA}$ . The  $\lambda 2175$  line is illustrated in Figure 2. We adopt the atomic transition probabilities from Hartman et al. (2010), which are reliable to  $\approx 5\%$ . Both lines are dominant branches ( $\approx 90\%$ ) from the upper levels. The FIP of Sb is 8.61 eV. Most Sb is ionized in the atmosphere of HD 222925, but a substantial reservoir of neutral Sb is likely to be present.

There are two stable isotopes of Sb,  $^{121}\text{Sb}$  and  $^{123}\text{Sb}$ . These isotopes have nonzero nuclear spin  $I = 5/2$  and  $I = 7/2$ , respectively. We adopt the ground-level HFS  $A$  and  $B$  values reported by Fernando et al. (1960), which are based on atomic beam magnetic resonance measurements, and are of high accuracy and precision. Two studies (Buchholz et al. 1978; Hassini et al. 1988) reported excited-level HFS constants of  $^{121}\text{Sb}$  for the resonance lines of interest, and their results are in near agreement. Sobolewski et al. (2016a,b) also reported HFS  $A$  constants of  $^{123}\text{Sb}$  and a  $B$  constant for one ( $\lambda 2175$ ) of the two lines. We scale the HFS  $B$  values for  $^{121}\text{Sb}$  found by Hassini et al. to generate HFS  $B$  values for both  $^{123}\text{Sb}$  lines. Our scaled  $B$  value for the upper level of the  $^{123}\text{Sb}$   $\lambda 2175$  line matches the Sobolewski et al. (2016b) experimental value. Our choice of HFS  $B$  constants has a negligible impact on the derived abundances.

The IS of 287 MHz for the 2175  $\text{\AA}$  line was computed by Gamrath et al. (2018b) using a sophisticated multiconfiguration Dirac-Hartree-Fock code. The two Sb I lines at 2068 and 2175  $\text{\AA}$  in Table A4 both connect a common upper  $5p^2(^3P)6s$  configuration and common lower  $5p^3$  ground configuration. Table 4 of Gamrath et al. shows that the field shift from the participation of an  $s$  electron in the upper or lower configuration dominates the normal and specific mass shifts for heavy elements, such as Sb. The heavier isotope is to the blue if the  $s$  electron is in the upper, but not lower, configuration. Sb has a positive IS using the standard sign convention. Although their mixing percentages are slightly different, we adopt the same IS value (287 MHz) for both lines. We present the line component patterns for the Sb I lines at 2068 and 2175  $\text{\AA}$  in Table A4. The center-of-gravity wavenumber and air wavelength in Table A4 are given for a solar system isotopic mixture.

The  $\lambda 2068.344$  line is found in the blue wing of a stronger Cr II line at 2068.395  $\text{\AA}$ , and it is nearly coincident with an Fe II line at 2068.320  $\text{\AA}$ . This Sb I line is too blended to be used as an abundance indicator in HD 222925. We derive an upper limit on the Sb abundance by assuming all of the absorption is due to Sb I and Cr II,  $\log \varepsilon(\text{Sb}) < 0.8$ .

The  $\lambda 2175.818$  line is less blended and clearly detected, with a depth  $\approx 35\%$  of the continuum, as illustrated in Figure 2. There are no obvious blends at this wavelength, and a nearby Fe II ( $\lambda 2175.725$ ) line can easily be fit in our syntheses with minimal impact on the derived Sb abundance. An unidentified absorption line at 2175.907  $\text{\AA}$  is present. We model it as an Fe I line with  $E_{\text{low}} = 1.0$  eV and  $\log(gf) = -2.95$ , and it, too, has minimal impact on the derived Sb abundance. We derive  $\log \varepsilon(\text{Sb}) = 0.37 \pm 0.20$  from this line, which is compatible with the upper limit derived from the  $\lambda 2068$  line. Our recommended Sb abundance is based on the Sb I line at 2175.818  $\text{\AA}$ .

A.30. *Tellurium (Te,  $Z = 52$ )*

We detect two Te II lines in our spectrum, at 2259.034 and 2385.792 Å. Other Te I lines, at 2142.822 and 2383.277 Å, are too blended to be of use as abundance indicators in HD 222925. Roederer et al. (2012b) discussed the  $\lambda 2385$  line in detail, and we adopt the  $\log(gf)$  for this line from that study. The uncertainty in its  $\log(gf)$  value is  $\approx 16\%$  (0.08 dex). This line is in a region where the continuum is depressed  $\approx 25\%$  by strong Fe II lines at 2382.039 and 2388.629 Å. We account for these lines in our syntheses.

The Te I line at 2259.034 Å has not previously been studied in cool stars, and it is illustrated in Figure 3. It connects the  $5p^4\ ^3P_2$  ground level to the  $5p^3(^4S^o)6s\ ^5S_2^o$  excited level. This line is virtually unblended and unsaturated in HD 222925, so it is an ideal abundance indicator. Morton (2000) quotes a  $\log(gf)$  value for this line,  $-1.31$ , using an upper-level radiative lifetime measurement (accurate to 3%) from Garpman et al. (1971) and branching ratios from Ubelis & Berzinsh (1983). This line is a major ( $\approx 92\%$ ) branch. The  $\log(gf)$  value should be reliable to within a few hundredths of a dex.

The Te I line at 2002.028 Å is covered by our spectrum. We calculate a  $\log(gf)$  value of  $-1.60 \pm 0.17$  from the experimental transition probability obtained by Ubelis & Berzinsh (1991). This line is probably detected, but the S/N in our spectrum is too low to be useful. Furthermore, analysis of this line in other stars with STIS spectra yields Te abundances considerably higher than those from other Te I lines, suggesting the presence of an unidentified blend at this wavelength. We discard this line from further consideration.

Four stable Te isotopes are accessible to the  $r$ -process,  $^{125}\text{Te}$ ,  $^{126}\text{Te}$ ,  $^{128}\text{Te}$ , and  $^{130}\text{Te}$ . Only  $^{125}\text{Te}$  has a nonzero nuclear spin  $I = 1/2$ , which is small. This isotope comprises only  $\approx 7\%$  of the  $r$ -process Te isotope mix (Sneden et al. 2008), so we ignore the HFS from this isotope. We also ignore the small IS of these Te isotopes. The FIP of Te is high, 9.01 eV, so a substantial fraction of neutral Te is present in the atmosphere of HD 222925. We derive  $\log \varepsilon(\text{Te}) = 1.76 \pm 0.25$  from the Te I  $\lambda 2385$  line and  $\log \varepsilon(\text{Te}) = 1.61 \pm 0.10$  from the Te I  $\lambda 2259$  line. Our recommended Te abundance is based on a weighted average of these two values.

A.31. *Lanthanide Elements*

Some of the lanthanide elements, including gadolinium (Gd,  $Z = 64$ ), terbium (Tb,  $Z = 65$ ), dysprosium (Dy,  $Z = 66$ ), erbium (Er,  $Z = 68$ ), thulium (Tm,  $Z = 69$ ), and ytterbium (Yb,  $Z = 70$ ) are detectable in our spectrum of HD 222925. Roederer et al. (2018b) derived abundances of these elements from the optical spectrum, often using many more lines. We derive abundances from 6 lines of Gd II in the UV spectrum (compared with 38 lines in the optical spectrum), 1 line of Tb II (3 lines), 1 line of Dy II (32 lines), 3 lines of Er II (13 lines), 3 lines of Tm II (7 lines), and 1 line of Yb II (1 line). We use the same sources of  $\log(gf)$  values, from the Wisconsin group’s work, so our results are on a consistent scale with previous abundance derivations. The uncertainties in these  $\log(gf)$  values are generally better than 5% (0.02 dex). The abundances derived from UV lines and optical lines are in excellent agreement. Our recommended abundances for these elements are based on the weighted averages of these values. Our recommendations for all other lanthanide elements, plus Ba, except Lu (Appendix A.32), are adopted from Roederer et al.

The Ho abundance is slightly low relative to the other lanthanide elements in HD 222925 (see Section 4.3), so it deserves special mention. We reexamine all nine lines that were used by Roederer et al. (2018b) to derive the Ho abundance, recheck the atomic data used to generate our syntheses, and confirm that our synthesis parameter files are correct. We find no fault with the original analysis. We also assess how much the original line fits could be adjusted to maximize the abundance; for example, by making different choices about the strengths of blending features, while continuing to adequately reproduce the observed spectrum. This approach could only increase the Ho abundance by  $\approx 0.04$  dex, which is insufficient to explain the discrepancy. The MOOG partition function for Ho II agrees with the NIST ASD value to within  $\approx 5\%$  at  $\log \tau \sim 0$ . Using the NIST partition functions would lead to a small decrease in the Ho abundance,  $\approx 0.03$  dex or less, exacerbating the discrepancy. We find no reason to discount the Ho abundance presented previously.

A.32. *Lutetium (Lu,  $Z = 71$ )*

We check for 22 UV lines of Lu II, and 7 of them are sufficiently strong and unblended to yield reliable abundances. Figure 4 illustrates the Lu II line at 2911.392 Å. We adopt  $\log(gf)$  values for these lines from Quinet et al. (1999), Lawler et al. (2009), and Roederer et al. (2010). There are two stable isotopes of Lu,  $^{175}\text{Lu}$  and  $^{176}\text{Lu}$ , and only the majority isotope  $^{175}\text{Lu}$  (97.4% in the solar system) is accessible to the  $r$ -process. It has nuclear spin  $I = 7/2$ , which produces wide HFS patterns, as is apparent in Figure 4. We adopt the HFS patterns recently published by Den Hartog et al. (2020). Roederer et al. (2018b) derived the Lu abundance in HD 222925 from two optical lines. That study accounted for HFS and used a consistent set of  $\log(gf)$  values. Lu has a low FIP, 5.43 eV, so virtually all Lu atoms are ionized in the atmosphere of HD 222925. Our recommended Lu abundance reflects the weighted mean of the 7 UV lines and 2 optical lines.

A.33. *Hafnium* (Hf,  $Z = 72$ )

We check for 28 UV lines of Hf II, and 15 of them yield reliable abundances. Figure 4 illustrates the Hf II line at 2647.297 Å. We adopt  $\log(gf)$  values from Lawler et al. (2007) and Den Hartog et al. (2021a). Four stable Hf isotopes are accessible to the  $r$ -process,  $^{177}\text{Hf}$ ,  $^{178}\text{Hf}$ ,  $^{179}\text{Hf}$ , and  $^{180}\text{Hf}$ , and the  $^{177}\text{Hf}$  and  $^{179}\text{Hf}$  isotopes have large nonzero nuclear spins  $I = 7/2$  and  $9/2$ , respectively. The HFS and IS of the Hf II lines of interest have not been studied in the laboratory. We observe no substantial broadening of the Hf II lines in our spectrum, and most of the Hf II lines are on the weak part of the curve of growth. Hf has a low FIP, 6.83 eV, and singly ionized Hf is the dominant species in the atmosphere of HD 222925. Our recommended Hf abundance is based on a weighted average of the 15 UV lines and 5 optical lines studied by Roederer et al. (2018b).

A.34. *Tantalum* (Ta,  $Z = 73$ )

We have checked 20 potential Ta II lines in our spectrum of HD 222925, but we do not detect any of them. Ta has a low FIP, 7.55 eV, so  $\text{Ta}^+$  is the dominant species in the atmosphere of HD 222925.

Siqueira Mello et al. (2013) reported detections of two Ta II lines, at 2635.583 and 2832.702 Å, in a STIS E230M ( $R = 30,000$ ) spectrum of the metal-poor,  $r$ -process-enhanced red giant CS 31082-001. Absorption is detected at the  $\lambda 2635$  line in our spectrum of HD 222925, but we cannot confidently attribute this absorption to Ta II. Lines of Mn I ( $\lambda 2635.561$ ) and OH ( $\lambda 2635.581$ ) are potential absorbers. We calculate  $\log(gf) = -0.16 \pm 0.03$  for this Ta II line from the transition probability published by Quinet et al. (2009). This value is 0.86 dex lower than the  $\log(gf)$  value adopted by Siqueira Mello et al. from VALD, and it predicts a substantially weaker line. No absorption is detected at the  $\lambda 2832$  line in HD 222925, despite the continuum being clear in this region. Quinet et al. did not cover the  $\lambda 2832$  line in their study, and we are reluctant to derive an upper limit from this line using the VALD  $\log(gf)$  value. Our upper limit is instead derived from the Ta II line at 2752.486 Å.

A.35. *Tungsten* (W,  $Z = 74$ )

We check our spectrum for the 40 W II lines studied by Kling et al. (2000) and Nilsson et al. (2008). Six of these lines yield acceptable abundances in HD 222925, and Figure 2 illustrates two of them. The FIP of W is 7.86 eV, so most W atoms are singly ionized in the atmosphere of HD 222925.

W has five stable isotopes, four of which are produced by the  $r$ -process:  $^{182}\text{W}$ ,  $^{183}\text{W}$ ,  $^{184}\text{W}$ , and  $^{186}\text{W}$ . Only  $^{183}\text{W}$  has nonzero nuclear spin  $I = 1/2$ . No information on the HFS of this isotope is available. The IS of W II lines have been studied by Aufmuth et al. (1995), but none of the W II lines in our spectrum have measured IS. Furthermore the assignment configurations and terms of levels in  $\text{W}^+$  are also incomplete. Low-lying even-parity levels are typically a mixture of  $5d^5$ ,  $5d^46s$ , and  $5d^36s^2$  configurations. As noted previously, transitions involving an  $s$ -electron produce large field shifts. The odd-parity levels studied by Aufmuth et al. are primarily mixtures of the  $5d^46p$  and  $5d^36s6p$  configurations. The upper levels of the relatively strong spectral lines in our study are also likely to include significant contributions from these configurations. Aufmuth et al. found negative field shifts as large as  $-0.155 \text{ cm}^{-1}$  for pure  $5d^36s^2$  to  $5d^46p$  transitions of  $^{186}\text{W}$  compared to  $^{184}\text{W}$ . Aufmuth et al. used the standard sign convention, and we use their results to estimate the IS for the W II lines. We present the line component patterns for eight lines of W II, including several lines that may be useful abundance indicators in other stars, in Table A5. These eight W II lines all connect to the ground  $5d^4(^6S)6s$  configuration, and have lighter isotopes to the blue of the heavier isotope.

Among the six W II lines we use to derive an abundance, the IS are estimated for four of them ( $\lambda\lambda 2088.204$ ,  $2094.751$ ,  $2118.875$ , and  $2194.528$ ). We do not include the IS in our syntheses of the W II lines at  $2204.489$  and  $2658.032$  Å. We assess the abundance sensitivity to the IS by deliberately excluding it from the test syntheses of the lines for which an IS is estimated. The inferred abundances change by  $< 0.01$  dex, so the impact of the unknown IS for the other two weak lines is likely minimal. We adopt an  $r$ -process isotope mix in these syntheses.

These six transitions are all major decay branches from upper levels, whose radiative lifetimes have been measured to better than  $\approx 10\%$ . The Kling et al. (2000) and Nilsson et al. (2008)  $\log(gf)$  values agree to within 0.03 dex for the one line of these six in common ( $\lambda 2118$ ). The W II line at  $2204.489$  Å was not included in either study. Roederer et al. (in preparation) estimated a  $\log(gf)$  value for this line using a reverse abundance analysis based on five other W II lines in the STIS E230H ( $R = 114,000$ ) spectrum of HD 196944. We consider this  $\log(gf)$  value to be of lower quality than the other ones, but it is likely reliable at the  $\sim 0.10$ – $0.15$  dex level. Our recommended W abundance in HD 222925 is based on a weighted average of these six W II lines.

A.36. *Rhenium* (Re,  $Z = 75$ )

We detect two Re II resonance lines in our spectrum, at  $2214.277$  and  $2275.255$  Å, as illustrated in Figures 2 and 3. The FIP of Re is 7.83 eV, and  $\text{Re}^+$  is the dominant ionization state in the atmosphere of HD 222925.

There are two stable isotopes of Re,  $^{185}\text{Re}$  and  $^{187}\text{Re}$ , and both are accessible to the  $r$ -process. Their nuclear spins are  $I = 5/2$ , so they both exhibit HFS. We adopt the ground-level HFS  $A$  and  $B$  values reported by Wahlgren et al.

**Table A5.** Estimated Isotope Shift Line Component Patterns for W II Lines

Wavenumber ( $\text{cm}^{-1}$ )	$\lambda_{\text{air}}$ ( $\text{\AA}$ )	Component Position ( $\text{cm}^{-1}$ )	Component Position ( $\text{\AA}$ )	Isotope
49245.361	2029.9948	0.301529	−0.012431	180
49245.361	2029.9948	0.146529	−0.006041	182
49245.361	2029.9948	0.069029	−0.002846	183

NOTE—Energy levels from the NIST ASD and the index of air (Peck & Reeder 1972) are used to compute the center-of-gravity wavenumbers and air wavelengths,  $\lambda_{\text{air}}$ , and component positions are given relative to those values. The complete version of Table A5 is available in the online edition of the journal in machine-readable format. A short version is included here to demonstrate its form and content.

**Table A6.** Hyperfine Structure and Isotope Shift Line Component Patterns for Re II Lines

Wavenumber ( $\text{cm}^{-1}$ )	$\lambda_{\text{air}}$ ( $\text{\AA}$ )	$F_{\text{upper}}$	$F_{\text{lower}}$	Component Position ( $\text{cm}^{-1}$ )	Component Position ( $\text{\AA}$ )	Strength	Isotope
45147.402	2214.2770	5.5	5.5	−1.195604	0.058646	0.25325	185
45147.402	2214.2770	5.5	4.5	−0.405968	0.019913	0.03247	185
45147.402	2214.2770	4.5	5.5	−1.017998	0.049934	0.03247	185

NOTE—Center-of-gravity wavenumbers and air wavelengths,  $\lambda_{\text{air}}$ , are given with component positions relative to those values. Strengths are normalized to sum to 1 for each isotope. The complete version of Table A6 is available in the online edition of the journal in machine-readable format. A short version is included here to demonstrate its form and content.

(1997), based on their measurements using a Fourier Transform Spectrometer (FTS). The IS of 118.6 mK for the Re II line at 2214  $\text{\AA}$  and 117.8 mK for the Re II line at 2275  $\text{\AA}$  were also extracted from the FTS data by Wahlgren et al. Their Figure 1 shows that the lighter and rarer isotope is to the blue, and these two lines have negative IS, using the standard convention. The two Re II lines in Table A6 both connect to the ground  $5d^5(^6S)6s$  configuration. The common upper configuration and common lower configuration of the two Re lines yield very similar measured IS, as expected. We present the line component patterns for these two Re II lines in Table A6.

We adopt the  $\log(gf)$  value for the Re II line at 2214  $\text{\AA}$ ,  $-0.019$ , from Palmeri et al. (2005). Measurements by Ortiz et al. (2013) support this value. The atomic transition probability for the Re II line at 2275  $\text{\AA}$  was determined by both Wahlgren et al. (1997) and Palmeri et al. The radiative lifetime measurements of the upper  $^7P_2$  level are in excellent agreement,  $4.47 \pm 0.22$  ns and  $4.5 \pm 0.3$  ns, respectively. Both studies report a dominant BF for the Re II line at 2275  $\text{\AA}$ . Unfortunately, the experimental BF of  $0.6 \pm 0.04$  from Wahlgren et al. does not agree with the theoretical BF of 0.928 from Palmeri et al. We adopt a simple average of 0.76, resulting in a  $\log(gf)$  value of  $-0.180$ . The  $\log(gf)$  values for the Re II lines at 2214 and 2275  $\text{\AA}$  are likely reliable to  $\approx 7\%$  (0.03 dex) and  $\approx 20\%$  (0.10 dex), respectively.

Both lines are strong and are the dominant absorbers at their respective wavelengths in our spectrum, as shown in Figures 2 and 3. Other blending features are present nearby. The known lines cannot reproduce the observed line profile in either case, without the presence of strong Re II lines broadened by HFS. We adopt an  $r$ -process isotope mix. The abundances derived from the  $\lambda 2214$  and  $\lambda 2275$  lines,  $\log \varepsilon(\text{Re}) = 0.10 \pm 0.15$  and  $0.25 \pm 0.15$ , respectively, are in good agreement. Our recommended Re abundance is based on a weighted average of these two lines.



A.37. *Osmium* (*Os*,  $Z = 76$ )

We check for 12 lines of Os I and 22 lines of Os II in our spectrum, and we derive abundances from 4 Os I lines and 5 Os II lines. Figure 3 illustrates two Os II lines, and Figure 4 illustrates one Os I line. The FIP of Os is 8.44 eV, and both neutral and singly ionized Os are present in HD 222925.

There are four stable isotopes of Os that are accessible to the  $r$ -process,  $^{188}\text{Os}$ ,  $^{189}\text{Os}$ ,  $^{190}\text{Os}$ , and  $^{192}\text{Os}$ . Only  $^{189}\text{Os}$  has a nonzero nuclear spin  $I = 3/2$ , and it only comprises  $\approx 17\%$  of the predicted  $r$ -process isotope mixture (Snedden et al. 2008). Little is known about the HFS or IS for the Os I and II lines. We assess the importance of HFS and IS as follows. We mount an Os hollow cathode lamp in front of 25  $\mu\text{m}$  and 10  $\mu\text{m}$  pinhole entrance slits to the 3 m focal length laboratory echelle spectrometer at the University of Wisconsin (Wood & Lawler 2012). This setup produces a resolving power of  $R > 250,000$ . The lines are not resolved, but broadening or hints of structure are apparent for the Os II lines at 2067, 2227, and 2282 Å. This preliminary result suggests that some HFS or IS may be present at a level that may impact stellar abundance work. Further investigation of this issue will be presented elsewhere. We do not include any HFS or IS in our syntheses of Os I or II lines, which could, in principle, cause us to overestimate the abundances derived from lines where HFS and IS are important.

We adopt  $\log(gf)$  values for both Os I and Os II lines from Quinet et al. (2006). Ivarsson et al. (2004) also published  $\log(gf)$  values for several Os II lines, but these two sets of values agree only moderately well for the 3 Os II lines in common, which are also used to derive abundances. This disagreement is mainly attributable to the different BF values, which were calculated from theory (Quinet et al.) or measured experimentally and corrected by calculations of residual branches that fall outside the wavelength range observed (Ivarsson et al.). The mean difference in their  $\log(gf)$  values is +0.05 dex, with the Ivarsson et al. values being larger, but the differences range from  $-0.09$  to  $+0.14$  dex, with a standard deviation of 0.10 dex. Formally, the  $\log(gf)$  errors are stated to be  $\approx 6\text{--}10\%$  ( $\approx 0.03\text{--}0.05$  dex), but we adopt a conservative uncertainty of 0.10 dex on these  $\log(gf)$  values.

The Os II line at 2067.230 Å appears to be blended with an unidentified species. This line is broader than would be expected from Os II alone, and it is shifted to the blue by  $\approx 0.01$  Å relative to the expected center of the Os II line. If we assume that Os II is the only line absorber at this wavelength, it yields an abundance  $\approx 0.6$  dex higher than the mean of the other Os I and Os II lines. We treat this value as an upper limit on the Os abundance. We do not recommend using this line as an abundance indicator without further study of the blending feature.

The mean abundance derived from 4 Os I lines,  $\log \varepsilon(\text{Os}) = 1.19 \pm 0.14$ , agrees with that derived from 5 Os II lines,  $\log \varepsilon(\text{Os}) = 1.09 \pm 0.12$ . These results agree with the Os abundance derived by Roederer et al. (2018b) from two weak optical Os I lines,  $\log \varepsilon(\text{Os}) = 1.26 \pm 0.15$ . We note that the UV lines yielding the highest abundances are not uniformly the ones where hints of broadening are detected in the laboratory echelle data. This result suggests that the abundance uncertainties are dominated by factors other than the neglect of HFS and IS in our syntheses, likely unidentified minor blends and continuum placement. Our recommended Os abundance is based on a weighted average of these 11 lines.

A.38. *Iridium* (*Ir*,  $Z = 77$ )

We check for 53 lines of Ir I and II in our spectrum. Four Ir I and two Ir II lines are detected and useful as abundance indicators, and two of these lines are illustrated in Figures 3 and 4. Several other lines are detected, but they are too blended to be useful. The FIP of Ir is high, 8.97 eV, and both neutral and singly ionized Ir are present.

There are two stable isotopes of Ir,  $^{191}\text{Ir}$  and  $^{193}\text{Ir}$ . Both are accessible to the  $r$ -process and have nuclear spin  $I = 3/2$ . The HFS and IS have been measured by Büttgenbach et al. (1978), Bürger et al. (1984), and Gianfrani & Tino (1993) for one of the Ir I lines that is useful for abundance work,  $\lambda 2924.790$ . This line connects an upper  $5d^7 6s(^5F)6p$  configuration to the ground  $5d^7 6s^2$  configuration. The lighter and rarer isotope is to the blue of the heavier isotope, which is a negative IS, as shown in Figure 2 of Gianfrani & Tino. We present the complete line component pattern for this line in Table A7. This line provides the best fit to the HD 222925 spectrum when its wavelength is shifted by 0.013 Å toward the blue.

The  $\log(gf)$  values for the Ir I lines are adopted from the NIST ASD, which combined upper-level radiative lifetime measurements from Gough et al. (1983) with BFs from Xu et al. (2007). With the exception of the Ir I  $\lambda 2481$  line, whose  $\log(gf)$  uncertainty is graded by NIST as having D accuracy ( $< 50\%$ , 0.30 dex), the other  $\log(gf)$  values are reliable to better than 7% (0.03 dex). The  $\log(gf)$  values for the Ir II lines are adopted from Ivarsson et al. (2004), who estimated uncertainties of  $\approx 7\%$  (0.03 dex).

Roederer et al. (2018b) derived the Ir abundance from a single optical Ir I line. We noticed an error in the treatment of the Ir isotope mix in our synthesis of this line, at 3800.124 Å, and we revise its abundance to  $\log \varepsilon(\text{Ir}) = 1.32$ . This value is 0.22 dex lower than that presented in Roederer et al.

The abundance derived from the two Ir I lines with HFS and IS,  $\log \varepsilon(\text{Ir}) = 1.31$ , is comparable to that from the three Ir I lines without HFS and IS,  $\log \varepsilon(\text{Ir}) = 1.24$ . This result suggests that the impact of the HFS and IS in the line lists is small for this set of lines in this star. Both values are much lower than the abundance derived from the



**Table A7.** Hyperfine Structure and Isotope Shift Line Component Pattern for the Ir I  $\lambda 2924$  Line

Wavenumber ( $\text{cm}^{-1}$ )	$\lambda_{\text{air}}$ ( $\text{\AA}$ )	$F_{\text{upper}}$	$F_{\text{lower}}$	Component Position ( $\text{cm}^{-1}$ )	Component Position ( $\text{\AA}$ )	Strength	Isotope
34180.48	2924.7905	7	6	0.096458	−0.008256	0.31250	191
34180.48	2924.7905	6	6	0.023650	−0.002024	0.01231	191
34180.48	2924.7905	6	5	0.045641	−0.003907	0.25852	191

NOTE—Energy levels from the NIST ASD and the index of air (Peck & Reeder 1972) are used to compute the center-of-gravity wavenumbers and air wavelengths,  $\lambda_{\text{air}}$ , and component positions are given relative to those values. Strengths are normalized to sum to 1 for each isotope. The complete version of Table A7 is available in the online edition of the journal in machine-readable format. A short version is included here to demonstrate its form and content.

**Table A8.** Hyperfine Structure and Isotope Shift Line Component Pattern for the Pt I  $\lambda 2274$  Line

Wavenumber ( $\text{cm}^{-1}$ )	$\lambda_{\text{air}}$ ( $\text{\AA}$ )	$F_{\text{upper}}$	$F_{\text{lower}}$	Component Position ( $\text{cm}^{-1}$ )	Component Position ( $\text{\AA}$ )	Strength	Isotope
43954.430	2274.3808	3.0	2.0	0.065542	−0.003392	1.00000	190
43954.430	2274.3808	3.0	2.0	0.041584	−0.002152	1.00000	192
43954.430	2274.3808	3.0	2.0	0.015028	−0.000778	1.00000	194

NOTE—Energy levels from the NIST ASD and the index of air (Peck & Reeder 1972) are used to compute the center-of-gravity wavenumbers and air wavelengths,  $\lambda_{\text{air}}$ , and component positions are given relative to those values. Strengths are normalized to sum to 1 for each isotope. The complete version of Table A8 is available in the online edition of the journal in machine-readable format. A short version is included here to demonstrate its form and content.

two Ir II lines,  $\log \varepsilon(\text{Ir}) = 1.58$ , which is not derived using HFS and IS. Our recommended Ir abundance reflects a weighted average of the five Ir I lines.

#### A.39. *Platinum* (Pt, $Z = 78$ )

We check our spectrum of HD 222925 for 35 Pt I and 8 Pt II lines among the stronger lines listed in Den Hartog et al. (2005) and Quinet et al. (2008). We derive abundances from 8 Pt I lines (Figures 3 and 4) and 1 Pt II line (Figure 2). This marks the first detection of Pt II in a metal-poor star. Den Hartog et al. quote transition probability uncertainties  $\approx 5\text{--}7\%$  (0.02–0.03 dex) for the lines we use. Quinet et al. estimate that their  $\log(gf)$  values are reliable to  $\approx 25\%$  (0.12 dex). The high FIP of Pt, 8.96 eV, ensures that a substantial fraction of both neutral and singly ionized Pt are present in the atmosphere of HD 222925.

There are four stable isotopes of Pt that are accessible to the  $r$ -process:  $^{194}\text{Pt}$ ,  $^{195}\text{Pt}$ ,  $^{196}\text{Pt}$ , and  $^{198}\text{Pt}$ . The  $^{195}\text{Pt}$  isotope has nuclear spin  $I = 1/2$  and thus exhibits HFS. Previous laboratory studies have measured the HFS constants and IS for only a limited selection of the levels required to compute the line component patterns for the lines detected in HD 222925. We include HFS and IS for two of the lines ( $\lambda\lambda 2646.881$  and  $2705.895$ ) from Den Hartog et al. (2005). We compute the pattern for one more line ( $\lambda 2274.381$ ) using the HFS  $A$  constants from Labelle et al. (1989) and Basar et al. (1996) and the IS from Labelle et al. and Kronfeldt & Basar (1995). This line connects an upper  $5d^8 6s(2F)6p$  configuration to a lower  $5d^9 6s$  configuration. The lighter isotope is to the blue of the heavier isotope, which is a negative IS. Table A8 presents the complete line component pattern for this line. Our recommended Pt abundance is based on a weighted average of all nine Pt I and Pt II lines.

**Table A9.** Hyperfine Structure Line Component Pattern for the Au I  $\lambda 2675$  Line

Wavenumber ( $\text{cm}^{-1}$ )	$\lambda_{\text{air}}$ ( $\text{\AA}$ )	$F_{\text{upper}}$	$F_{\text{lower}}$	Component Position ( $\text{cm}^{-1}$ )	Component Position ( $\text{\AA}$ )	Strength
37358.991	2675.9366	2.0	2.0	-0.070073	0.005019	0.31250
37358.991	2675.9366	2.0	1.0	0.137403	-0.009842	0.31250
37358.991	2675.9366	1.0	2.0	-0.090688	0.006496	0.31250
37358.991	2675.9366	1.0	1.0	0.116789	-0.008365	0.06250

NOTE—Energy levels from the NIST ASD and the index of air (Peck & Reeder 1972) are used to compute the center-of-gravity wavenumbers and air wavelengths,  $\lambda_{\text{air}}$ , and component positions are given relative to those values. Strengths are normalized to sum to 1. Table A9 is available in the online edition of the journal in machine-readable format.

#### A.40. Gold (*Au*, $Z = 79$ )

We detect two Au I resonance lines at 2427.950 and 2675.950  $\text{\AA}$ . The  $\lambda 2427$  line is blended, and only the  $\lambda 2675$  line is useful as an abundance indicator. We also check for weaker Au I lines at 2126.630, 2352.580, 2376.240, 2641.480, 2748.250, and 3122.780  $\text{\AA}$  (Fivet et al. 2006; Zhang et al. 2018). None are detected. Our spectrum is relatively unblended around  $\lambda 2376$  and  $\lambda 3122$ , and these lines might be detectable with higher-S/N spectra. The FIP of Au is high, 9.23 eV, and neutral Au is common in the atmosphere of HD 222925. Syntheses of a few of the strongest Au II lines listed in Fivet et al. (2006) reveal that they are too blended to be of use as abundance indicators in HD 222925.

Au has only one stable isotope,  $^{197}\text{Au}$ , which has nuclear spin  $I = 3/2$ . Demidov et al. (2021) calculate HFS  $A$  constants for the upper and lower levels of the  $\lambda 2675$  line, and their values agree with earlier experimental work by Dahmen & Penselin (1967) and Passler et al. (1994). We use the Demidov et al. HFS  $A$  constants to compute the complete line component pattern for this line, which is given in Table A9.

The observed center-of-gravity wavelength listed in the NIST ASD, 2675.950  $\text{\AA}$ , is found to be a better match to the Au I line in our spectrum than the wavelengths calculated directly from the Au I energy levels, 2675.9366  $\text{\AA}$  (Ehrhardt & Davis 1971). This discrepancy is larger than the stated uncertainty in the energy levels measured by Ehrhardt & Davis and the typical uncertainty present in the NIST ASD. Its cause is not immediately clear. Several other Au I lines listed in the NIST ASD exhibit similar discrepancies between their observed and calculated wavelengths. The energies and wavelengths listed in Table A9 are based on the calculated center-of-gravity wavelength, and we shift the wavelengths by +0.022  $\text{\AA}$  in our syntheses.

The NIST ASD quotes a  $\log(gf)$  value for the  $\lambda 2675$  line from Hannaford et al. (1981), with a grade of A+ (2%, 0.01 dex). Measurements by Zhang et al. (2018) of the radiative lifetime of the upper level agree with the Hannaford et al. value to within  $\approx 10\%$ . This agreement is worse than the stated mutual uncertainties of the two measurements, and translates into a 0.05 dex difference in the  $\log(gf)$  values. For consistency with previous Au abundance derivations, we continue to adopt the Hannaford et al.  $\log(gf)$  value, but we caution that the 0.01 dex uncertainty recommended by NIST may be slightly optimistic.

The Au I line at 2675  $\text{\AA}$ , illustrated in Figure 4, is the only one that has previously been used to derive Au abundances in metal-poor stars. Most of the absorption at this wavelength is Au I. The most significant blend is Nb II, at 2675.942  $\text{\AA}$ . We are confident that this blend is synthesized correctly because we know the Nb abundance well (derived from 10 lines; Appendix A.22), NLTE effects are minimal (Appendix A.22), and the  $\log(gf)$  value for this line is known experimentally (38% or 0.20 dex; Nilsson & Ivarsson 2008). We adjust the strength of this blend within its known uncertainty, illustrated by the gray band in Figure 4, which affects the derived Au abundance by about  $\pm 0.07$  dex. We derive  $\log \varepsilon(\text{Au}) = 0.53 \pm 0.22$  from this line. The  $\lambda 2376$  and  $\lambda 3122$  lines yield upper limits  $\log \varepsilon(\text{Au}) < 1.2$  and  $< 1.1$ , which are compatible with this abundance. Our recommended Au abundance is based on this one Au I line.

#### A.41. Lead (*Pb*, $Z = 82$ )

Roederer et al. (2020) reported the detection of the Pb II line at 2203.534  $\text{\AA}$  in HD 222925, as illustrated in Figure 2. That study derived  $\log \varepsilon(\text{Pb}) = 1.14 \pm 0.16$ . The FIP of Pb is 7.42 eV, and singly ionized Pb is the dominant ionization state in the atmosphere of HD 222925. Mashonkina et al. (2012) showed that the ground state of  $\text{Pb}^+$  is formed in LTE, and we assume that the low-excitation level that gives rise to the  $\lambda 2203$  line is also formed in LTE. We adopt

**Table B10.** Radial Velocity Measurements of HD 222925

Date	$V_r$	Unc.	Reference
	(km s <sup>-1</sup> )	(km s <sup>-1</sup> )	
(unspecified)	−34	7	Beers et al. (2014)
(unspecified)	−38.64	0.36	Navarrete et al. (2015)
(unspecified)	−37.93	0.28	Gaia DR2 (Katz et al. 2019)
2017/09/28	−38.9	0.6	Roederer et al. (2018b)
2021/07/04	−38.7	10	new (MagE)
2021/07/05	−25.2	12	new (MagE)
2021/11/24	−37.6	0.6	new (MIKE)
2021/11/25	−38.6	0.6	new (MIKE)
2021/12/05	−38.1	0.6	new (MIKE)
2021/12/06	−38.1	0.6	new (MIKE)

the  $\log(gf)$  from Quinet et al. (2007) (uncertainty  $\approx 14\%$ , or 0.07 dex), the HFS and IS patterns from Roederer et al., and an  $r$ -process isotopic mix from Sneden et al. (2008) in our syntheses.

Peterson (2021) noted the presence of absorption near this wavelength in two stars more metal-poor than HD 222925. Pb absorption would not be expected in those stars, and Peterson postulated that this absorption could be assigned to an unidentified Fe I line with wavelength = 2203.526 Å,  $E_{\text{low}} = 2.18$  eV, and  $\log(gf) = -2.06$ . This postulated line is offset slightly to the blue of the Pb II line, and it would decrease the derived Pb abundance by  $\approx 0.2$  dex. Until additional confirmation of this potential assignment is available, we recommend the Pb abundance for HD 222925 as described in Roederer et al. (2020).

#### A.42. Bismuth (Bi, $Z = 83$ )

We check for the 13 Bi I lines that are listed in the NIST ASD, but we detect none of them. The Bi I line at 2230.609 Å provides the best upper limit on the Bi abundance. It lies in a region between several weak lines of Fe-group species, and the line profile can be reasonably well fit with no Bi present. We derive an upper limit by minimizing the absorption from these blends, while simultaneously providing a reasonable fit to the observed line profile.

#### A.43. Thorium (Th, $Z = 90$ ) and Uranium (U, $Z = 92$ )

There are no Th II or U II lines known in this region of the UV spectrum. Roederer et al. (2018b) derived a Th abundance from 5 optical lines (Nilsson et al. 2002b) and a U upper limit from 2 optical lines (Nilsson et al. 2002a). We perform a new check for the strongest U II lines listed in the study by Gamrath et al. (2018a), and none are detected or useful for further constraining the U abundance. Our recommended Th and U abundances are taken from Roederer et al.

### B. RADIAL VELOCITY MEASUREMENTS OF HD 222925

The radial velocity,  $V_r$ , of HD 222925 has been measured several times over the last decade. All  $V_r$  measurements known to us are listed in Table B10. We have made several new measurements during the most recent observing season, using the Magellan Echellette (MagE) Spectrograph (Marshall et al. 2008) and MIKE. The MagE observations were collected using the 1''0 slit, yielding  $R \sim 4,700$ , and the MIKE observations were collected using the 0''7 slit, yielding  $R \sim 35,000$ . We measure  $V_r$  by cross-correlating the order containing the Mg I “b” triplet against a stellar template, as described in Roederer et al. (2014c). We calculate heliocentric corrections using the IRAF “rvcorrect” task. The dates of some measurements are unspecified by the original references, but the time baseline of the  $V_r$  measurements from high-resolution spectroscopy spans at least 7 yr. No evidence for  $V_r$  variations is found.

### REFERENCES

- |  |   |
|--|---|
| Abbott, B. P., Abbott, R., Abbott, T. D., et al. 2017,<br>ApJL, 850, L39 | Arcones, A., & Martínez-Pinedo, G. 2011, Physical Review<br>C, 83, 045809 |
|--|---|

- Arlandini, C., Käppeler, F., Wisshak, K., et al. 1999, *ApJ*, 525, 886
- Arnould, M., Goriely, S., & Takahashi, K. 2007, *PhR*, 450, 97
- Asplund, M., Grevesse, N., Sauval, A. J., & Scott, P. 2009, *ARA&A*, 47, 481
- Aufmuth, P., Kopp, E. G., & Spiewak, H. 1995, *Journal of Physics B Atomic Molecular Physics*, 28, 3687
- Bäckström, E., Nilsson, H., Engström, L., Hartman, H., & Mannervik, S. 2013, *Journal of Physics B Atomic Molecular Physics*, 46, 205001
- Barbuy, B., Spite, M., Hill, V., et al. 2011, *A&A*, 534, A60
- Barklem, P. S., Christlieb, N., Beers, T. C., et al. 2005, *A&A*, 439, 129
- Basar, G., Kronfeldt, H. D., & Kröger, S. 1996, *Zeitschrift fur Physik D Atoms Molecules Clusters*, 36, 35
- Beers, T. C., Norris, J. E., Placco, V. M., et al. 2014, *ApJ*, 794, 58
- Belmonte, M. T., Pickering, J. C., Ruffoni, M. P., et al. 2017, *ApJ*, 848, 125
- Belokurov, V., Erkal, D., Evans, N. W., Koposov, S. E., & Deason, A. J. 2018, *MNRAS*, 478, 611
- Bergemann, M., & Cescutti, G. 2010, *A&A*, 522, A9
- Bergemann, M., & Gehren, T. 2008, *A&A*, 492, 823
- Bergemann, M., Lind, K., Collet, R., Magic, Z., & Asplund, M. 2012, *MNRAS*, 427, 27
- Bergemann, M., Pickering, J. C., & Gehren, T. 2010, *MNRAS*, 401, 1334
- Bernstein, R., Shtetman, S. A., Gunnels, S. M., Mochnacki, S., & Athey, A. E. 2003, in *Proc. SPIE*, Vol. 4841, *Instrument Design and Performance for Optical/Infrared Ground-based Telescopes*, ed. M. Iye & A. F. M. Moorwood, 1694–1704
- Berzins, U., Ubelis, A., & Bziskjans, A. 2021, *JQSRT*, 276, 107943
- Bessell, M. S., Collet, R., Keller, S. C., et al. 2015, *ApJL*, 806, L16
- Biémont, E., Dutrieux, J. F., Martin, I., & Quinet, P. 1998, *Journal of Physics B Atomic Molecular Physics*, 31, 3321
- Biemont, E., Quinet, P., & Zeippen, C. J. 1993, *A&AS*, 102, 435
- Biémont, É., Blagoev, K., Engström, L., et al. 2011, *MNRAS*, 414, 3350
- Bisterzo, S., Gallino, R., Straniero, O., Cristallo, S., & Käppeler, F. 2011, *MNRAS*, 418, 284
- Bisterzo, S., Travaglio, C., Gallino, R., Wiescher, M., & Käppeler, F. 2014, *ApJ*, 787, 10
- Bisterzo, S., Travaglio, C., Wiescher, M., Käppeler, F., & Gallino, R. 2017, *ApJ*, 835, 97
- Bouazza, S., Guern, Y., Abjean, R., & Bauche, J. 1987, *Zeitschrift fur Physik D Atoms Molecules Clusters*, 7, 33
- Buchholz, B., Kronfeldt, H. D., Müller, G., Voss, M., & Winkler, R. 1978, *Zeitschrift fur Physik A Hadrons and Nuclei*, 288, 247
- Bürger, K. H., Büttgenbach, S., Dicke, R., Gözl, G., & Träber, F. 1984, *Physics Letters B*, 140, 17
- Büttgenbach, S., Dicke, R., Gebauer, H., Kühnen, R., & Träber, F. 1978, *Zeitschrift fur Physik A Hadrons and Nuclei*, 286, 333
- Caffau, E., Bonifacio, P., Faraggiana, R., et al. 2005, *A&A*, 441, 533
- Cameron, A. G. W. 1982, *Ap&SS*, 82, 123
- Charbonnel, C. 1995, *ApJL*, 453, L41
- Chen, M. H., & Cheng, K. T. 2010, *Journal of Physics B Atomic Molecular Physics*, 43, 074019
- Chornock, R., Berger, E., Kasen, D., et al. 2017, *ApJL*, 848, L19
- Côté, B., Denissenkov, P., Herwig, F., et al. 2018, *ApJ*, 854, 105
- Cowan, J. J., Burris, D. L., Sneden, C., McWilliam, A., & Preston, G. W. 1995, *ApJL*, 439, L51
- Cowan, J. J., Pfeiffer, B., Kratz, K.-L., et al. 1999, *ApJ*, 521, 194
- Cowan, J. J., Sneden, C., Lawler, J. E., et al. 2021, *Reviews of Modern Physics*, 93, 015002
- Cowan, J. J., Sneden, C., Roederer, I. U., et al. 2020, *ApJ*, 890, 119
- Cowan, J. J., Sneden, C., Beers, T. C., et al. 2005, *ApJ*, 627, 238
- Cowley, C. R., Ayres, T. R., Castelli, F., et al. 2016, *ApJ*, 826, 158
- Cowley, C. R., Ryabchikova, T., Kupka, F., et al. 2000, *MNRAS*, 317, 299
- Curtis, L. J., Matulioniene, R., Ellis, D. G., & Fischer, C. F. 2000, *PhRvA*, 62, 052513
- Dahmen, H., & Penselin, S. 1967, *Zeitschrift fur Physik*, 200, 456
- Demidov, Y. A., Konovalova, E. A., Imanbaeva, R. T., Kozlov, M. G., & Barzakh, A. E. 2021, *PhRvA*, 103, 032824
- Den Hartog, E. A., Herd, M. T., Lawler, J. E., et al. 2005, *ApJ*, 619, 639
- Den Hartog, E. A., Lawler, J. E., & Roederer, I. U. 2020, *ApJS*, 248, 10
- . 2021a, *ApJS*, 254, 5
- Den Hartog, E. A., Lawler, J. E., Sneden, C., & Cowan, J. J. 2006, *ApJS*, 167, 292
- Den Hartog, E. A., Lawler, J. E., Sneden, C., Cowan, J. J., & Brukhovesky, A. 2019, *ApJS*, 243, 33

- Den Hartog, E. A., Lawler, J. E., Sneden, C., et al. 2021b, *ApJS*, 255, 27
- Den Hartog, E. A., Lawler, J. E., Sobeck, J. S., Sneden, C., & Cowan, J. J. 2011, *ApJS*, 194, 35
- Ding, M., & Pickering, J. C. 2020, *ApJS*, 251, 24
- Dupree, A. K., Li, T. Q., & Smith, G. H. 2007, *AJ*, 134, 1348
- Ehrhardt, J. C., & Davis, S. P. 1971, *Journal of the Optical Society of America* (1917-1983), 61, 1342
- Eichler, M., Arcones, A., Kelic, A., et al. 2015, *ApJ*, 808, 30
- Ezzeddine, R., Rasmussen, K., Frebel, A., et al. 2020, *ApJ*, 898, 150
- Fedchak, J. A., & Lawler, J. E. 1999, *ApJ*, 523, 734
- Fernando, P. C. B., Rochester, G. K., Spalding, I. J., & Smith, K. F. 1960, *Philosophical Magazine*, 5, 1291
- Feuillet, D. K., Sahlholdt, C. L., Feltzing, S., & Casagrande, L. 2021, *MNRAS*, 508, 1489
- Fivet, V., Quinet, P., Biéumont, É., & Xu, H. L. 2006, *Journal of Physics B Atomic Molecular Physics*, 39, 3587
- Frebel, A. 2018, *Annual Review of Nuclear and Particle Science*, 68, 237
- Fröhlich, C., Hauser, P., Liebendörfer, M., et al. 2006, *ApJ*, 637, 415
- Fu, H., Xu, Y., Fang, D., et al. 2021, *JQSRT*, 266, 107590
- Gaia Collaboration, Brown, A. G. A., Vallenari, A., et al. 2021, *A&A*, 649, A1
- Gamrath, S., Palmeri, P., & Quinet, P. 2018a, *MNRAS*, 480, 4754
- Gamrath, S., Palmeri, P., Quinet, P., Bouazza, S., & Godefroid, M. 2018b, *JQSRT*, 218, 38
- Garpman, S., Lidö, G., Rydberg, S., & Svanberg, S. 1971, *Zeitschrift für Physik*, 247, 238
- Gianfrani, L., & Tino, G. M. 1993, *Zeitschrift für Physik D Atoms Molecules Clusters*, 25, 113
- Goriely, S. 1999, *A&A*, 342, 881
- Gough, D. S., Hannaford, P., & Lowe, R. M. 1983, *Journal of Physics B Atomic Molecular Physics*, 16, 785
- Gratton, R. G., Sneden, C., Carretta, E., & Bragaglia, A. 2000, *A&A*, 354, 169
- Gudin, D., Shank, D., Beers, T. C., et al. 2021, *ApJ*, 908, 79
- Gurell, J., Nilsson, H., Engström, L., et al. 2010, *A&A*, 511, A68
- Hannaford, P., Larkins, P. L., & Lowe, R. M. 1981, *Journal of Physics B Atomic Molecular Physics*, 14, 2321
- Hansen, C. J., Primas, F., Hartman, H., et al. 2012, *A&A*, 545, A31
- Hansen, T. T., Holmbeck, E. M., Beers, T. C., et al. 2018, *ApJ*, 858, 92
- Hartman, H., Nilsson, H., Engström, L., et al. 2010, *PhRvA*, 82, 052512
- Hassini, F., Ahmed, Z. B., Robaux, O., Verges, J., & Wyart, J.-F. 1988, *Journal of the Optical Society of America B Optical Physics*, 5, 2060
- Helmi, A., Babusiaux, C., Koppelman, H. H., et al. 2018, *Nature*, 563, 85
- Hill, V., Plez, B., Cayrel, R., et al. 2002, *A&A*, 387, 560
- Holmbeck, E. M., Hansen, T. T., Beers, T. C., et al. 2020, *ApJS*, 249, 30
- Holmgren, L. 1975, *PhysS*, 11, 15
- Hotokezaka, K., Piran, T., & Paul, M. 2015, *Nature Physics*, 11, 1042
- Howard, L. H., & Andrew, K. L. 1985, *Journal of the Optical Society of America B Optical Physics*, 2, 1032
- Howes, L. M., Asplund, M., Keller, S. C., et al. 2016, *MNRAS*, 460, 884
- Hunter, J. D. 2007, *Computing in Science and Engineering*, 9, 90
- Ishigaki, M. N., Aoki, W., & Chiba, M. 2013, *ApJ*, 771, 67
- Ivans, I. I., Simmerer, J., Sneden, C., et al. 2006, *ApJ*, 645, 613
- Ivarsson, S., Wahlgren, G. M., Dai, Z., Lundberg, H., & Leckrone, D. S. 2004, *A&A*, 425, 353
- Jacobson, H. R., Keller, S., Frebel, A., et al. 2015, *ApJ*, 807, 171
- Ji, A. P., Drout, M. R., & Hansen, T. T. 2019, *ApJ*, 882, 40
- Ji, A. P., Frebel, A., Chiti, A., & Simon, J. D. 2016, *Nature*, 531, 610
- Johansson, S. G., Jueizadeh, A., Litzen, U., et al. 1994, *ApJ*, 421, 809
- Jones, E., Oliphant, T., Peterson, P., & et al. 2001, *SciPy: Open source scientific tools for Python*, online. <http://www.scipy.org/>
- Jönsson, P., & Andersson, M. 2007, *Journal of Physics B Atomic Molecular Physics*, 40, 2417
- Käppeler, F., Beer, H., & Wisshak, K. 1989, *Reports on Progress in Physics*, 52, 945
- Karlsson, H., & Litzén, U. 2000, *Journal of Physics B Atomic Molecular Physics*, 33, 2929
- . 2001, *Journal of Physics B Atomic Molecular Physics*, 34, 4475
- Kasen, D., Badnell, N. R., & Barnes, J. 2013, *ApJ*, 774, 25
- Kasen, D., Metzger, B., Barnes, J., Quataert, E., & Ramirez-Ruiz, E. 2017, *Nature*, 551, 80
- Katz, D., Sartoretti, P., Cropper, M., et al. 2019, *A&A*, 622, A205
- Kimble, R. A., Woodgate, B. E., Bowers, C. W., et al. 1998, *ApJL*, 492, L83
- Kirby, E. N., Guhathakurta, P., Zhang, A. J., et al. 2016, *ApJ*, 819, 135
- Kling, R., Ekberg, J. O., & Kock, M. 2000, *JQSRT*, 67, 227



- Kobayashi, C., Karakas, A. I., & Lugaro, M. 2020, *ApJ*, 900, 179
- König, K., Krämer, J., Imgram, P., et al. 2020, *PhRvA*, 102, 042802
- Korotin, S., Andrievsky, S., Caffau, E., & Bonifacio, P. 2017, in *Astronomical Society of the Pacific Conference Series*, Vol. 510, *Stars: From Collapse to Collapse*, ed. Y. Y. Balega, D. O. Kudryavtsev, I. I. Romanyuk, & I. A. Yakunin, 141
- Korotin, S. A., Andrievsky, S. M., & Zhukova, A. V. 2018, *MNRAS*, 480, 965
- Kramida, A., Ralchenko, Y., Reader, J., & NIST ASD Team. 2020, *NIST Atomic Spectra Database* (ver. 5.8), [Online]. Available: <https://physics.nist.gov/asd>, National Institute of Standards and Technology, Gaithersburg, MD.
- Kratz, K.-L., Farouqi, K., & Möller, P. 2014, *ApJ*, 792, 6
- Kratz, K.-L., Farouqi, K., Pfeiffer, B., et al. 2007, *ApJ*, 662, 39
- Kronfeldt, H. D., & Basar, G. 1995, *PhyS*, 51, 227
- Kurucz, R. L. 2011, *Canadian Journal of Physics*, 89, 417
- Labelle, R. D., Fairbank, William M., J., Engleman, Rolf, J., & Keller, R. A. 1989, *Journal of the Optical Society of America B Optical Physics*, 6, 137
- Landstreet, J. D. 2011, *A&A*, 528, A132
- Larkins, P. L., & Hannafor, P. 1993, *Zeitschrift für Physik D Atoms Molecules Clusters*, 27, 313
- Lawler, J. E., den Hartog, E. A., Labby, Z. E., et al. 2007, *ApJS*, 169, 120
- Lawler, J. E., Feigenson, T., Sneden, C., Cowan, J. J., & Nave, G. 2018, *ApJS*, 238, 7
- Lawler, J. E., Guzman, A., Wood, M. P., Sneden, C., & Cowan, J. J. 2013, *ApJS*, 205, 11
- Lawler, J. E., Sneden, C., & Cowan, J. J. 2015, *ApJS*, 220, 13
- Lawler, J. E., Sneden, C., Cowan, J. J., Ivans, I. I., & Den Hartog, E. A. 2009, *ApJS*, 182, 51
- Lawler, J. E., Sneden, C., Cowan, J. J., et al. 2008, *ApJS*, 178, 71
- Lawler, J. E., Sneden, C., Nave, G., et al. 2017, *ApJS*, 228, 10
- Lawler, J. E., Wickliffe, M. E., Cowley, C. R., & Sneden, C. 2001, *ApJS*, 137, 341
- Lemaître, J. F., Goriely, S., Bauswein, A., & Janka, H. T. 2021, *Physical Review C*, 103, 025806
- Li, H. F., Naimi, S., Sprouse, T. M., et al. 2021, *arXiv e-prints*, [arXiv:2112.05312](https://arxiv.org/abs/2112.05312)
- Li, Z. S., Norin, J., Persson, A., et al. 1999, *PhRvA*, 60, 198
- Lind, K., Asplund, M., Barklem, P. S., & Belyaev, A. K. 2011, *A&A*, 528, A103
- Lind, K., Bergemann, M., & Asplund, M. 2012, *MNRAS*, 427, 50
- Lind, K., Primas, F., Charbonnel, C., Grundahl, F., & Asplund, M. 2009, *A&A*, 503, 545
- Lindgren, L., Hernández, J., Bombrun, A., et al. 2018, *A&A*, 616, A2
- Liu, Y., Hutton, R., Zou, Y., Andersson, M., & Brage, T. 2006, *Journal of Physics B Atomic Molecular Physics*, 39, 3147
- Ljung, G., Nilsson, H., Asplund, M., & Johansson, S. 2006, *A&A*, 456, 1181
- Lodders, K., Palme, H., & Gail, H. P. 2009, *Landolt Börnstein*, 4B, 712
- Marshall, J. L., Burles, S., Thompson, I. B., et al. 2008, in *Society of Photo-Optical Instrumentation Engineers (SPIE) Conference Series*, Vol. 7014, *Ground-based and Airborne Instrumentation for Astronomy II*, ed. I. S. McLean & M. M. Casali, 701454
- Martin, D. C., Fanson, J., Schiminovich, D., et al. 2005, *ApJL*, 619, L1
- Mashonkina, L., Ryabtsev, A., & Frebel, A. 2012, *A&A*, 540, A98
- Mashonkina, L., Sitnova, T., & Belyaev, A. K. 2017, *A&A*, 605, A53
- Mashonkina, L. I., Belyaev, A. K., & Shi, J. R. 2016, *Astronomy Letters*, 42, 366
- McElroy, T., & Hibbert, A. 2005, *PhyS*, 71, 479
- Meléndez, J., & Barbuy, B. 2009, *A&A*, 497, 611
- Meyer, B. S., & Brown, J. S. 1997, *Astrophysical Journal Supplement Series*, 112, 199
- Montalbán, J., Mackereth, J. T., Miglio, A., et al. 2021, *Nature Astronomy*, 5, 640
- Morton, D. C. 2000, *ApJS*, 130, 403
- . 2003, *ApJS*, 149, 205
- National Academies. 2021, *Pathways to Discovery in Astronomy and Astrophysics for the 2020s* (Washington, DC: The National Academies Press)
- Navarrete, C., Chanamé, J., Ramírez, I., et al. 2015, *ApJ*, 808, 103
- Nilsson, H., Engström, L., Lundberg, H., et al. 2008, *European Physical Journal D*, 49, 13
- Nilsson, H., & Ivarsson, S. 2008, *A&A*, 492, 609
- Nilsson, H., Ivarsson, S., Johansson, S., & Lundberg, H. 2002a, *A&A*, 381, 1090
- Nilsson, H., Zhang, Z. G., Lundberg, H., Johansson, S., & Nordström, B. 2002b, *A&A*, 382, 368
- Nilsson, H., Hartman, H., Engström, L., et al. 2010, *A&A*, 511, A16

- Niu, P., Liu, W., Cui, W., & Zhang, B. 2014, *MNRAS*, 443, 2426
- Nordlander, T., & Lind, K. 2017, *A&A*, 607, A75
- Norris, J., Bessell, M. S., & Pickles, A. J. 1985, *ApJS*, 58, 463
- Oliver, P., & Hibbert, A. 2010, *Journal of Physics B Atomic Molecular Physics*, 43, 074013
- Ortiz, M., Aragón, C., Aguilera, J. A., Rodríguez-García, J., & Mayo-García, R. 2013, *Journal of Physics B Atomic Molecular Physics*, 46, 185702
- Ou, X., Roederer, I. U., Sneden, C., et al. 2020, *ApJ*, 900, 106
- Pakhomov, Y. V., Ryabchikova, T. A., & Piskunov, N. E. 2019, *Astronomy Reports*, 63, 1010
- Palmeri, P., Quinet, P., Biémont, É., Xu, H. L., & Svanberg, S. 2005, *MNRAS*, 362, 1348
- Passler, G., Rikowska, J., Arnold, E., et al. 1994, *NuPhA*, 580, 173
- Peck, E. R., & Reeder, K. 1972, *Journal of the Optical Society of America (1917-1983)*, 62, 958
- Peterson, R. C. 2011, *ApJ*, 742, 21
- . 2021, *ApJL*, 914, L22
- Peterson, R. C., Barbuy, B., & Spite, M. 2020, *A&A*, 638, A64
- Peterson, R. C., & Kurucz, R. L. 2015, *ApJS*, 216, 1
- Peterson, R. C., Kurucz, R. L., & Ayres, T. R. 2017, *ApJS*, 229, 23
- Pignatari, M., Gallino, R., Heil, M., et al. 2010, *ApJ*, 710, 1557
- Piskunov, N. E., Kupka, F., Ryabchikova, T. A., Weiss, W. W., & Jeffery, C. S. 1995, *A&AS*, 112, 525
- Placco, V. M., Frebel, A., Beers, T. C., & Stancliffe, R. J. 2014, *ApJ*, 797, 21
- Placco, V. M., Sneden, C., Roederer, I. U., et al. 2021, *Research Notes of the American Astronomical Society*, 5, 92
- Placco, V. M., Beers, T. C., Ivans, I. I., et al. 2015, *ApJ*, 812, 109
- Plez, B., Hill, V., Cayrel, R., et al. 2004, *A&A*, 428, L9
- Quinet, P., Biémont, E., Palmeri, P., et al. 2012, *A&A*, 537, A74
- Quinet, P., Biémont, E., Palmeri, P., & Xu, H. L. 2007, *Journal of Physics B Atomic Molecular Physics*, 40, 1705
- Quinet, P., Fivet, V., Palmeri, P., et al. 2009, *A&A*, 493, 711
- Quinet, P., Palmeri, P., Biémont, É., et al. 2006, *A&A*, 448, 1207
- Quinet, P., Palmeri, P., Biémont, E., et al. 1999, *MNRAS*, 307, 934
- Quinet, P., Palmeri, P., Fivet, V., et al. 2008, *PhRvA*, 77, 022501
- Rasmussen, K. C., Zepeda, J., Beers, T. C., et al. 2020, *ApJ*, 905, 20
- Roederer, I. U. 2012, *ApJ*, 756, 36
- Roederer, I. U., & Barklem, P. S. 2018, *ApJ*, 857, 2
- Roederer, I. U., Cowan, J. J., Preston, G. W., et al. 2014a, *MNRAS*, 445, 2970
- Roederer, I. U., Hattori, K., & Valluri, M. 2018a, *AJ*, 156, 179
- Roederer, I. U., Jacobson, H. R., Thanathibodee, T., Frebel, A., & Toller, E. 2014b, *ApJ*, 797, 69
- Roederer, I. U., Karakas, A. I., Pignatari, M., & Herwig, F. 2016a, *ApJ*, 821, 37
- Roederer, I. U., Kratz, K.-L., Frebel, A., et al. 2009, *ApJ*, 698, 1963
- Roederer, I. U., & Lawler, J. E. 2012, *ApJ*, 750, 76
- . 2021, *ApJ*, 912, 119
- Roederer, I. U., Placco, V. M., & Beers, T. C. 2016b, *ApJL*, 824, L19
- Roederer, I. U., Preston, G. W., Thompson, I. B., et al. 2014c, *AJ*, 147, 136
- Roederer, I. U., Sakari, C. M., Placco, V. M., et al. 2018b, *ApJ*, 865, 129
- Roederer, I. U., Sneden, C., Lawler, J. E., & Cowan, J. J. 2010, *ApJL*, 714, L123
- Roederer, I. U., Sneden, C., Lawler, J. E., et al. 2018c, *ApJ*, 860, 125
- Roederer, I. U., Lawler, J. E., Sobeck, J. S., et al. 2012a, *ApJS*, 203, 27
- Roederer, I. U., Lawler, J. E., Cowan, J. J., et al. 2012b, *ApJL*, 747, L8
- Roederer, I. U., Schatz, H., Lawler, J. E., et al. 2014d, *ApJ*, 791, 32
- Roederer, I. U., Lawler, J. E., Holmbeck, E. M., et al. 2020, *ApJL*, 902, L24
- Saha, M. N. 1921, *Proceedings of the Royal Society of London Series A*, 99, 135
- Sakari, C. M., Placco, V. M., Farrell, E. M., et al. 2018, *ApJ*, 868, 110
- Scott, P., Grevesse, N., Asplund, M., et al. 2015, *A&A*, 573, A25
- Shukla, N., Kaur, H., Arora, B., & Srivastava, R. 2022, *Physica B Condensed Matter*, 624, 413422
- Siegel, D. M., Barnes, J., & Metzger, B. D. 2019, *Nature*, 569, 241
- Sikström, C. M., Pihlemark, H., Nilsson, H., et al. 2001, *Journal of Physics B Atomic Molecular Physics*, 34, 477
- Siqueira Mello, C., Spite, M., Barbuy, B., et al. 2013, *A&A*, 550, A122

- Sitnova, T. M., Yakovleva, S. A., Belyaev, A. K., & Mashonkina, L. I. 2020, *Astronomy Letters*, 46, 120
- Smartt, S. J., Chen, T. W., Jerkstrand, A., et al. 2017, *Nature*, 551, 75
- Snedden, C., Cowan, J. J., Burris, D. L., & Truran, J. W. 1998, *ApJ*, 496, 235
- Snedden, C., Cowan, J. J., & Gallino, R. 2008, *ARA&A*, 46, 241
- Snedden, C., Cowan, J. J., Kobayashi, C., et al. 2016, *ApJ*, 817, 53
- Snedden, C., McWilliam, A., Preston, G. W., et al. 1996, *ApJ*, 467, 819
- Snedden, C., Preston, G. W., McWilliam, A., & Searle, L. 1994, *ApJL*, 431, L27
- Snedden, C., Cowan, J. J., Lawler, J. E., et al. 2003, *ApJ*, 591, 936
- Snedden, C. A. 1973, PhD thesis, The University of Texas at Austin.
- Sobeck, J. S., Lawler, J. E., & Sneden, C. 2007, *ApJ*, 667, 1267
- Sobeck, J. S., Kraft, R. P., Sneden, C., et al. 2011, *AJ*, 141, 175
- Sobolewski, L. M., Bouazza, S., & Kwela, J. 2016a, *European Physical Journal D*, 70, 20
- Sobolewski, L. M., Bouazza, S., Windholz, L., & Kwela, J. 2016b, *Journal of the Optical Society of America B Optical Physics*, 33, 1921
- Sprouse, T. M., Mumpower, M. R., & Surman, R. 2021, *Physical Review C*, 104, 015803
- Surman, R., Beun, J., McLaughlin, G. C., & Hix, W. R. 2009, *Physical Review C*, 79, 045809
- Surman, R., & Engel, J. 2001, *Physical Review C*, 64, 035801
- Takeda, Y., Zhao, G., Chen, Y.-Q., Qiu, H.-M., & Takada-Hidai, M. 2002, *PASJ*, 54, 275
- Theodosiou, C. E. 1989, *PhRvA*, 39, 4880
- Tody, D. 1993, in *Astronomical Society of the Pacific Conference Series*, Vol. 52, *Astronomical Data Analysis Software and Systems II*, ed. R. J. Hanisch, R. J. V. Brissenden, & J. Barnes, 173
- Träbert, E., Wolf, A., Linkemann, J., & Tordoir, X. 1999, *Journal of Physics B Atomic Molecular Physics*, 32, 537
- Travaglio, C., Gallino, R., Arnone, E., et al. 2004, *ApJ*, 601, 864
- Ubelis, A. P., & Berzinsh, U. V. 1983, *PhyS*, 28, 171
- . 1991, *PhyS*, 43, 162
- van der Walt, S., Colbert, S. C., & Varoquaux, G. 2011, *Computing in Science Engineering*, 13, 22
- Vassh, N., Vogt, R., Surman, R., et al. 2019, *Journal of Physics G Nuclear Physics*, 46, 065202
- Wahlgren, G. M., Johansson, S. G., Litzén, U., et al. 1997, *ApJ*, 475, 380
- Wanajo, S., Janka, H.-T., & Müller, B. 2011, *ApJL*, 726, L15
- Wanajo, S., Kajino, T., Mathews, G. J., & Otsuki, K. 2001, *ApJ*, 554, 578
- Wang, Y. H., Dumke, R., Zhang, J., et al. 2007, *European Physical Journal D*, 44, 307
- Watson, D., Hansen, C. J., Selsing, J., et al. 2019, *Nature*, 574, 497
- Westin, J., Sneden, C., Gustafsson, B., & Cowan, J. J. 2000, *ApJ*, 530, 783
- Wickliffe, M. E., & Lawler, J. E. 1997, *Journal of the Optical Society of America B Optical Physics*, 14, 737
- Wickliffe, M. E., Lawler, J. E., & Nave, G. 2000, *JQSRT*, 66, 363
- Wiese, W. L., Smith, M. W., & Miles, B. M. 1969, *Atomic Transition Probabilities, Vol. II: Sodium through Calcium - A Critical Data Compilation* (U.S. Government Printing Office, Washington, D.C.)
- Wood, M. P., & Lawler, J. E. 2012, *ApOpt*, 51, 8407
- Wood, M. P., Lawler, J. E., Den Hartog, E. A., Sneden, C., & Cowan, J. J. 2014a, *ApJS*, 214, 18
- Wood, M. P., Lawler, J. E., Sneden, C., & Cowan, J. J. 2013, *ApJS*, 208, 27
- . 2014b, *ApJS*, 211, 20
- Woodgate, B. E., Kimble, R. A., Bowers, C. W., et al. 1998, *PASP*, 110, 1183
- Woosley, S. E., & Hoffman, R. D. 1992, *ApJ*, 395, 202
- Wu, M.-R., Fernández, R., Martínez-Pinedo, G., & Metzger, B. D. 2016, *MNRAS*, 463, 2323
- Xu, H. L., Svanberg, S., Quinet, P., Palmeri, P., & Biémont, É. 2007, *JQSRT*, 104, 52
- Xu, H. L., Persson, A., Svanberg, S., et al. 2004, *PhRvA*, 70, 042508
- Yamaguchi, A., Safronova, M. S., Gibble, K., & Katori, H. 2019, *PhRvL*, 123, 113201
- Yong, D., Kobayashi, C., Da Costa, G. S., et al. 2021a, *Nature*, 595, 223
- Yong, D., Da Costa, G. S., Bessell, M. S., et al. 2021b, *MNRAS*, 507, 4102
- Zhang, M., Zhou, L., Gao, Y., et al. 2018, *Journal of Physics B Atomic Molecular Physics*, 51, 205001